PhD-FSTC-2016-11
The Faculty of Sciences, Technology and Communication

DISSERTATION

Presented on 24/03/2016 in Luxembourg

to obtain the degree of

DOCTEUR DE L'UNIVERSITÉ DU LUXEMBOURG

EN CHIMIE

by

Alexandre Crossay

Born on 20 April 1986 in Fontenay-aux-Roses (France)

ELECTRODEPOSITION AND SELENIZATION OF METALLIC THIN FILMS FOR KESTERITE SOLAR CELLS APPLICATION

Dissertation defense committee

Dr Phillip Dale, Dissertation supervisor
Université du Luxembourg

Prof. Dr. Alejandro Pérez Rodriguez, Vice Chairman
Professor, Institut de Recerca en Energia de Catalunya

Dr. Diego Colombara
Université du Luxembourg

Dr. Pierre-Philippe Grand
EDF lab Chatou, IRDEP

Prof. Dr. Jan Lagerwall, Chairman
Professor, Université du Luxembourg

Table of Contents

Abstract

Thin films of Kesterite $Cu_2ZnSnSe_4$ (CZTSe) are prepared via a low energy cost and high material efficiency process, to be potentially used as light absorbers in solar cell devices. The fabrication process involves two main steps: (i) formation of a metallic stack of Cu/Sn/Zn by sequential electrodeposition of Cu, Sn and Zn onto glass/Mo substrates; (ii) reactive annealing at 550°C in presence of Se and SnSe powders to form Kesterite. This thesis mainly aims at understanding the mechanisms of metal alloying and selenization occurring during step (ii), and their effects on the microstructure of the final film, the presence of secondary phases and their distribution in the thin films synthesized. The second objective is to understand their effects on the solar cells parameters.

The stoichiometry of the precursor layers Cu/Sn/Zn is deliberately chosen to be Cu-poor and Zn-rich ($Cu/(Zn+Sn)<1$ and $Zn/Sn>1$), as it allows to reach the best power conversion efficiencies. Under these conditions, Kesterite, $SnSe_2$ and ZnSe are expected. However, a study of different compositions shows that the predominant phases present are only Kesterite and ZnSe. $SnSe_2$ is not present because this phase is unstable under the conditions of selenization, which leads to a self-regulation of tin content via gas phase exchange of SnSe during the selenization.

Analyses of the selenization of Cu/Sn/Zn layers at short times and lower temperatures allow to deconstruct the mechanism of Kesterite formation into sequential steps. Because of the diffusion of metals and the formation of alloys, a reorganization of metals is observed prior to the incorporation of selenium in the thin films. The layers are then composed of Sn, Cu-Sn and Cu-Zn phases mainly, which are found to be segregating at large scales of tens of micrometers. During selenium incorporation, a tin self-regulation process is established, in which tin is depleted during the first stages of selenization, and then tin is replenished. ZnSe segregates at the surface of the absorber layer as large islands of 10-20 micrometers. By analyzing a specific position of a sample after the different process steps, it is shown that the segregation of ZnSe at this large scale is originating in the segregation of metals during alloying.

Because of the presence of ZnSe on the surface of the films, part of the photocurrent generated in the absorber layer is not collected, which decrases the short circuit current of the devices. In this sense, a linear decrease of short circuit current is observed when the ZnSe molar ratio is increasing, and confirmed by external quantum efficiency (EQE) measurements showing a decrease of current collected through the whole range of photon energies. An optimal molar ratio of $ZnSe/(CZTSe + ZnSe)=0.2$ is found. Below this value, the short circuit current decreases, probably due to the formation of other types of harmful secondary phases such as Cu_2SnSe_3 or Cu_2Se.

A strong decrease of open circuit voltage and fill factor of the solar cells is proved to be related to the formation of blisters in the thin films, which result in the creation of pinholes due to their fragility. Formation of these blisters is supposed to originate from hydrogen evolution under the Cu layer during the electrodeposition process.

Finally, a study of an additional process of prealloying between the steps of electrodeposition and selenization is presented, which demonstrates the possibility to increase the open circuit voltage of the solar cells by varying the time of this alloying step. A best power conversion efficiency of 7.2% is achieved via this method, which is close to the highest value of 9.1% reported for an electrodeposition-based process of Kesterite synthesis.

Acknowledgements

I first would like to thank my supervisors, Phillip Dale and Diego Colombara (Laboratory for Energy Materials, Luxembourg), for giving me the opportunity to do my Ph.D. at the University of Luxembourg. I really appreciated your advice and your help through the whole project.
I am also very grateful to Alejandro Pérez-Rodriguez, head of the Institut de Recerca en Energia de Catalunya (IREC, Spain) for agreeing to be part of my CET committee, following the development of my research, and for all the work done leading the Scalenano project.
Further, I would like to thank Jan Lagerwall, head of the Experimental Soft Matter Physics group at the University of Luxembourg, and Pierre-Philippe Grand (EDF, France; formerly at NEXCIS, France), for being co-examiners of my thesis.

I want as well to thank all the members of the LPV and LEM, from the start to the end of my project, for the great help and support, and for the very nice working atmosphere. I really enjoyed working in this team! I am very grateful to a number of people: Maxime Thevenin and Michele Melchiorre, for providing the molybdenum substrates, doing the cells finishing and all SEM analyses; Thomas Schuler for all the help with everything; Erika Robert, for all the IV and EQE measurements of solar cells, this was a great help; Monika Arasimowicz who shared her knowledge on Kesterite and electrodeposition; Helen Meadows for the help with the copper electrodeposition, and the RTP oven; Alex Redinger and Marina Mousel, who helped me getting started with the oven; David Regesch, and Jessica DeWild for performing valuable PL analyses; Patricia Ramoa, for taking care of all organizational things, and for being a very good office neighbor; the students who participated to the work: Florian Maretti, and Jakob; Vicente Reis Adonis for the fabrication of electrodeposition tanks.

I am also very grateful to NEXCIS for sharing their knowledge on the electrodeposition at the start of the project, and especially Laura Vauche, Pierre-Philippe Grand, Salvador Jaime, Cedric Broussillou and Aurélie Jourdan who were very good partners for the Scalenano project.

Furthermore, I want to thank Mael Guennou, Nathalie Valle, Brahime Eladib and all other members of the Luxembourg Institute of Science and Technology who were invested into the characterizations of my samples.

Many thanks to Edgardo Saucedo and Sergio Giraldo for being involved into testing the IREC process on my precursor samples.

I would also like to thank Laurent Lombez, and Enrique Leite from IRDEP, for the measurement of mini solar cells.

Budhika Mendis, from the University of Durham, is also acknowledged for the FIB cross section analyses that he performed.

Further, I would like to thank Steffen Kretzschmar, from Helmholtz Zentrum Berlin, for the collaboration and the measurement of PL.

Financial support from the Scalenano project (Co-financed by the Seventh Framework programme of the European community under grant agreement nº284486) is as well acknowledged.

And finally I would like to thank my family and my friends, who were a great support during these years.

Work done in conjunction with others

The work presented in this thesis was carried out by the author, with the following exceptions:

1. The Mo-coated substrates were provided either by Maxime Thévenin, Dr. Michele Melchiorre from the Laboratory for Photovoltaics of the University of Luxembourg, or NEXCIS.
2. The scanning electron microscopy measurements were performed either by Maxime Thevenin or Dr. Michele Melchiorre from the University of Luxembourg.
3. The Raman analyses were done by Mael Guennou and Brahime Eladib from the LIST in Belvaux, Luxembourg.
4. The measurement of the solar cells and EQE spectra of section 5.2 was done by Erika Robert (University of Luxembourg).
5. The secondary ion mass spectrometry measurements were performed by Dr Nathalie Valle and Brahime Eladib from the CRP Gabriel Lippmann in Belvaux, Luxembourg.
6. The measurements using a focused ion beam microscope were performed by Dr Budhika Mendis from Durham University, United Kingdom.
7. The cells finishing (CdS, window layer, front contact) was done either by Maxime Thevenin or Dr. Michele Melchiorre (University of Luxembourg).
8. The fitting of IV curves was done by using a software provided by Thomas Weiss (University of Luxembourg).
9. The GDOES analyses were done at NEXCIS by Salvador Jaime.
10. The solar cells of section 5.3.2 were measured at IRDEP (Institut de Recherche et Developpement sur l'énergie photovoltaique), with the help of Laurent Lombez and Enrique Leite.

The evaluation of all the results was carried out by the author.

List of abbreviations

CBD	Chemical bath deposition
CE	Counter electrode
CIGSe	$Cu(In,Ga)Se_2$
CTSe	Cu_2SnSe_3
CZTSe	$Cu_2ZnSnSe_4$
CZTSSe	$Cu_2ZnSn(S,Se_4)$
ED	Electrodeposition
EDX	Energy-dispersive X-ray spectroscopy
EQE	External quantum efficiency
FF	Fill factor
FIB	Focused ion beam
FWHM	Full width at half maximum
GDOES	Glow discharge optical emission spectrometry
JV	Current-voltage
NHE	Normal hydrogen electrode
PV	Photovoltaics
PVD	Physical vapor deposition
R_a	Roughness average
RDE	Rotating disk electrode
RE	Reference electrode
RTP	Rapid thermal processor
SE	Secondary electrons
SEM	Scanning electron microscopy
SIMS	Secondary ion mass spectrometry
SLG	Soda lime glass
WE	Working electrode
XRD	X-ray diffraction
XRF	X-ray fluorescence

1 Introduction

1.1 Photovoltaics as a sustainable source of energy

As the world population is increasing and should have reached 10 billion by 2060 [1], energy production will be one of the main challenges of the next decades. In 2014, 85% of the world energy consumption was provided by carbon-emitting and non-renewable sources (oil 31%, natural gas 23%, coal 31%) [2], which poses serious problems of climate change and sustainability. An expansion of renewable sources of energy is thus necessary, including photovoltaics (PV).

The majority of installed PV is currently based on crystalline silicon. High power conversion efficiencies can be obtained with these solar cells, of more than 22% at large scale (>15000 cm²) [3]. However, despite the abundance of silicon, these solar cells are characterized by an energy intensive and high cost fabrication process. The indirect bandgap of the material implies that thick layers of high purity material of about 200 micrometers need to be used. This technology suffers as well from resource limitations, due to the use of silver as front contact [4]. For this reason, alternative solar cell technologies are being developed, based on direct bandgap materials, which require only thin films of absorber materials, of a few micrometers. Among them, CdTe and $Cu(In,Ga)(S,Se)_2$ (CIGS) are the most common. More recently, a strong research activity was concentrated on the development of a new material for thin film solar cells, Kesterite $Cu_2ZnSn(S,Se)_4$ (CZTS), which only requires earth-abundant elements. This material is the subject of the work presented in this thesis.

1.2 Thin film solar cells

1.2.1 Structure of a thin film solar cell

Thin film solar cells are based on absorber materials which have a direct bandgap. Thus the light can be absorbed in a much smaller volume compared to indirect bandgap materials such as silicon, because of the higher absorption coefficient, typically in the order $10^4 – 10^5$ cm^{-1}. The structure of a thin film solar cell is presented in figure 1.1. The cell is composed of a stack of several layers. The central part is composed of the p-n junction: a p-type semiconductor, called the absorber, coupled with several n-type semiconductor window layers. Basically, the p-type absorber layer absorbs the incoming light. Electron-hole pairs generated in this semiconductor are separated due to the presence of the p-n junction. The electrons flow to the n-type layers, while holes are directed to the opposite direction, which creates an electrical current. The back contact is made of molybdenum which is a good electrical conductor. The front contact layers are composed of a thin layer of CdS (called the buffer layer) followed by i-ZnO (intrinsic zinc oxide, not shown on the schematic) and a layer of Aluminum-doped zinc oxide on top, which has the property of being conductive and transparent as well. More information is available about this in chapter 5.

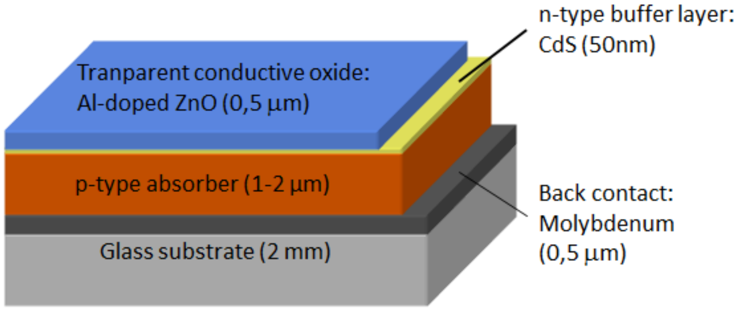

Figure 1.1: Schematic representation of a thin film solar cell.

The electrical characterization of a solar cell is performed by measuring the electrical current density generated by the solar cell while varying the voltage. An example of a current density – voltage (J-V) curve is shown in figure 1.2. Three different parameters are used to describe this type of curve: the sort circuit current (J_{sc}) which is the current density delivered by the solar cell when there is no difference of potential between the contacts; the open circuit voltage (V_{oc}) which is the voltage of the solar cell when no current is flowing; and finally the Fill factor (FF), which describes the squareness of the J-V curve. The fill factor is the ratio of the area of the rectangle A (in figure 1.2) versus the area of the rectangle B. The rectangle A is taken at the J and V values for which the power JxV is maximum, and the rectangle B at J_{sc} and V_{oc}.

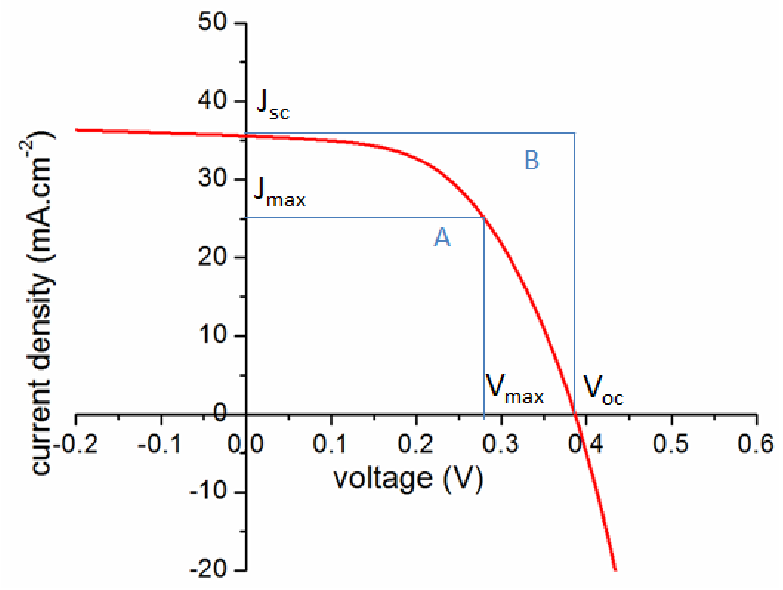

Figure 1.2: Current density-voltage (J-V) characteristic of a 7% power conversion efficiency solar cell with V_{oc}=386 mV, J_{sc}=35.5 mA/cm², FF=53%.

The power conversion efficiency of a solar cell is calculated as the ratio of the power output versus the power input (power of light), as in equation 1.1.

$$\eta = \frac{J_{\max} . V_{\max}}{P_{input}} \quad (1.1)$$

It can be calculated using the values of fill factor, V_{oc} and J_{sc}. The fill factor being defined by equation 1.2, the power conversion efficiency can be written as relation 1.3.

$$FF = \frac{J_{\max} . V_{\max}}{J_{sc} . V_{oc}} \quad (1.2)$$

$$\eta = \frac{FF . J_{sc} . V_{oc}}{P_{input}} \quad (1.3)$$

Thus, V_{oc}, J_{sc} and FF need to be as high as possible in order to increase the efficiency of the solar cells. Further information on solar cells characterization will be provided in chapter 2.

1.2.2 Chalcogenide thin film solar cells

The $Cu_2ZnSnS(e)_4$ absorber material which is the subject of this thesis belongs to the family of chalcogenides, including several semiconductors used as absorbers for thin film solar cells: CdTe, CIGS. All these materials can be derived via a systematic approach of isoelectronic substitution [5], which consists to start from one element (silicon) and then substitute one element by two others, the average number of valence electrons remaining the same (figure 1.3).

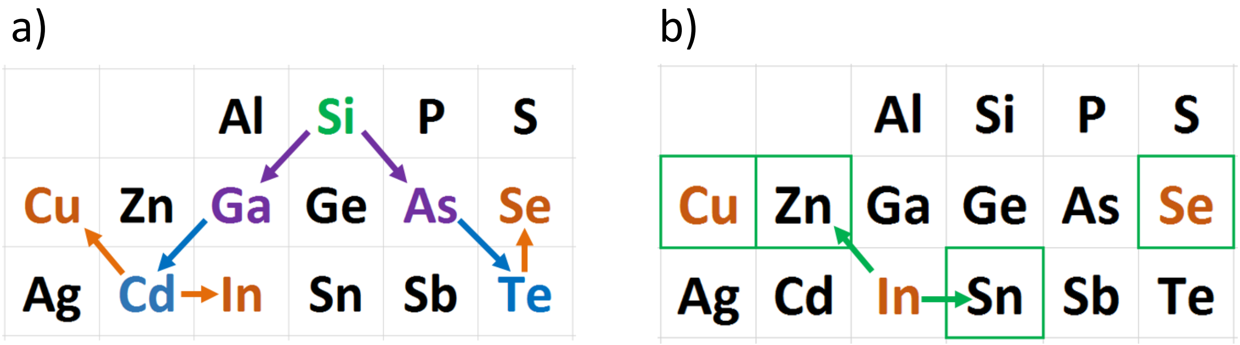

Figure 1.3: Periodic table showing genealogical derivation of semiconductors by isoelectronic substitution: (a) derivation Si – GaAs – CdTe – $CuInSe_2$; (b) $CuInSe_2$ – $Cu_2ZnSnSe_4$.

Extensive research has already been performed in the field of CIGS solar cells, for approximately 40 years (for a detailed history of evolution of cells efficiencies for each material, see NREL efficiency chart [6]). The best device efficiency for this material reaches now 21.7% [7], which is close to the crystalline silicon highest efficiency of 25% [3]. Since the middle of the 1990s, Kesterite is emerging as an alternative to CIGS. The main advantage is to replace indium by more abundant and cheaper elements. Zinc and tin are produced in respectively 20 000 and 500 times larger quantities than indium [8]. Furthermore indium price is increasing due to the high demand from the electronic display industry. Another advantage is that

Kesterite is similar to CIGS, thus a transition to a Kesterite-based solar cell may take advantage of the more mature knowledge gained on CIGS solar cells. Thus, in this thesis often results on Kesterite will be compared to those known for CIGS.

1.3 Kesterite thin film solar cells

1.3.1 Generalities on Kesterite

Kesterite is defined as the Zn-rich variety of the mineral $Cu_2(Zn,Fe)SnS_4$. By extension, the selenide variety $Cu_2ZnSnSe_4$ is also called Kesterite. This semiconductor has a p-type conductivity, a direct bandgap and its optoelectronic properties are suitable for application as an absorber layer in a solar cell (for more details, see section 1.3.2). Its similarity with CIGS offers the advantage to use the same solar cell structure: CdS as buffer layer, molybdenum as back contact and ZnO as front contact. Although, this structure is found to be not optimal for Kesterite, and alternative materials for buffer layer as well as for back contact will probably be necessary to reach efficiencies comparable to CIGS.

An advantage is also to have the possibility to tune the bandgap of the absorber by using a mixture of sulfide and selenide CZTSSe. S and Se are highly miscible in Kesterite, and CZTS has a bandgap of 1.45 eV [9], while the bandgap of CZTSe is 1.0 eV [10]. Thus it is possible to optimize the bandgap, which then theoretically allows efficiencies higher than 30% [11].

Historically, the first reports on the synthesis of Kesterite date from the 1960s [12], [13]. Twenty years later, Ito et al. [9] identified CZTS as a suitable absorber for solar cells, by preparing a heterojunction cadmium tin oxide – CZTS which showed an open circuit voltage of 165 mV under illumination. The first reported power conversion efficiency dates from 1997, when Katagiri et al. [14] presented a value of 0.66%. The highest reported power conversion efficiency achieved with a Kesterite absorber is currently 12.6% [15]. Since the past twenty years, many reports on Kesterite solar cells were published. Several reviews of the literature available [16]–[32], as well as books on the subject ([5], [33] among others).

Two main routes can be employed to synthesize Kesterite absorbers: (i) direct synthesis of the Kesterite, which is often followed by an annealing step to improve the quality of the material, or (ii) two-step synthesis, involving first the deposition of a metallic layer of Cu-Sn-Zn, followed by a reactive annealing at 500-600°C to incorporate the chalcogen. Route (ii) can then be itself divided into two different types of process: physical and chemical deposition. Physical deposition includes evaporation or sputtering of the metals, and typically requires high vacuum. With chemical depositions, the metals are dissolved or dispersed in solutions, and can be directly deposited on the substrates by ink-coating, spraying, or electrodeposition. The advantages of chemical deposition techniques are their lower-cost and high material utilization.

1.3.2 Optoelectronic properties

As previously mentioned, CZTSe is a p-type semiconductor, mainly because of the high population of acceptor defects Cu_{Zn} and V_{Cu} [34]. It has a direct bandgap with a value of around 1.0 eV [10], which can vary from 0.95 eV to 1.05 eV depending on the ordering of the material [35] (caused by the presence of Zn_{Cu} and Cu_{Zn} defect complexes, this will be explained further in section 1.3.3). Its absorption coefficient is $>10^4$ cm^{-1} [9]. The net carrier concentration is not precisely determined, and many different values can be found ranging from 1.2×10^{15} to 3.1×10^{20} cm^{-3} [34].

1.3.3 Crystal structure and defects

The Kesterite crystal structure derives from that of chalcopyrite, which itself derives from the zinc blende structure. The Kesterite unit cell is shown in figure 1.4.

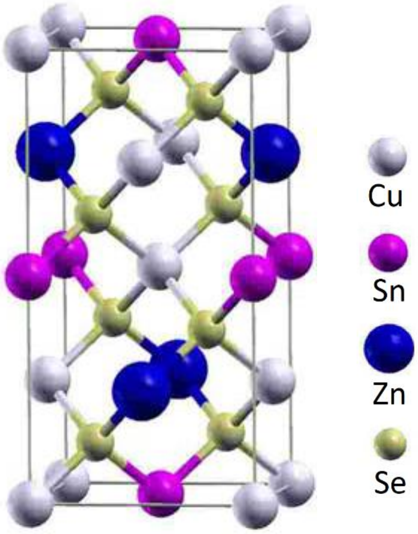

Figure 1.4: Crystal structure of Kesterite (figure adapted from [10]**).**

Among the possible defects, V_{Cu} and Cu_{Zn} have a low formation energy, and both have a donor behavior, thus they are possible candidates for generating a p-type conductivity in the semiconductor. However, all high efficiency solar cells are produced by using a Cu-poor and Zn-rich composition, the optimal value being in the order of Cu/(Zn+Sn)=0.85 and Zn/Sn=1.1-1.3 [23]. In these conditions, Cu_{Zn} has a higher formation energy and thus V_{Cu} is the most likely defect generating the p-type conductivity of the Kesterite.

Charge-compensated defect clusters are also calculated to be present in relatively high concentrations, mainly [Cu_{Zn} + Zn_{Cu}]. These defect clusters create potential fluctuations within the material, which affects significantly the bandgap of the material. A way to increase the ordering of the Kesterite (by decreasing the concentration of these defect complexes), is to perform a low temperature annealing treatment. Rey et al. [35] showed a transition between ordered (low concentration of defect clusters) and disordered Kesterite at a temperature of 200 +/- 20°C. Below this temperature, the concentration of [Cu_{Zn} + Zn_{Cu}] decreases, and above the concentration increases. Disordered CZTSe has a bandgap of 0.95 +/- 0.01 eV, while ordered Kesterite has a bandgap of 1.05 +/- 0.01 eV. However, improvement of solar cells efficiencies by ordering Kesterite has not yet been reported.

1.3.4 Phase stability

The Kesterite selenide system was studied by Dudchak [36], who proposed to describe it by considering the pseudo-ternary system Cu_2Se-$SnSe_2$-ZnSe, as shown in figure 1.5. The stability domain of the Kesterite phase is relatively narrow compared to CIGS for example. Thus, secondary phases (metal selenide phases other than Kesterite) are easily formed during the synthesis process. All secondary phases are reported to be detrimental for the solar cell performances. However, among all possible secondary phases, ZnSe seems to be the least harmful [37].

The best Kesterite solar cell devices are made with absorber layers grown with a copper poor and zinc rich composition (Cu/(Zn+Sn)<1 and Zn/Sn>1) [23], [24], which leads inevitably to the presence of ZnSe, Cu_2Se or $SnSe_2$ secondary phases [36], as described in figure 4.1 (adapted from Dudchak).

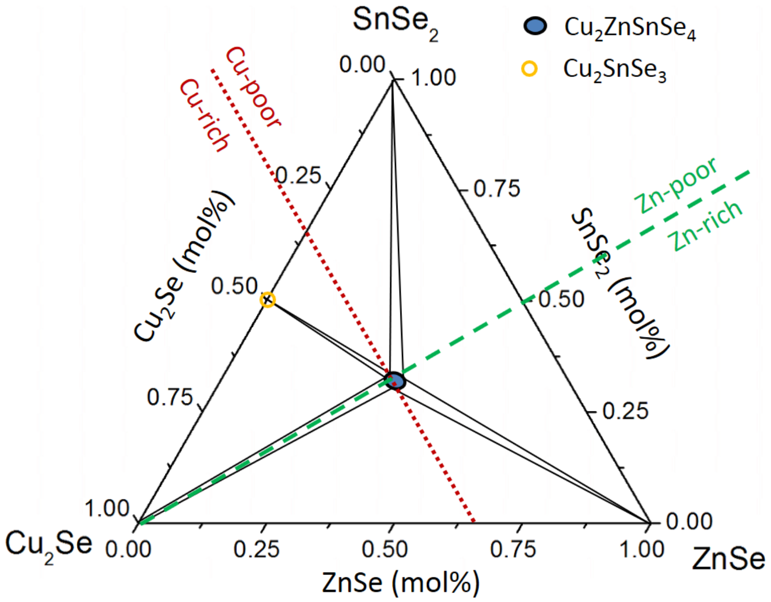

Figure 1.5: Isothermal section of the Cu_2Se-ZnSe-$SnSe_2$ system at 670K (adapted from [36]**). The red dotted line indicates all compositions with Cu/(Zn+Sn)=1, and the green dashed line indicates Zn/Sn=1. Domains of Cu-poor/Cu-rich and Zn-poor/Zn-rich are delimited by these two lines, as described on the figure.**

At the normal temperatures employed for the synthesis of Kesterite (500-600°C), some species have a high vapor pressure (SnSe and Se), which can cause decomposition of the Kesterite if the background pressure of the gaseous species is not sufficient. The decomposition reaction 1.4 was reported by Redinger et al. [38]:

$$Cu_2ZnSnSe_4(s) \rightarrow Cu_2Se(s) + ZnSe(s) + SnSe(g) + \frac{1}{2}Se_2(g) \qquad (1.4)$$

At 550°C, the saturation partial pressure of SnSe is around 3.6x10^{-3} mbar which is relatively high, thus decomposition of Kesterite can occur if the partial pressure of SnSe in the environment is not sufficient. This is why the selenization processes need to be done in the presence of additional Sn or SnSe, to provide a sufficient background pressure of SnSe, in order to maximize Kesterite formation. Partial pressures of ZnSe and CuSe at 550°C are respectively 6.4x10^{-15} mbar and 1.2x10^{-13} mbar [39], thus much lower than that of SnSe, and these phases do not pose problems of evaporation during the selenization process.

1.4 Objectives and structure of the thesis

This thesis investigates the synthesis of Kesterite thin films for their implementation as absorbers into solar cell devices. The layers are prepared via the two-step method presented previously: metallic layers containing Cu, Sn and Zn are first deposited, and then these films are converted to Kesterite by a reactive annealing step during which selenium is incorporated in the layers. The choice of a sequential deposition of metals was mainly motivated by the fact that this method offers a very easy control of the stoichiometry of the samples, which is of great importance to control the secondary phases formed during the selenization. The specificity here is to perform the deposition of metals via electrochemical methods, which already gave very good results (record power conversion efficiency of 7.2% [40] at the beginning of this thesis, which then was increased to 9.1% [41] at the time of writing the thesis) and offer the strong advantage of being a low energy cost and high material efficiency process, if used industrially. Metallic stacks of Cu/Sn/Zn are electrodeposited onto glass/Mo substrates, which are then selenized via annealing at 550°C in presence of Se to form Kesterite. An intermediate step of annealing at 200-350°C (prealloying step) prior to selenization is optionally investigated. It is mainly used in this thesis to study the effects of alloying of the metals before the incorporation of selenium in the thin films. For the fabrication of solar cells, the layers are selenized directly after the electrodeposition without prealloying step, except for a few cases which will be indicated. This choice was made in order to reduce the number of process steps and then potentially decrease the variability of the process. The absence of this step could also be a good point for the transfer of the process to industry.

As explained in the previous section, the formation of Kesterite secondary phases is a major problem for the fabrication of efficient solar cells. Thus one of the main objectives of this thesis will be to investigate the formation of secondary phases, to study which ones are present, and where they form in the layers. In this frame, two main objectives will be followed. The first is based on the work of Arasimowicz [42], who investigated a very similar process of fabrication and presents results where ZnSe is the main secondary phase present, whereas the stoichiometry of the precursor layer should lead to a material containing ZnSe and SnSe. Therefore, one goal is to investigate if the same phenomenon occurs with the process used for this thesis, and in this case understand why SnSe is absent from the layers after selenization. With sulfide Kesterite, which has a close chemistry to the selenide Kesterite, a similar behavior is observed [43], and was explained by a mechanism of self-regulation of tin content via evaporation of tin sulfide which allows to end with the exact quantity of tin required to form Kesterite. Our objective for this is then to compare the behavior of Sn in the selenide system and compare it with the results of Johnson et al.

A second motivation for this thesis is the investigation of the effect of segregation mechanisms occurring during the heating of metallic samples at 200-350°C. This segregation is due to the very low miscibility of Zn and Sn, which lead to the segregation of Cu-Zn and Cu-Sn alloys after alloying of the metals. Several reports show that different microstructures of metal layers can be obtained by heating different types of metal stacks (a Mo/Cu/Sn/Cu/Zn precursor will lead to a bilayer Mo/CuSn/CuZn, whereas Cu/Sn/Zn leads to a columnar structure of CuSn and CuZn [44] in the same alloying conditions). These different microstructures have then an influence on the segregation of secondary phases in the [44]. Strong improvements of power conversion efficiencies were achieved by using an intermediate step just before the selenization in order to alloy the metals and have the required microstructure of precursor. However, evidence of the influence of precursor microstructure was only done by comparing very different types of samples (e.g. bilayer vs columnar type), and by studying the samples at a scale of a few micrometers which is too small to observe the distribution of the alloys. Thus, the objective here is to study the effect of prealloying on the segregation of metals at microscopic scale, and then to study the effect of this segregation on the formation of ZnSe and on its segregation. The hypothesis here is that alloying occurs during the process investigated for the thesis, even if no annealing step at 200-350°C is performed prior to selenization: alloying occurs during the heating ramp of the process of selenization, before incorporation of selenium in the layer. The second hypothesis is that after alloying occurred, the separation of Zn and Sn can not be reversed during the incorporation of selenium, which can explain why large aggregates of secondary phases are present after this process.

Additionally, attention will be brought to the understanding of the effect of ZnSe on the performance of solar cells. Previous work from Watjen et al [45] shows that surface ZnSe affects mainly the short circuit current of the solar cells by acting as a barrier between the absorber and the CdS, because of its resistivity [37]. However, this study from Watjen et al only shows results on a single sample and compares local variations of current on areas where ZnSe is more or less present. Thus the objective for this thesis is to investigate this effect on different samples which have different amounts of ZnSe, and find at which composition the short circuit current of the solar cells is the highest. A hypothesis that can be made is that in the range of compositions investigated (Cu-poor and Zn-rich), the short circuit will be increasing when the quantity of zinc is decreasing, but only to a certain point, after which the composition becomes too close to stoichiometry and other types of secondary phases appear, due to the local inhomogeneity of metals in the precursor metallic layer. For instance, Cu_2Se or Cu_2SnSe_3 could be expected, which are harmful for the solar cells.

In order to facilitate the understanding of the results obtained while investigating these different points, they will be presented in three chapters (3 to 5) following the order of the process of synthesis of the solar cells. Chapter 3 will present all results concerning the electrodeposition of Cu/Sn/Zn stacks, and results on the investigation of the effect of alloying of the metals. The work presented is a continuation of works realized by Berg [46] and Arasimowicz [42], thus the changes brought to their processes will be presented first, with the consequences of these modifications. Then, the specificities of the layers electrodeposited will be detailed, in terms of morphology and composition at macroscopic and microscopic scale. This chapter will be concluded by an investigation of the alloying of the metals in these layers. The formation and segregation of alloys of Cu-Sn and Cu-Zn at a rather large scale is discussed.

Chapter 4 investigates the selenization mechanism, and is divided into three parts: a) investigation of the mechanism of formation of kesterite and its secondary phases, where alloying prior to incorporation of selenium will be discussed, as well as tin self-regulation; b) investigation of the change of composition after selenization, which enables to clearly identify the mechanism of Sn self-regulation; c) investigation of the effect of segregation of metals before selenization on the segregation of ZnSe secondary phase.

Chapter 5 is devoted to the analysis of the solar cells into which the Kesterite absorbers are implemented. A first study of kesterite composition is done to investigate the effects of the presence of different amounts of zinc selenide in the absorber layers. An analysis of the variation of fill factor and open circuit voltage is then done, and finally an improvement of open circuit voltage of the solar cells by performing an alloying step before the selenization is presented.

2 Fabrication and characterization methods

Aim of the chapter

This chapter presents first all methods of fabrication of the solar cells: substrate used, deposition of metals, prealloying, selenization and completion into devices. The methods of characterization of the thin films are detailed as well. The technique of identical location analysis which was developed for this thesis is presented, together with more conventional methods of imaging, elemental analysis and phase identification. Finally, methods of opto-electrical characterization of the solar cells are described.

2.1 Fabrication of absorber layers and solar cells

The Kesterite absorber layers are fabricated in three main steps: i) Cu/Sn/Zn stacks are electrodeposited on glass-Mo substrates, ii) optionally the layers are heated to alloy them and iii) the precursor is heated in a selenium and tin selenide atmosphere. Then, the solar cells are completed by deposition of the buffer layer (CdS), the window layer (i-ZnO and Al-doped ZnO) and the metallic contact grids.

2.1.1 Electrodeposition and alloying of Cu-Sn-Zn precursors

(a) Electrodeposition of Cu/Sn/Zn stacks

Cu, Sn and Zn layers are sequentially deposited on the glass/Mo substrates to obtain stacks of glass/Mo/Cu/Sn/Zn.

Basics of electrodeposition:

The method of electrodeposition is relatively simple and can be described by considering the schematic of figure 2.1. It consists to apply a potential difference between two electrodes immersed in a solution (electrolyte), in order to reduce metallic ions dissolved in the electrolyte, and form a metallic layer on the negative electrode.

The general equation of a redox reaction is $Ox + ne^- \rightarrow Red$, with Ox and Red respectively the oxidized and reduced agents of a certain redox couple. In case of a metal M, present in solution in a +z oxidized state, this equation becomes:

$$M^{z+}_{solution} + ze^- \rightarrow M_{solid}. \qquad (2.1)$$

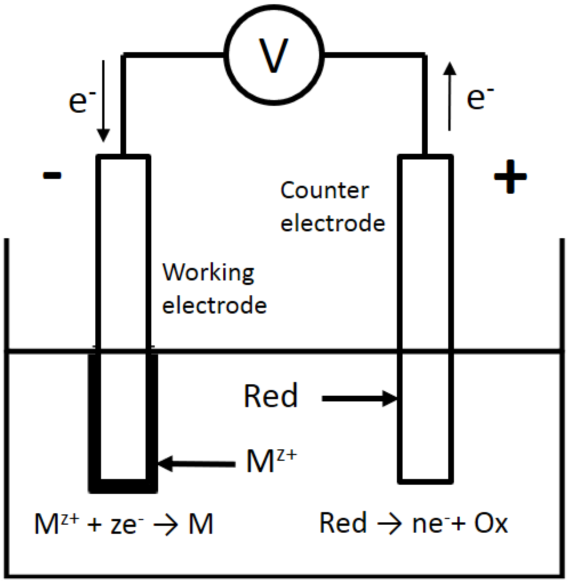

Figure 2.1: Schematic drawing of a two-electrode electrochemical cell.

When the potential difference between the negative electrode (working electrode) and the positive electrode (counter electrode) is sufficient to allow the two reactions to occur, the reduced species Red will be oxidized at the counter electrode, and the metal ions M^{z+} will be reduced at the working electrode, which will cause the deposition of M metal on this electrode. The global equation is as follows (equation 2.2):

$$nM^{z+}_{solution} + zRed \rightarrow nM_{solid} + zOx \qquad (2.2)$$

The reducing agent Red which is oxidized at the counter electrode can be either the metal of the cathode, or an ion in solution, or the solvent itself.

For the redox couple M/M^{z+}, when the reaction 2.1 is at equilibrium (zero current), the Nernst equation 2.3 describes the potential of the solution for a certain ratio of concentration of each species.

$$E_{eq} = \mathrm{E}^0_{\mathrm{eq}} + \frac{\mathrm{RT}}{\mathrm{zF}} \ln\left[\frac{a_{M^{z+}}}{a_M}\right] \qquad (2.3)$$

In equation 2.3, E^0_{eq} is the standard potential, R is the universal gas constant, T is the absolute temperature, a is the chemical activity for the relevant species, F is the Faraday constant (the number of coulombs per mole of electrons: $F = 9.648\times10^4$ C mol^{-1}), and z is the number of electrons transferred.

When the potential is more negative than E_{eq}, the formation of the metal (reduction reaction) is favored. The overpotential η needed to obtain a certain current I is then defined as $\eta = E(I) - E_{eq}(0)$, and depends on three different parameters: $\eta = \eta_{ct} + \eta_{cr} + \eta_{conc}$ with η_{ct} , η_{cr} and η_{conc} being overpotentials due respectively to charge transfer, matter transport and crystallization.

The number of moles of metal deposited $n_{M^{z+}}$ can be controlled by counting the charge q passed in the circuit during the process with equation 2.4.

$$n_{M^{z+}} = \frac{q}{zF} \tag{2.4}$$

However, parasitic reactions can occur during the deposition, such as the reduction of another species in solution, or hydrogen evolution ($2H_2O + 2e^- \rightarrow H_2 + 2OH^-$). Thus, the plating efficiency for each metal on a specific substrate needs to be determined first in order to grow a layer with the desired thickness.

Electrodeposition with a three-electrode setup:

For the specific application of deposition of thin films on substrates of a size of a few centimeters, a three-electrode setup with a rotating disk electrode for the working electrode is used, as described in figure 2.2. It allows a better control of the process compared to a static electrodeposition. In this configuration, a third electrode is added, which has a constant potential. It is used as a reference to measure the potential of the working electrode during the deposition process. This setup offers the advantage to work under constant potential at the working electrode. Furthermore, an electrode which allows to rotate the substrate during the electrodeposition (the center of rotation is the center of the sample) is used. It is referred to as a “rotating disk electrode” and is used to create a flow of electrolyte to the surface of the sample in order to obtain a homogeneous deposition of metals over the sample area and increase the mass transport of solution to the surface of the working electrode, thus allowing a fast replenishment of the metal ions in the vicinity of the growing metallic layer.

For the synthesis of Cu/Sn/Zn layers, Cu, Sn and Zn thin films are sequentially electrodeposited on glass/Mo substrates using the setup described in figure 2.2. The glass/Mo substrate is attached and electrically connected to a disk electrode rotating at 300 rpm, with the Mo layer facing down (in contact with the solution). A view of the rotating disk electrode from below is shown in figure 2.3a. An adhesive tape is placed around the edges of the sample and on the electrode in order to i) ensure electrical contact between the Cu contacts and the molybdenum, ii) also to define the deposition area, iii) isolate the electrical contact from the electrolyte. The counter electrode is a platinum wire (99.9%, Mateck, diameter of 1 mm, 2cm immersed in the electrolyte). The reference electrode is a saturated calomel electrode (E=+0.241 V vs normal hydrogen electrode) from Radiometer Analytical.

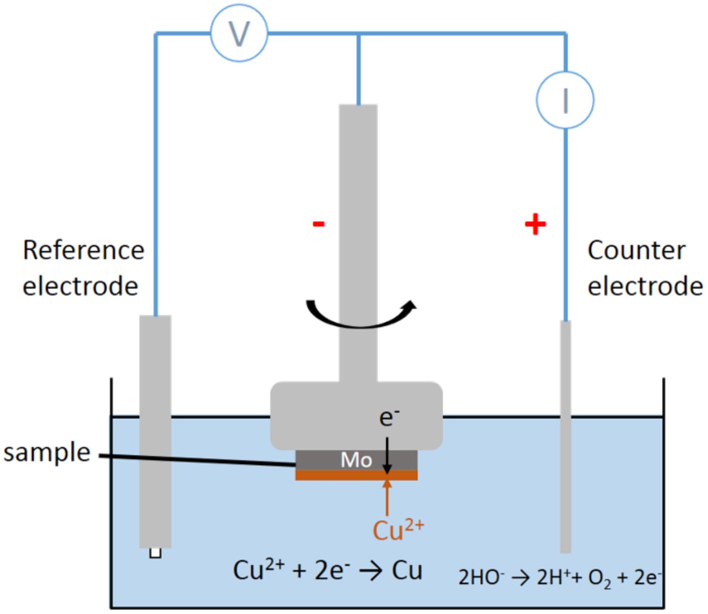

Figure 2.2: Electroplating cell composed of a reference electrode, a rotating working electrode (in the center) supporting the sample, and a counter electrode. All electrodes are immersed in an aqueous solution, called electrolyte. Here is described the example of the deposition of a copper layer: Cu^{2+} ions dissolved in the solution are reduced at the surface of the sample to form the Cu layer.

All the electrodes are immersed in an electrolyte containing cations of the metal to be deposited, in a 100 mL beaker. The Cu layer is electrodeposited from an aqueous electrolyte containing 3 M NaOH (99.99%, Sigma Aldrich), 0.2 M Sorbitol (99%, Sigma Aldrich), 0.1 M Cu (II) sulfate hydrate (99.999%, Alfa Aesar), and 0.932 mM Empigen BB detergent (Sigma Aldrich). The Sn layer is electrodeposited from an aqueous electrolyte with 1 M methanesulfonic acid (>99.5%, Sigma Aldrich), 50 mM Sn(II) methane sulfonate (Sigma Aldrich), and 3.6 mM Empigen BB detergent (Sigma Aldrich). Finally the Zn layer is electrodeposited from an aqueous solution containing 3 M KCl (99.995%, Alfa Aesar), 50 mM $ZnCl_2$ (99.999%, Alfa Aesar), 1 g pH3 Hydrion buffer (Sigma Aldrich), and 0.2g of Poly[bis(2-chloroethyl) ether-*alt*-1,3-bis[3-(dimethylamino)propyl]urea] quaternized (solution 62 wt. % in H_2O, Sigma Aldrich). These electrolytes were developed by Scragg and Berg [46], [47].

The depositions are performed under constant electric potential at the working electrode. The potentiostat used for the process is an Autolab PGSTAT302N. Metal ions dissolved in the electrolytes are reduced at the surface of the working electrode and form the metal layers ($M^{z+} + ze^- \rightarrow M$). The thickness of the metal layer is controlled by the charge passed during the process. After sequential electrodeposition of Cu, Sn and Zn layers, the as deposited samples are as described in figure 2.3b.

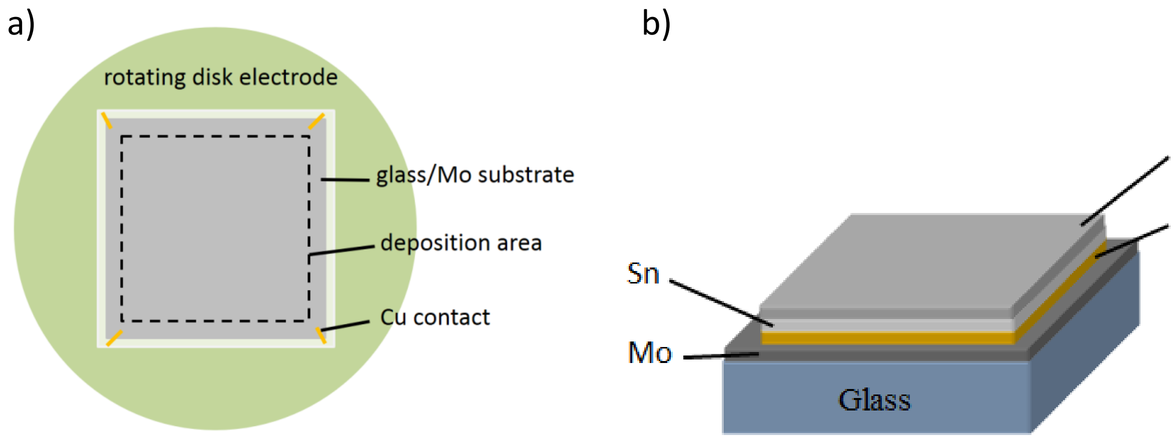

Figure 2.3: Schematic of (a) glass/Mo substrate mounted on rotating disk electrode (RDE), seen from below. All the area outside the dotted square is covered with adhesive tape to isolate connecting wires from the electrolyte. (b) schematic of Cu/Sn/Zn stack on glass/Mo substrate after electrodeposition.

(b) Optional prealloying step

In a few specified cases, the as-electrodeposited metal stacks are annealed under 1 bar nitrogen at 350°C in a rapid thermal processing (RTP) oven (AS-one100, Annealsys). Fast heating and cooling ramps are used with this type of oven, of typically 10°C/s for heating, and 0.7°C/s for cooling. This step is optional and aims at mixing the metals to form alloys of Cu-Sn and Cu-Zn. It is not performed for all samples.

2.1.2 Selenization of Cu-Sn-Zn thin films

The selenization process consists of a reactive annealing at 500-600°C in presence of Se and SnSe powders, which react with the metals of the Cu-Sn-Zn layer to form selenide compounds. To this end, the glass/Mo/Cu-Sn-Zn samples are placed inside a graphite chamber, together with 100 mg of selenium powder (99.999%, Alfa Aesar) and 15 mg of tin selenide powder (99.999%, Alfa Aesar). A background pressure of 10 mbar of forming gas (10 vol% H_2 in N_2) in the oven is used. The graphite box is heated to the target temperature and kept at this temperature during a certain time (0-30 min) to perform the selenization. This reactive annealing can be performed with two different types of oven: a tube furnace, and a RTP oven. The main differences between these ovens are the heating and cooling ramps (the RTP can perform much faster ramps), and the configuration of the oven (shape, size of the box, type of heating…). These specificities are listed in the following.

Tube furnace selenization:

A tube furnace oven is used for all “standard” processes, and was used for the selenization of all the samples presented in this thesis, except for section 4.2 (the use of a different oven is clearly specified in this section). A schematic description of the oven is shown in figure 2.4.

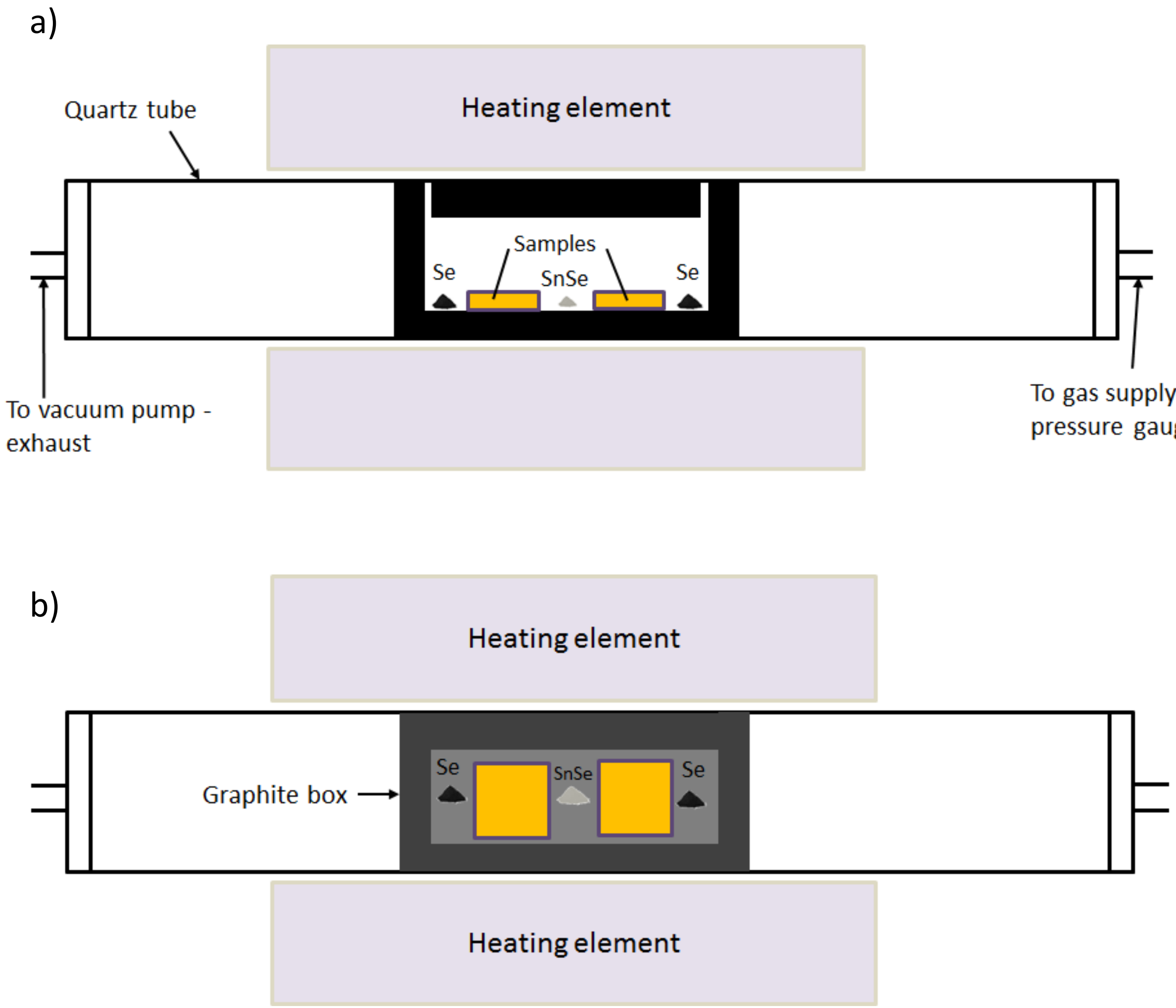

Figure 2.4: Design of tubular oven with graphite box containing two 2.5x2.5 cm^2 samples and powders of Se and SnSe: (a) side view, (b) view from above.

Two samples are annealed together in a selenization process. SnSe powder is placed between the two samples, and Se powder at the edges of the graphite chamber. This configuration was found to give the best results. During a process, the temperature is increased to 100°C, and kept at this value for 30 minutes. During this time, several flushes of nitrogen and forming gas are done, in order to remove any residual water or solvent (isopropanol is used to clean the oven). The temperature is then raised to the target value at a rate of 18°C/min. This temperature is held for the desired time, and the oven is left to cool naturally to room temperature during three hours. The standard selenization process is done at 550°C for 30 minutes.

Rapid thermal processing (RTP) oven:

The design of this oven differs from the tubular oven, as described in figure 2.5. The heating is from above the chamber, and cooling can be performed from under the graphite box. This oven allows faster ramps of heating and cooling than the tubular furnace. Typically, the heating ramp is 10°C/sec and the cooling ramp 0.7°C/sec.

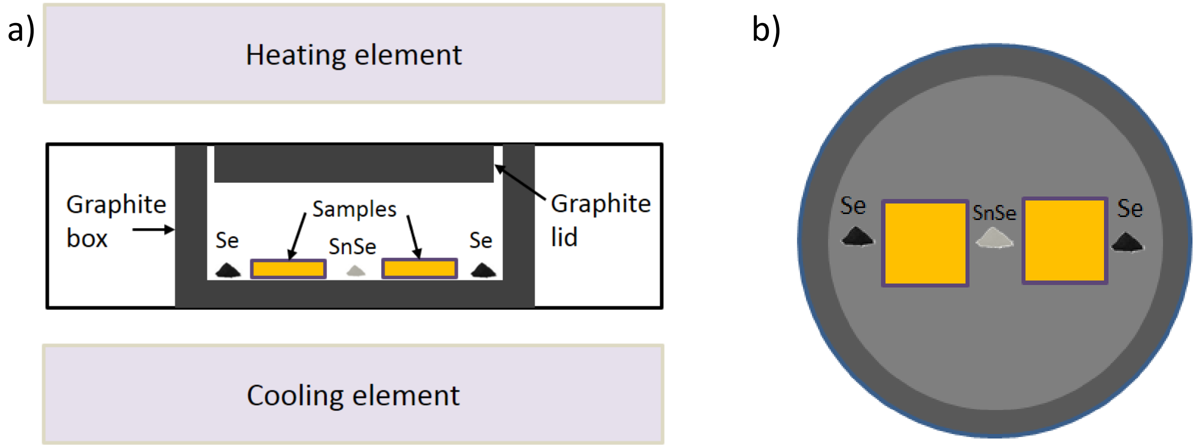

Figure 2.5: (a) Design of RTP oven, side view, (b) graphite box of RTP oven, view from above. The samples represented in yellow have a size of 2.5x2.5 cm².

The standard selenization process using a RTP oven is done at 550°C for 5 minutes.

2.1.3 Fabrication of substrate and finalization of solar cells

The fabrication of glass/Mo substrates and the implementation of selenized samples into solar cell devices are standard processes, performed by an ingeneer at the University of Luxembourg. They are briefly described in this section.

(a) Substrate

Soda-lime glass (SLG) slides of 2.5 x 2.5 cm² size and 2 mm thickness are used as substrates. A molybdenum layer of 500 nm thickness is sputtered on the glass. The Mo target purity is >99.95% (AJA International Inc.). Prior to the deposition of Cu/Sn/Zn layers, the glass/Mo samples are etched in ammonia (>25%) for three minutes, in order to remove molybdenum oxides from the surface. These oxides are removed to increase the conductivity of the substrate and avoid drops of electric potential at the surface during the electrodeposition.

(b) Completion into solar cells devices

After selenization of the Cu-Sn-Zn layers, completion into full devices was done by etching the absorbers surface with aqueous KCN in order to remove residual Se and Cu_xSe phases. Subsequently, CdS is deposited by chemical bath route, i-ZnO, and Al:ZnO layers were sputtered and finally a Ni/Al contact grid added. Contact grids were used for all solar cells, except for the cells of section 5.3.2. The size of the regular solar cells is 0.5 x 1 cm². Solar cells for mapping purposes have a size of 0.5 x 0.5 cm². Several solar cells can be made on a single sample, as shown on figure 2.6.

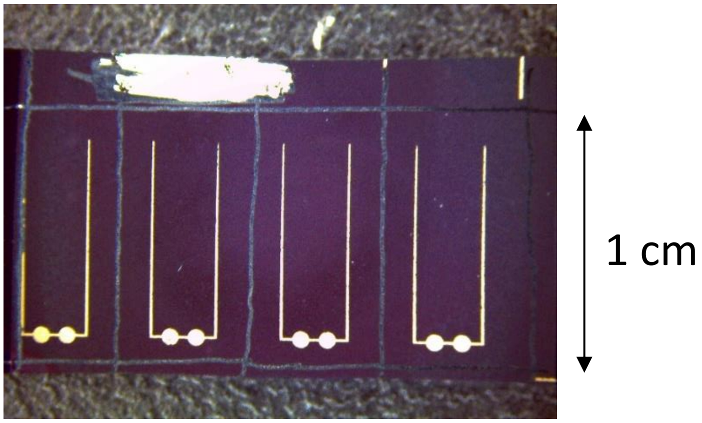

Figure 2.6: Example of solar cells made on a 2.5 x 2.5 cm² sample (the upper and lower edges of the complete sample have been removed).

2.2 Characterization techniques

2.2.1 Identical location analysis

The Identical location (IL) technique enables the investigation of an identical location on a sample before and after a transformation. It was first presented in 2008 by Mayrhofer et al. [48], and used in their study to perform TEM analyses on a catalyst before and after electrochemical treatment. The method consists to use TEM grids as references to be able to retrieve the same place after the treatment.

The method seems useful to follow selenization mechanisms at microscopic scale, and especially to understand the origin of large scale segregation of ZnSe in the absorber layers (presented in chapter 4). However, the use of TEM grids is not possible, thus a simple technique to mark the surface of the samples was developed, as described in figure 2.7.

Two perpendicular lines are scratched into the sample. Inside three of the quadrants an additional scratch is placed (see figure 2.7a) in order to leave one clear identifiable quadrant, by the absence of a scratch.

Figure 2.7b shows a zoom of 2.7a with green lines indicating the edges of the scratch and a blue dashed box to indicate the area of interest, which is chosen far away from the marking lines to avoid any effect of these scratches during the selenization. The area of interest can be analysed by mapping techniques such as energy dispersive X-ray spectroscopy (EDX), micro photoluminescence (μ-PL), and μ-Raman. The precision in location of the area of interest was found to be in the order of 1 micrometer.

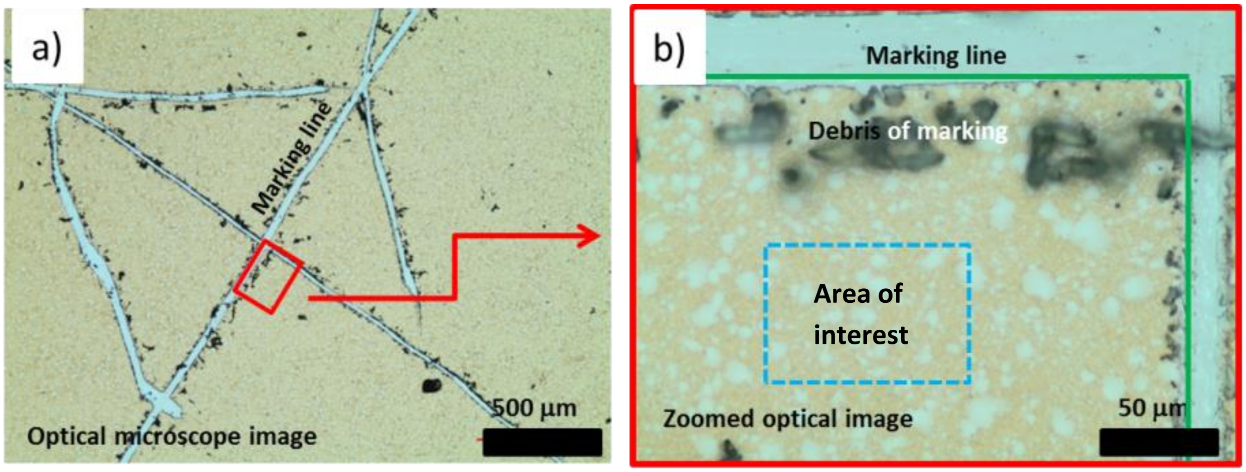

Figure 2.7: (a) Optical microscope image of a sample scratched with a cross and an additional scratch in three of the quadrants. (b) zoomed optical microscope image of the unscratched quadrant with blue dashed box showing the area of interest.

2.2.2 Characterization of thin films

This section presents the methods used for imaging, elemental analysis and phase analysis of a sample. For more information on these characterization techniques, please refer to the book "Advanced characterization techniques for thin film solar cells" [49].

Imaging:

The analysis of the morphology of the thin films was done by three different methods: optical microscope and scanning electron microscope (SEM) imaging.

The optical microscope used is a model BX51 from Olympus. The microscope is used in reflection mode, where the light source is a halogen lamp. The image of the sample is magnified by a system of lenses (UIS2 Optical System) and acquired via the software Olympus Stream.

SEM imaging is performed using a Hitachi SU-70. An electron beam is generated by the machine with an accelerating voltage of 7.0 kV. This electron beam is focused on the surface of the sample, to have a beam size of approximately 10-20 nm. Atoms from the sample are excited by the incoming electron beam and emit electrons, called secondary electrons. During the imaging, the area analyzed is scanned by the electron beam, and the secondary electrons are collected by a detector. This enables to create an image representative of the topography of the surface of the sample. Backscattered electrons can also be detected (with a different detector) during the scanning. These are electrons coming from the SEM electron beam, which are reflected from the sample by elastic scattering interactions with the atoms of the sample. Analysis of backscattered electrons provides an image of the composition of the sample. The sample can be analyzed in top view or cross section modes. Top view is a view of the surface of the layer, while cross section requires to cut the sample, and consists of observing the cut layer (observation of the layer in depth)

Cross section and top view images were also acquired with a dual column focused ion beam microscope (FIB, FEI HeliosNanolab). After SEM imaging of the surface, Pt e-beam deposition was used to define the cutting line on the sample's surface and to prevent damage to the layer during milling. An anion beam with 30 kV acceleration was used to mill and polish the cross section. The cross section was analyzed in the same dual column microscope, with an electron beam of 5 kV energy. The exact position of the cross section on the sample is ensured by the presence of the Pt stripe on the surface.

Bulk composition:

The chemical composition of the bulk material was analysed by energy dispersive X-ray spectroscopy (EDX Oxford Instruments INCAXMAX) using the same SEM machine (Hitachi SU-70), with an electron beam of 20 keV on areas of 400 x 400 μm^2, unless stated otherwise. Because of the excitation of the atoms of the sample by the electron beam, X-rays are emitted by the atoms. Each atom has specific X-ray radiations, thus the analysis of the X-rays allows to detect and quantify the elemental composition of the layers. Because of the high penetration depth of the incoming electrons at the acceleration voltage used, the interaction volume of the electrons in the samples is about 1 micrometer. Consequently, the resolution of the EDX measurement is approximately 1 micrometer. The presence of different phases at different positions in the depth of a sample can significantly affect the results obtained with this method, since most of the signal recorded originates from the surface of the sample, where most of the interactions between the electron beam and the sample occur.

In this thesis, the compositions of the films are mostly discussed in terms of molar ratios, with the following definitions (equations 2.5, 2.6 and 2.7):

$$x(Zn) = \frac{n(Zn)}{n(Cu)/2 + n(Sn) + n(Zn)} \qquad (2.5)$$

$$x(Sn) = \frac{n(Sn)}{n(Cu)/2 + n(Sn) + n(Zn)} \qquad (2.6)$$

$$x(Cu_2) = \frac{n(Cu)/2}{n(Cu)/2 + n(Sn) + n(Zn)} \qquad (2.7)$$

with *n(X)* amount of the metal X in moles.

These ratios are used to describe the metallic films, as well as the metal-selenide ones. The choice of Cu_2 instead of Cu is motivated by the easier description of the compositions in the pseudo-ternary system Cu_2Se-ZnSe-$SnSe_2$ proposed by Dudchak [36] (see ternary diagram of figure 1.5 in chapter 1). In this system Cu, Sn and Zn have the same oxidation state than in Kesterite (Cu +I, Zn +II, Sn +IV).

Another ratio which is extensively discussed in this thesis is the ZnSe ratio, which is defined in equation 2.8. It represents the molar fraction of ZnSe in the binary system (Kesterite + ZnSe).

$$\frac{ZnSe}{CZTSe+ZnSe} = \frac{Zn-\frac{Cu}{2}}{Zn} \qquad (2.8)$$

EDX mapping analyses were performed as well in the frame of the identical location analysis study presented in chapters 3 and 4. The dimensions of area analyzed are 65x48 μm^2. The obtained chemical composition maps were divided into 1.02 x 1 μm^2 units, which corresponds to the resolution of the method; thus it gives a total of 64 x 48 points for each map.

Composition depth-profile:

The compositional depth profile was analysed by secondary-ion mass spectrometry (SIMS). This analysis is done by sputtering the layer's surface with a focused ion beam. Secondary ions ejected from the samples are analyzed by a mass spectrometer to determine the elemental composition of the layer. The elemental composition is recorded as a function of the sputtering time, thus it gives an information on the depth profile of composition in the samples. However, this technique is non quantitative, thus it only allows comparisons of profiles of concentration. The profiles are always normalized to the maximum value.

Glow discharge optical emission spectroscopy (GDOES) is another method used for the determination of the profiles of composition in depth. Similarly to SIMS, the layer's surface is sputtered. Atoms ejected from the surface are then excited by a plasma. X-rays are emitted by these atoms when coming back to their fundamental energy, which are analyzed by an optical detector to determine the nature of the elements.

Phase analysis:

The phase analysis of the bulk material was examined by X-ray diffraction (XRD), with a Bruker D8 apparatus. This measurement is done to determine the atomic structure of the material under investigation. The sample analyzed is illuminated by a monochromatic beam of X-rays, which are diffracted in several specific directions by the crystals present in the films. These directions can allow to identify the structure of the crystals and the phases which are present. XRD measurements were performed in grazing incidence mode, where the position of the X-ray source is fixed, while the detector is moving.

The phase analysis at the surface of the samples can also be analyzed by Raman spectroscopy, up to a depth of less than 100 nm, depending on the wavelength of illumination. Monochromatic light is shining on the sample, and interacts with molecular vibrations of the material. As a result, the energy of the laser photons will be shifted up or down. This shift is giving information on the vibration modes of the system, and allow to characterize specific compounds. Raman and μ-Raman spectra were obtained by means of a Renishaw inVia Micro-Raman spectrometer.

The thickness of metallic layers was determined by X-ray fluorescence, which is a technique allowing the measurement of the composition of a sample. An X-ray photon beam is focused on the surface of the sample to analyze, which causes the ionization of some of the atoms of the material by ejection of an electron. In the ionized atoms, electrons in higher orbitals than the electron ejected will fall into lower energy states to finally reach the state which was occupied by the electron ejected. This decrease of energy of the electrons in the atom are accompanied by emission of photons (fluorescence). The energy of fluorescent photons corresponds to the difference of energy between orbitals of the element. Thus it is characteristic of the element and the elemental composition of the material can be detected. The machine is calibrated to provide metals thickness directly from the intensity of each element.

2.2.3 Electro-optical characterization of the solar cells

(a) **Basics of solar cells**

The electronic behavior of a solar cell can be described by the equivalent electrical circuit of figure 2.8. It contains a source of electrical current, which delivers a continuous current density J_{ph}, a diode in parallel of this source of current and two resistances, one in series and the other in parallel. The series resistance models the electrical resistance of the materials where the current is flowing, while the parallel (shunt) resistance models shunt paths which can exist in the solar cells, due to pinholes, conductive phases in the absorber, or defects of the crystal. To achieve good efficiencies, R_s needs to be as low as possible and R_p the highest possible.

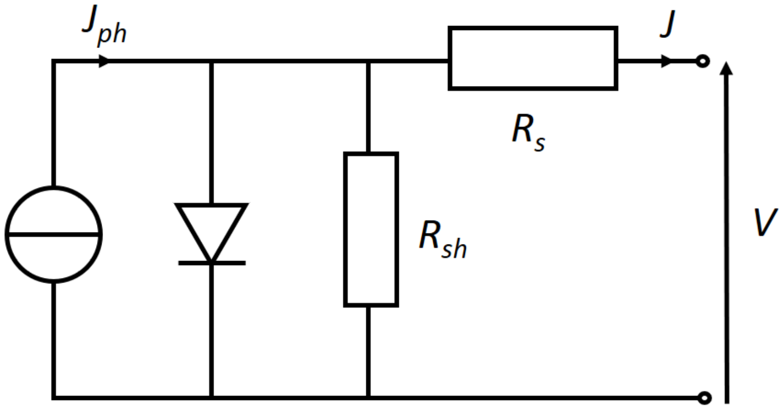

Figure 2.8: Equivalent circuit of a solar cell.

Equation 2.9 describes the relationship between the current density and the voltage applied to the solar cell, under illumination.

$$J = J_{ph} - J_0 exp\left(\frac{q(V+JR_S)}{AkT}\right) - \frac{V+JR_S}{R_{sh}} \tag{2.9}$$

where V denotes the applied voltage, J_0 the dark saturation current density, q the electron charge, A the diode ideality factor, k the Boltzmann constant, T the absolute temperature, J_{ph} the light generated current density, and the parasitic R_s (series) and R_{sh} (parallel) resistances. Electrical currents are described in current density (in A/cm^2), which corresponds to the current delivered by the solar cell (A) divided by its total area.

A typical current density-voltage (JV) curve is presented in figure 2.9. As described in chapter 1, the rectangle F is taken at the J and V values for which the power J×V is maximum. The important parameters are the open circuit voltage V_{oc}, which is the voltage obtained when no current flows, the short circuit current density and the fill factor. The fill factor is the ratio of the area of the rectangle F versus the area of the rectangle E. It describes the squareness of the JV curve.

The power conversion efficiency (η) of the solar cell is calculated as the ratio of the power output versus the power input (power of light), as in equation 2.10.

$$\eta = \frac{J_{\max}.V_{\max}}{P_{input}}. \tag{2.10}$$

It can be calculated using the values of fill factor, V_{oc} and I_{sc} as follows: the fill factor is defined in equation 2.11.

$$FF = \frac{J_{\max}.V_{\max}}{J_{sc}.V_{oc}} \tag{2.11}$$

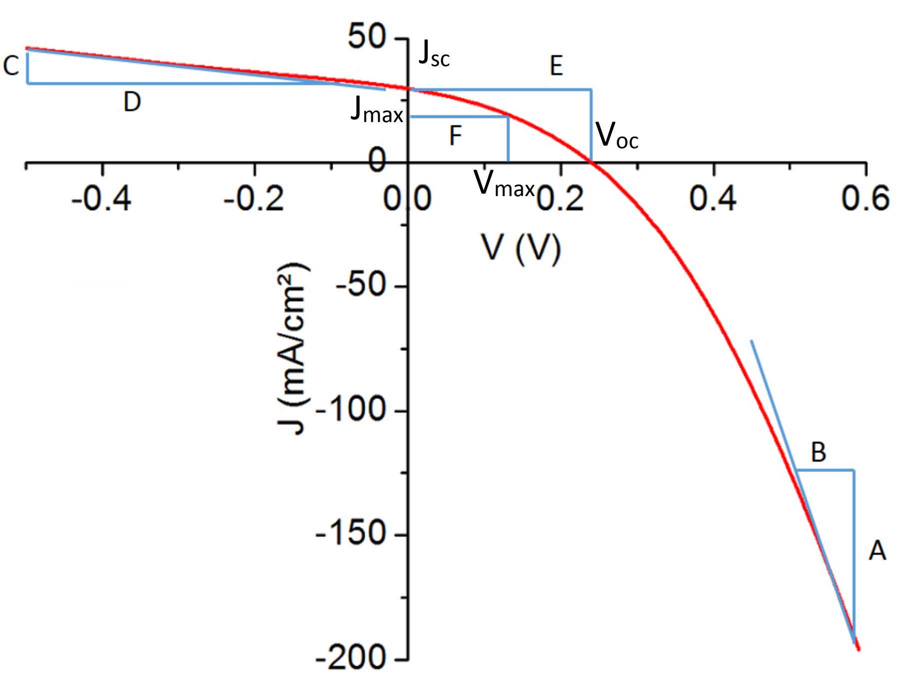

Figure 2.9: Typical JV curve measured under illumination (red curve).

Finally the efficiency can be written as in equation 2.12.

$$\eta = \frac{FF.J_{sc}.V_{oc}}{P_{input}} \tag{2.12}$$

The series and shunt resistances can as well be derived from this type of curve. The series resistance is calculated as $R_s = \frac{B}{A}$ and shunt resistance as $R_{sh} = \frac{D}{C}$ (see equation 2.9).

The second characterization technique is the quantum efficiency (EQE). An example is given in figure 2.10. It measures the proportion of current collected (compared with the intensity of the light) for a certain wavelength. It allows to understand the photocurrent collection and find the causes of current losses.

The right edge (highest wavelengths) of the curve is due to the limit of absorption of the absorber, and allows to determine its bandgap. The left edge is due to absorption of the TCO and buffer layer. For further information about the characterization of a solar cell, the reader is invited to refer to [50].

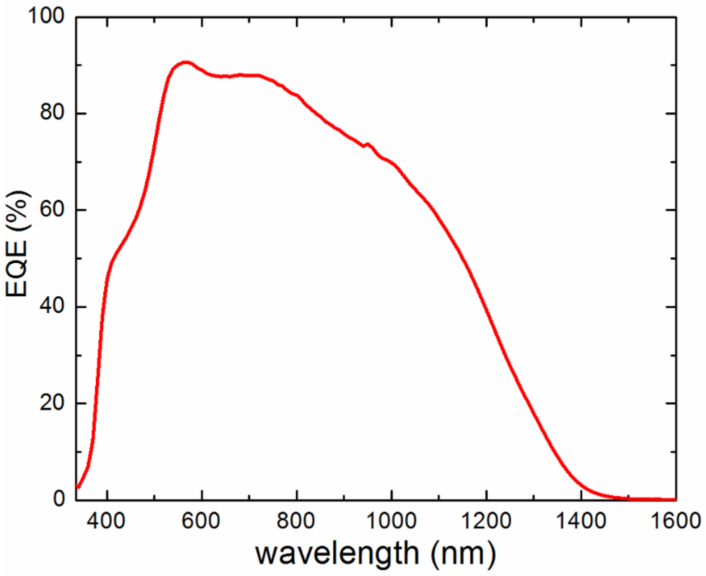

Figure 2.10 : External quantum efficiency curve of a Kesterite solar cell.

(b) **Methods of analysis**

Current-voltage characteristics are measured with a home-built setup. A halogen lamp (100 mW/cm²) is used to simulate the AM1.5 spectrum. The measurement is calibrated by measuring the short circuit current of a certified reference silicon solar cell. Details on I-V characteristics will be given in the introduction of chapter 5.

A software developed by Thomas Weiss (University of Luxembourg) is used to fit the current-voltage (J-V) characteristics obtained, and extract values of series resistances, shunt resistances, as well as diode factors. Details on the fitting methodology can be found in a publication of Burgers et al. [51].

External quantum efficiency (EQE) measurements were performed using a home-built setup, using a Xenon and Tungsten lamp as light sources. The beam area is 1x1 mm². The system is calibrated by the measurement of a silicon and a InGaAs photodiode.

3 Preparation of metallic Cu-Sn-Zn precursors

Aim of the chapter

This chapter is devoted to the study of the synthesis of Cu-Sn-Zn metallic precursors. The developed process of electrodeposition of Cu/Sn/Zn stacks is presented first, including the specificities of each of the layers that constitute the stack, in terms of morphology and composition. The second part investigates the effects of metals alloying in the precursors leading to the formation of Cu-Sn and Cu-Zn phases. Especially this latter section aims at studying the spatial reorganization of the metals caused by the alloying.

3.1 Introduction: electrodeposition and alloying of Cu-Sn-Zn thin films

3.1.1 Background

Electrodeposition for photovoltaics:

Electroplating is a technique that allows the deposition of a layer of metal or semiconductor on the surface of a conductive material. The method was already in use around 200 BC in Peru, for the deposition of gold on copper by electroless plating (without external source of electric current) [52]. Modern electroplating started in 1805 with the work of Luigi Brugnatelli, who performed electrodeposition of gold using the Voltaic Pile invented in 1800. Nowadays, there are many industrial applications of this technique, such as the deposition of anti-corrosion layers, or decorative plating (gilding or chrome plating).

The use of electrodeposition in photovoltaics was motivated by the possibility to prepare thin films of a few hundred nanometers relatively easily, with a high control of the thickness, which allows the deposition of metals or semiconductors for thin film solar cells. Furthermore, this process is easily upscalable, which is a great advantage for further development of the process at industrial scale. In the field of Kesterite solar cells, the use of electrodeposition is rather recent: in 2008 and 2009 were reported stacked electrodeposition [53], [54] and co-electrodeposition [55] of Cu-Sn-Zn for fabrication of CZTS solar cells, followed by a high temperature treatment in presence of sulfur. A first power conversion efficiency of around 1% was achieved using stacked electrodeposition [54]. This efficiency rapidly increased to 3.2%, reported by Scragg et al. in 2010 [47]. In 2012, a breakthrough was achieved by Ahmed et al. who published a 7.3% efficient CZTS solar cell [40], and Guo et al. with a 7% CZTSe solar cell [56], both introducing a new prealloying step between the electrodeposition and the selenization/sulfurization. More recently, Vauche reported a 9.1% efficient CZTSe solar cell. The increase of efficiency was made possible by working on post selenization treatments (etching and prealloying), and buffer layer optimization [41], [57]. For more details on the electrodeposition of Kesterite thin films, review articles of the activity are available [18], [26].

Concerning the electrodeposition process, sequential deposition of only the metals is the most commonly used for Kesterite solar cells. Different stack orderings have been explored, however because of their different standard reduction potentials ($Cu^{2+}/Cu = 0.34V$; $Sn^{2+}/Sn = -0.14V$; $Zn^{2+}/Zn = -0.76V$ vs. NHE [58]), only the sequence Mo/Cu/Sn/Zn avoids issues of metal exchange and reduces problems of layer stripping during the sequential electrodepositions. An alternative to this process, that was already mentioned briefly, is the so-called co-electrodeposition which consists of electrodepositing several metals or all metals at the same time. A power conversion efficiency of 8% was reported [59], by co-electrodepositing a Cu-Sn-Zn precursor.

Other types of electrodeposition processes have been investigated, as described in the review by Colombara et al. [18]: co-electrodeposition of Cu, Sn and Zn or co-electrodeposition of Cu, Sn, Zn, S or Se. Although a very good result of 8% power conversion efficiency achieved by selenization of a co-electrodeposited Cu-Sn-Zn layer [60], these techniques still have strong disadvantages compared to sequential depositions. The fact that each element has different deposition potentials, different diffusion coefficients and different pH range stabilities makes the choice of the electrolyte chemistry very tricky. Furthermore, sequential electrodeposition offers the advantage to have a very easy control of the stoichiometry of the material, by simply changing the relative thickness of the layers. For these reasons, in this thesis only a sequential Cu/Sn/Zn deposition was used.

Alloying of Cu-Sn-Zn thin films:

In the most usual case of a sequential deposition method, the films have a strong vertical composition gradient. To alloy the metals and thus improve inter-mixing of the elements, treatments at temperatures of 200°C to 350°C have been reported [40], [44], [57]. Other beneficial effects of this treatment can be the improvement of compactness, homogeneity and adhesion to the Mo layer [61]. However, for this thesis the majority of the solar cells were fabricated by directly performing the selenization step after the electrodeposition of Cu/Sn/Zn. The choice of not performing a deliberate alloying before the selenization was motivated by the necessity to keep the process as simple as possible and avoid potential sources of non-reproducibility. However, even by avoiding this annealing at 200-350°C, alloying of the metals is supposed to occur in the layers during the heating process of the selenization, before incorporation of the selenium, and its effects will be described in chapter 4.

Thermodynamic studies of Sn-Zn-Cu ternary system have been reported at 230°C [62], as well as 250°C and 600°C [63]. They show that under the conditions that are commonly used for alloying Cu-Sn-Zn precursors (annealing at 200 to 400°C), or for selenization (up to 600°C), a ternary compound Cu-Sn-Zn does not exist; only Cu-Sn and Cu-Zn are alloyed, and are slightly miscible with Zn (for Cu-Sn) or Sn (for Cu-Zn). The minimization of surface energy for these two coexisting alloy phases will then provide a driving force for many important phenomena such as sintering, wetting, and grain coarsening [64]. These phenomena lead to segregation of the metal alloys. Vauche et al. reported a bilayer morphology after annealing at 200°C, with Cu-Zn at the base of the film, and a Cu-Sn layer at the top. Their motivation to use low temperature annealings is to avoid the melting of tin which causes the formation of bumps in their layers. Arasimowicz et al. also reported the formation of a bilayer after annealing at 350°C of a Cu/Sn/Cu/Zn precursor [44]. In this specific case, the sequence of stack leads to the formation of Cu-Sn layer at the bottom (on the Mo), and Cu-Zn on the top. Another type of morphology, with vertical columns (from the bottom to the surface of the film) of Cu-Zn and Cu-Sn after prealloying was described by Ahmed et al. [40], and Arasimowicz et al. [44].

3.1.2 Objectives and structure of the chapter

At the start of this thesis, the best solar cells conversion efficiencies reported were 7.3% by Ahmed et al. [40] and 3.2% by Scragg et al. [47] for processes using electrodeposited precursors. Unfortunately, no detailed information on the process used by Ahmed was available, especially on the chemistry of the electrolytes used for the deposition of the metal stacks. The main difference between the works of Scragg and Ahmed is the sequence of the metallic stacks, namely Cu/Sn/Cu/Zn for Scragg and Cu/Sn/Zn for Ahmed. It was then hypothesized, based on the work of Arasimowicz [42], that obtaining a Cu/Sn/Zn stack was the key point to achieve high efficiency. Thus the first objective which is presented in section 3.2 is the investigation of modifications of the process developed by Scragg to achieve a Cu/Sn/Zn stack.

The following section (3.3) aims at describing the layers that are produced with the modified process, and compare them with electrodeposited layers presented in the literature. The properties investigated are the homogeneity of the thickness over the area, the roughness, and the compactness of the films. This part is more descriptive and aims at giving the reader a good understanding of the properties of the samples that are produced with the electrodeposition method. Most reports in the literature are concentrated on describing the layers at a scale of about 10 micrometers. This section 3.3 compares the properties of the layers obtained with this literature, and will as well provide further information on the layer's properties at a scale of more than 50 micrometers, which will then be of importance to investigate the segregation of metals during alloying.

The last section aims at investigating the effects of the alloying of Cu, Sn and Zn metals on the homogeneity of the metals in the films. As described in section 3.1.1, the formation of alloys of Cu-Sn and Cu-Zn is known is the literature, and the formation of these alloys in Cu-Sn-Zn electrodeposited precursors was already reported [40], [42], [57]. However, the study of alloyed thin films at a larger analysis scale than previously is reported in section 3.4, and aims at investigating whether large segregations of metals could occur during the alloying. In order to investigate this, alloying of the metal stacks is deliberately done by annealing the layers at 350°C for 30 minutes. This study is done in the frame of the investigation of the hypothesis that the alloying leads to a segregation of the metals at microscopic scale, which then induces a segregation of ZnSe during the selenization of the metals. The segregation of ZnSe will then be studied in the chapter 4.

3.2 Electrodeposition process and stack ordering

3.2.1 Process modifications

At the start of the project, several groups already had achieved relatively high efficiencies by electrodeposition of metals and sulfurization or selenization. A best efficiency of 7.3% had been reported by Ahmed et al. [40] by selenization of an electroplated Cu/Sn/Zn stacked precursor. However, full details on the chemistry of the electrolytes are not available. Scragg et al. as well obtained efficient solar cells using different approaches, as described in table 3.1. They first reported an efficiency of 0.8% [65], using a stack Cu/Sn/Zn. However, they report a poor coverage by the Sn layer, which deposits with a very low nucleation density. Thus large grains of Sn are growing, but are too far from each other to coalesce at the end of the deposition, leaving empty spaces. The same group then improved their process by changing the tin solution chemistry [47], and achieved a dense and flat layer of this metal, which was a great improvement. However, they report strong difficulties to deposit zinc on the new type of tin. Thus, they opted for a different approach, and synthesized stacks of Cu/Sn/Cu/Zn, because of the possibility to achieve depositions of Cu on Sn, and of Zn on Cu. This led to a best power conversion efficiency of 3.2%.

Table 3.1: Summary of results obtained with different types of process. The compositions corresponding to each solution reference are summarized in table 3.2.

report	Cu solution reference	Sn solution reference	Zn solution reference	Drying after Sn	material	ordering	Reported device efficiency
Scragg [65]	Cu1	Sn1	Zn1	Yes	CZTS	Cu/Sn/Zn	0.8 %
Scragg [47]	Cu2	Sn2	Zn2	Yes	CZTS	Cu/Sn/Cu/Zn	3.2%
Berg [46]	Cu2	Sn2	Zn3	Yes	CZTS	Cu/Sn/Cu/Zn	
Arasimowicz [42]	Cu2	Sn2	Zn3	yes	CZTSe	Cu/Sn/Cu/Zn	1%
Crossay	Cu2	Sn2	Zn3	no	CZTSe	Cu/Sn/Zn	5% [66]

For this thesis, it was decided to try again to achieve a three-stack precursor, motivated by the recent results of Ahmed et al., and by the hope to reduce process steps and thus probably improve its reliability. For this, modifications of the process used by Scragg, Berg and Arasimowicz were done. One of the modifications was to avoid drying the layers between each deposition step, for two reasons: (i) avoid formation of stains on the layers, and (ii) avoid exposure of the layers to air. The electrolytes used are the same as those used by Berg and Arasimowicz (see tables 3.1 and 3.2). With this method, dense and covering thin films of zinc were achieved, and a power conversion efficiency of 5% was achieved by using the Cu/Sn/Zn layers, which was briefly reported in [66]. This was a large improvement, since selenide Kesterite solar cells from the Cu/Sn/Cu/Zn stack did not exceed 1%, as reported by Arasimowicz [44]. However, the reason for the ability to deposit zinc on tin remains unclear. A probable reason is that the new process avoids the formation of a resistive oxide layer on the surface of the tin, but the use of solution Zn3 instead of Zn2 which Scragg was using (see table 3.1) could also be the reason for this. The value of best efficiency was then increased to 5.9% by Arasimowicz, also by using a 3-stack Cu/Sn/Zn [42] and the same electrolytes.

This modified process was then used for the whole work presented in this thesis, and exclusively Cu/Sn/Zn stacked precursors were used.

Table 3.2: Electrolytes used for the deposition of Cu/Sn/Zn or Cu/Sn/Cu/Zn stacks.

Solution	Metal salt	complexant	Background electrolyte	surfactant
Cu1	$CuCl_2$	sorbitol	NaOH	
Cu2	$CuSO_4$	sorbitol	NaOH	Empigen
Sn1	$SnCl_2$	sorbitol	NaOH	
Sn2	$Sn(SO_3CH_3)_2$		CH_3SO_3H	Empigen
Zn1	$ZnCl_2$		pH3 buffer	
Zn2	$ZnSO_4$		K_2SO_4 + pH3	
Zn3	$ZnCl_2$		KCl + pH3	

3.2.2 Challenges of using Cu/Sn/Zn stacks

One of the main problems which appeared during the optimization of deposition parameters for the synthesis of the three-stack precursors is the formation of pinholes and delamination of the layer, mostly because of the need to deposit relatively thick copper layers (around 200nm). This is reported in the literature, and is probably due to hydrogen evolution (reaction 3.1) at the working electrode:

$$2H_2O + 2e^- \rightarrow H_2 + 2OH^- \qquad (3.1)$$

A pitting of the layers can be caused by hydrogen bubbles clinging to the surface where the deposition occurs. In these micropores, hydrogen can create a compressive stress as more and more gas accumulates [67].

Direct evidence of this phenomenon was observed by electroplating Cu, Sn and Zn on a Mo substrate which is static in the electrolyte (neither stirring the solution, nor rotating the sample). Bump-like features appear on the surface of the sample, as can be seen in figure 3.1a), which at some point break and bubbles of gas are released from the broken metallic layer. Bare molybdenum is then exposed, which shows that the hydrogen gas is forming between the molybdenum and the copper layer. The bumps observed are referred to as blisters in the following of this thesis. However, formation of large size blisters (figure 3.1a) was only observed for samples grown without stirring of the solution. In the case of samples grown using a rotating disk electrode, the flow of liquid on the surface of the sample is higher, which helps to remove hydrogen bubbles when they form. All samples presented in this thesis, except for the sample of figure 3.1a, are grown using a rotating disk electrode.

The formation of blisters can be described in different steps (figure 3.1b):

(i) Initiation of the blister: a bubble of hydrogen is stuck inside the Cu layer.
(ii) Growth: during Cu deposition, H_2 is formed preferentially in the vicinity of blisters already present, which grow. This occurs mainly during Cu and Zn deposition, which are done with the most negative deposition potentials.

Thus, optimization of the deposition potentials was done by trying to have the least negative possible values of potentials in order to decrease at most the formation of hydrogen, and avoid this problem of blistering.

Differences of behavior between samples grown under the exact same conditions were observed: some samples did not have any of these blisters, whereas others did, but no final explanation for this discrepancy of results was found. A possible explanation is that the molybdenum substrate could have micropores, which could “trap” gas bubbles (air remaining after introducing the layer in solution, or H_2 bubbles). Differences of wettability between Mo substrates were often observed, which could tend to validate this hypothesis of microstructure differences between Mo samples, but this still needs to be investigated. However, the formation of different amounts of blisters on different samples should not change the plating efficiency between the different samples: it was calculated that in the worse scenario observed, the amount of H_2 in the blisters was about 4 orders of magnitude lower than the amount of metals.

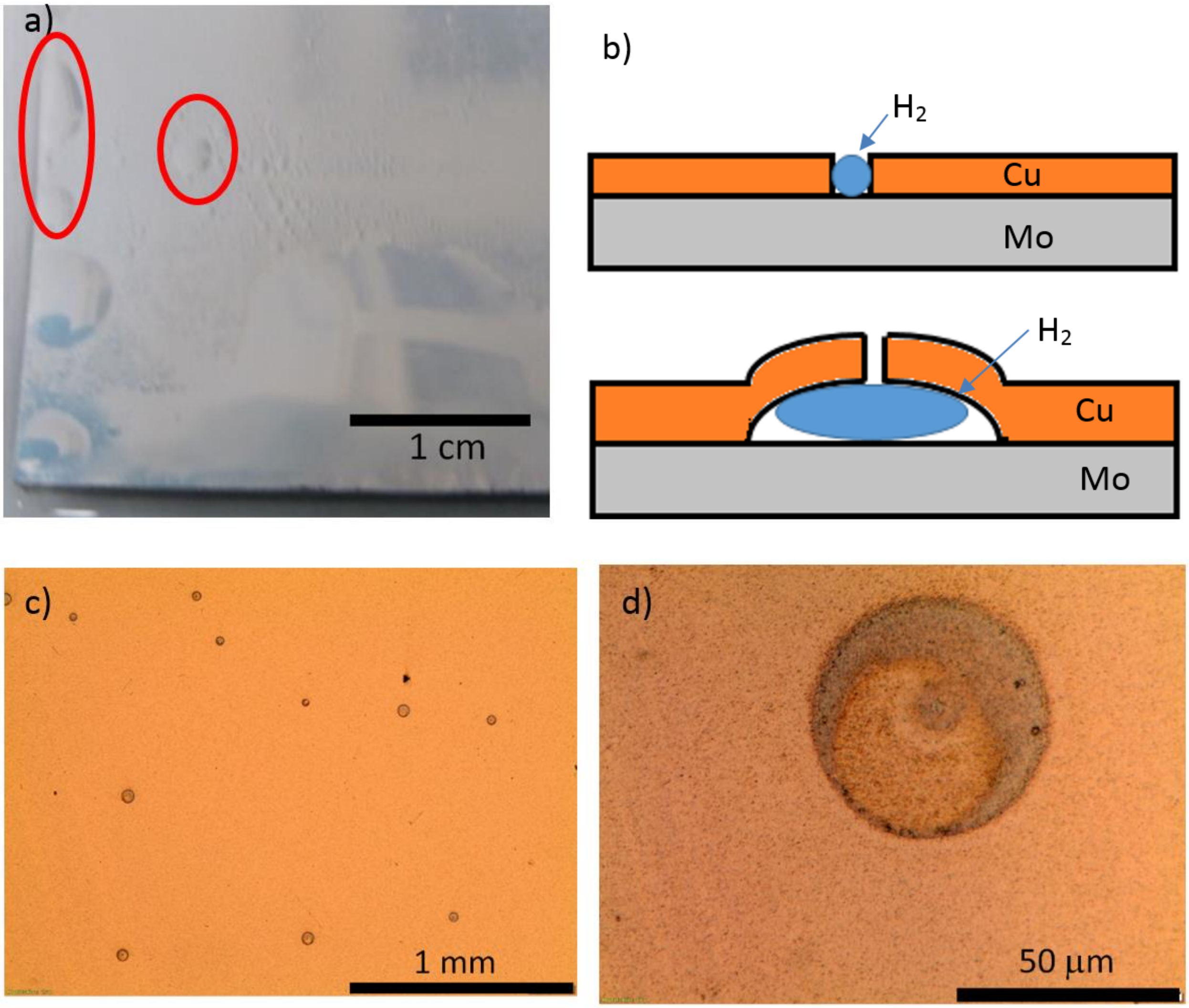

Figure 3.1: (a) Example of Cu/Sn layer deposited on Mo with formation of blisters due to hydrogen (sample grown without stirring or rotation), the red ovals highlight some of the bumps. (b) Proposed mechanism of formation of blisters, (c) and (d) top view optical microscope images of a Cu/Sn/Zn layer as deposited, with blisters.

The formation of these blisters will then have an impact on further steps of the fabrication of the solar cells. After selenization, blisters are still seen in the films, and appear to be very fragile, which then strongly decreases the performance of the solar cells. This will be investigated further in the thesis, in section 5.3.1.

In the following section, the specificities of each layer of the three-stack Cu/Sn/Zn are presented, including the morphology and composition homogeneity at macroscopic and microscopic scales.

3.3 Properties of as electrodeposited layers and stacks

This section will describe thin films formed after electrodeposition of Cu, Sn and Zn onto Mo substrates using the new process presented in section 3.2.1, deposited under standard plating conditions described in chapter 2. The parameters studied are the thicknesses of each metallic layer. The final composition of the Cu/Sn/Zn stack is given by the relative thicknesses of the individual metal layers, and the sum of the three layers informs on the quantity of matter present in the film. Other characteristic parameters are the roughness of the films, their compactness, or the size of metals grains. In this section, only thin films of Cu/Sn/Zn obtained directly after deposition are considered, with no consideration about alloying of metals, which will be described in the next section. Analyses are done at macroscopic scale (centimeter scale, which corresponds to the size of an entire sample), and at microscopic scale (micrometer scale).

3.3.1 Macroscopic scale

Figure 3.2 shows digital photographs of typical surfaces of glass/Mo/Cu, glass/Mo/Cu/Sn and glass/Mo/Cu/Sn/Zn as electrodeposited. All layers are very reflective, which is a sign of smooth surfaces. No macroscopic feature is observable by the naked eye when the depositions are carried out correctly.

Profilometer measurements on electrodeposited layers of Cu, Cu/Sn and Cu/Sn/Zn show roughness averages (R_a) in the order of 10 nm for the Cu layer (5% of Cu thickness), 25 nm for Sn (10% of thickness) and 30-40 nm for Zn (15% of Zn thickness). From these measurements, one can conclude that all layers are rather smooth. This will be discussed further in the next section, where each metallic layer is analysed at the microscopic scale.

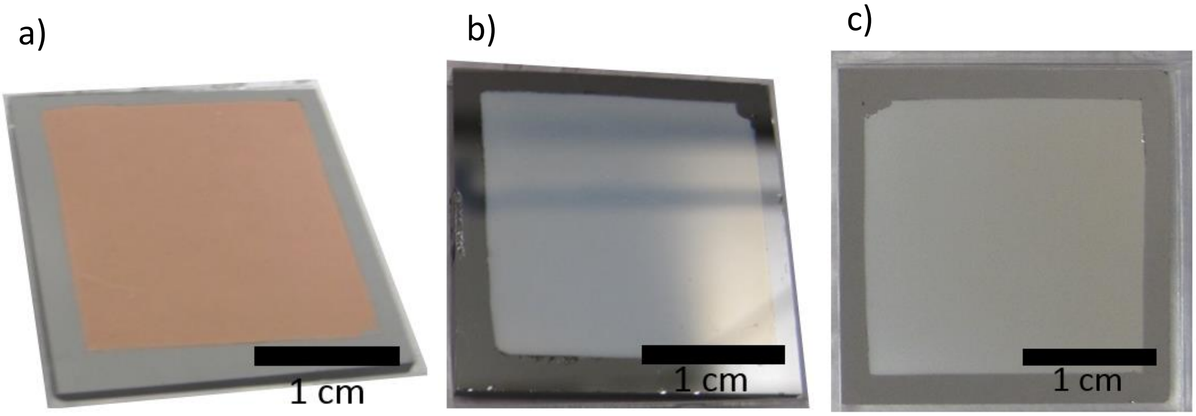

Figure 3.2: Digital photographs of (a) Cu on Mo, (b) Sn on Mo/Cu, and (c) Zn on Mo/Cu/Sn as electrodeposited using the standard methodology described in section 2.1.1.

To assess the homogeneity of thickness and composition of the films over almost the complete sample area, X-ray fluorescence (XRF) measurements were done at the scale of several centimeters on Cu/Sn/Zn samples using a XRF machine calibrated to determine directly the thickness from these measurements. Figure 3.3 shows the thickness variation of the Cu, Sn and Zn layers of a Cu/Sn/Zn sample. Cu and Sn are the most homogeneous layers of the stack, with a standard deviation of thickness of respectively 2 nm and 3 nm, corresponding to coefficients of variation of around 1% for Cu and Sn. The zinc layer is the least homogeneous, with a standard deviation value of 13 nm, which represents around 6% variation of thickness. The distribution of thickness is radially-symmetric (the center of symmetry being the center of the electrodeposited area), and zinc thickness is increasing at the edges of the thin film. The increase of Zn thickness at the edges of the deposition area can be explained by an increase of electric potential (the potential becomes less negative) over the distance from the contacts, due to the resistance of the Mo layer. This results in a faster growth of Zn at the edges of the sample, because of the more negative potential.

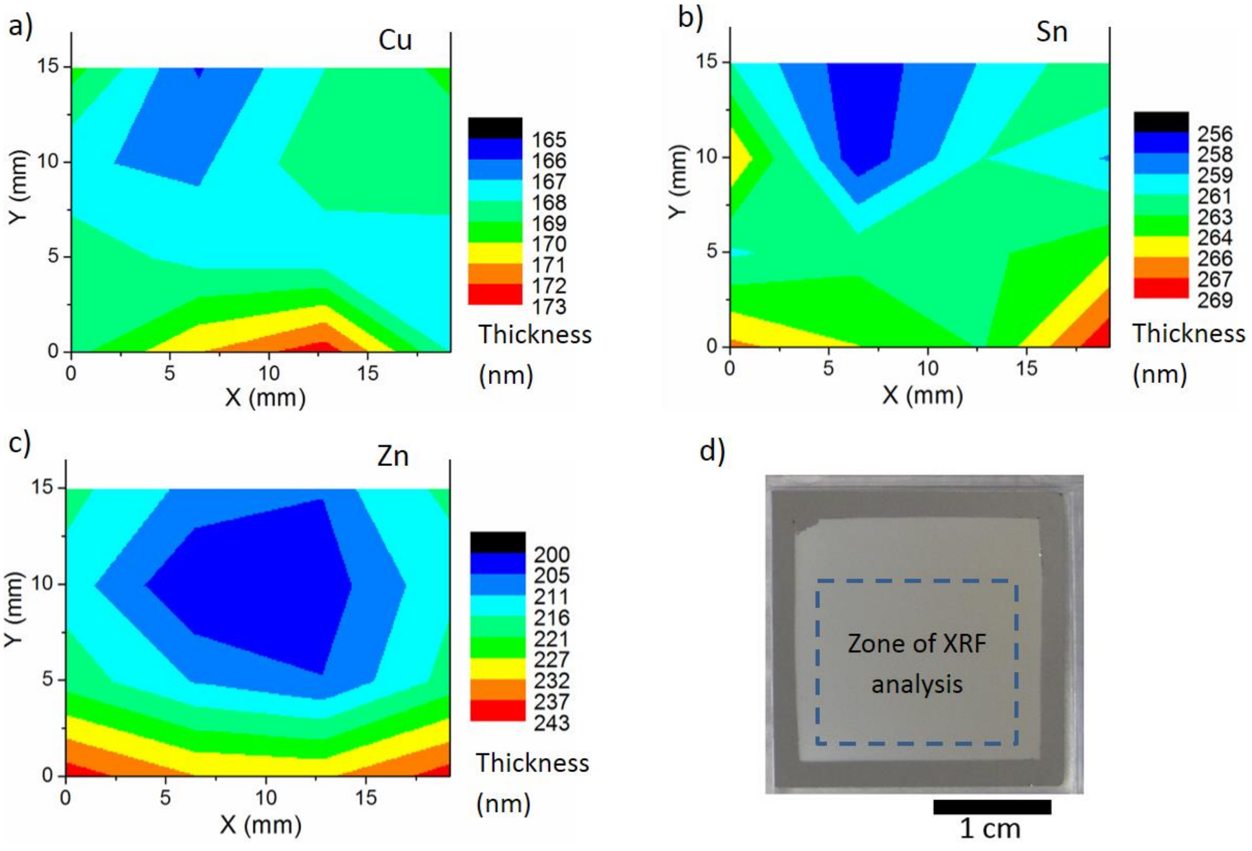

Figure 3.3: Distribution of thickness of (a) Cu, (b) Sn, (c) Zn from XRF measurements at NEXCIS. The film is plated with charges 2.2 C of Cu, 1.4 C of Sn, 2.8 C of Zn. (d) shows the area of the samples (dashed blue line) where the XRF measurements a, b and c were done.

The thickness maps of figure 3.3 were obtained by measuring 16 different points inside the zone of analysis. The deposition being radially-symmetric, a representation of the percentage of zinc thickness increase as a function of the distance to the center can be plot using all these data points. This graph is shown in figure 3.4a. This allows to characterize the Zn thickness increase over the area of the sample, and use it as a reference to estimate the composition of the films at different positions. This was found to be in good agreement with the other samples prepared throughout the thesis work. Figure 3.4b shows an estimated percentage of increase of zinc over the area of a complete sample, from the data of figure 3.4a. This model will be used for the following of the thesis.

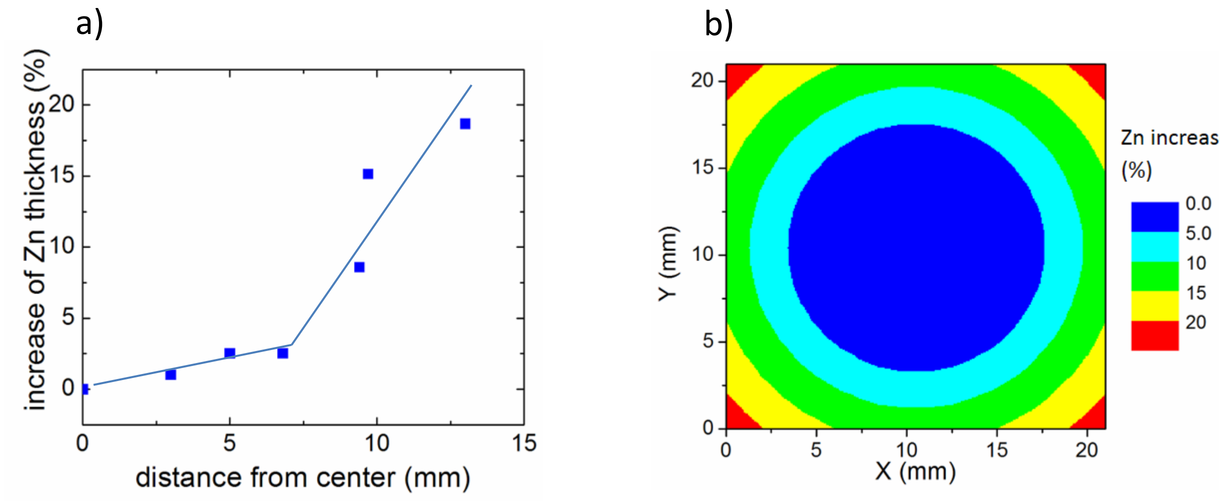

Figure 3.4: Evolution of (a) percentage of increase of thickness of the zinc layer from the center of the sample, as a function of distance to the center of the sample, (b) expected increase of zinc layer thickness (%) on a complete sample.

Several samples with different thicknesses of Cu, Sn and Zn were analyzed with XRF to assess the reproducibility of the process, as well as to calculate the faradaic plating efficiencies for each of the deposition steps. Figure 3.5 shows the evolution of thickness of each layer, compared to the coulombic charge passed during each deposition. The electrodeposition process is robust, as there is a linear relationship between charge and thickness for all deposition processes. Faradic plating efficiencies of 82 %, 96 % and 63 % are calculated for Cu, Sn and Zn respectively. Thus the composition of the film can be easily controlled taking into account these efficiencies by electroplating until a certain charge is passed.

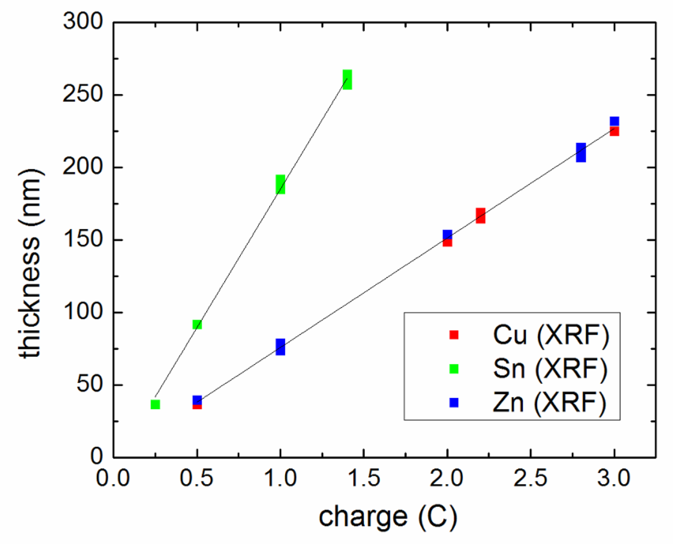

Figure 3.5: Evolution of the thickness of each metallic layer with the charge passed during electrodeposition of the corresponding metal.

In conclusion, the main characteristics of each layer are summarized in table 3.3. Each layer is smooth, and no macroscopic feature is observable optically. The slight increase of roughness average values for tin and then for zinc layers are probably due to the fact that these layers are deposited on surfaces that are already rough (copper is deposited on a flat surface of Mo, whereas zinc is deposited onto a surface of tin which is already rough). Cu and Sn are laterally homogeneous, whilst Zn has a radial thickness variation over the area, with the thickness at the edges being typically 15 to 20% thicker than at the center. A similar problem of thicker zinc deposits at the edge of the samples was reported by Berg [46], in the case of deposition of zinc on a Cu substrate. It was solved in this case by increasing the concentration of zinc in the electrolyte. For the electrodeposition of Zn on Sn studied here, the concentration of zinc is already very close to the solubility limit, thus it was not possible to investigate even higher concentrations to improve the homogeneity of the zinc layer.

Table 3.3: Summary of properties of each layer of a Cu/Sn/Zn electrodeposited stack.

Layer	Plating efficiency (%)	Thickness standard deviation (total area) (%)	Roughness average (nm)
Copper	82	1	10
Tin	96	1	25
Zinc	63	6	30 – 40

3.3.2 Microscopic scale

At the micrometer scale, SEM top view images (figures 3.6a, 3.6b and 3.6c) show dense and relatively smooth layers for all metals. The Cu layer is composed of grains of about 200 nm size, Sn of grains of 200 nm to 1 μm and Zn about 200 nm.

In terms of morphology (grain size, roughness), these layers are very similar to the electrodeposited champion 9.1% Cu/Sn/Zn stack presented by Vauche et al. [41], [57], except for the zinc layer, which in their case seems to be more porous and rougher. A disadvantage of having very compact layers may be a lower tolerance to the lateral compressive stress caused by volume expansion during the selenization process. SEM images show the layers to be laterally homogeneous in morphology. The morphologies can also be compared with reports of Berg [46] who deposited Cu, Sn and Zn layers using the same electrolytes than in this thesis. The morphologies are very similar for Cu and Sn (very similar shape and size off grains). The zinc layer is quite different with much smaller grains. This is probably due to the different stack ordering used by Berg, Cu/Sn/Cu/Zn, where Zn is deposited on Cu instead of tin in the case presented here. Different substrates can infer different nucleation densities for instance, which can be the cause for differences in final grain sizes.

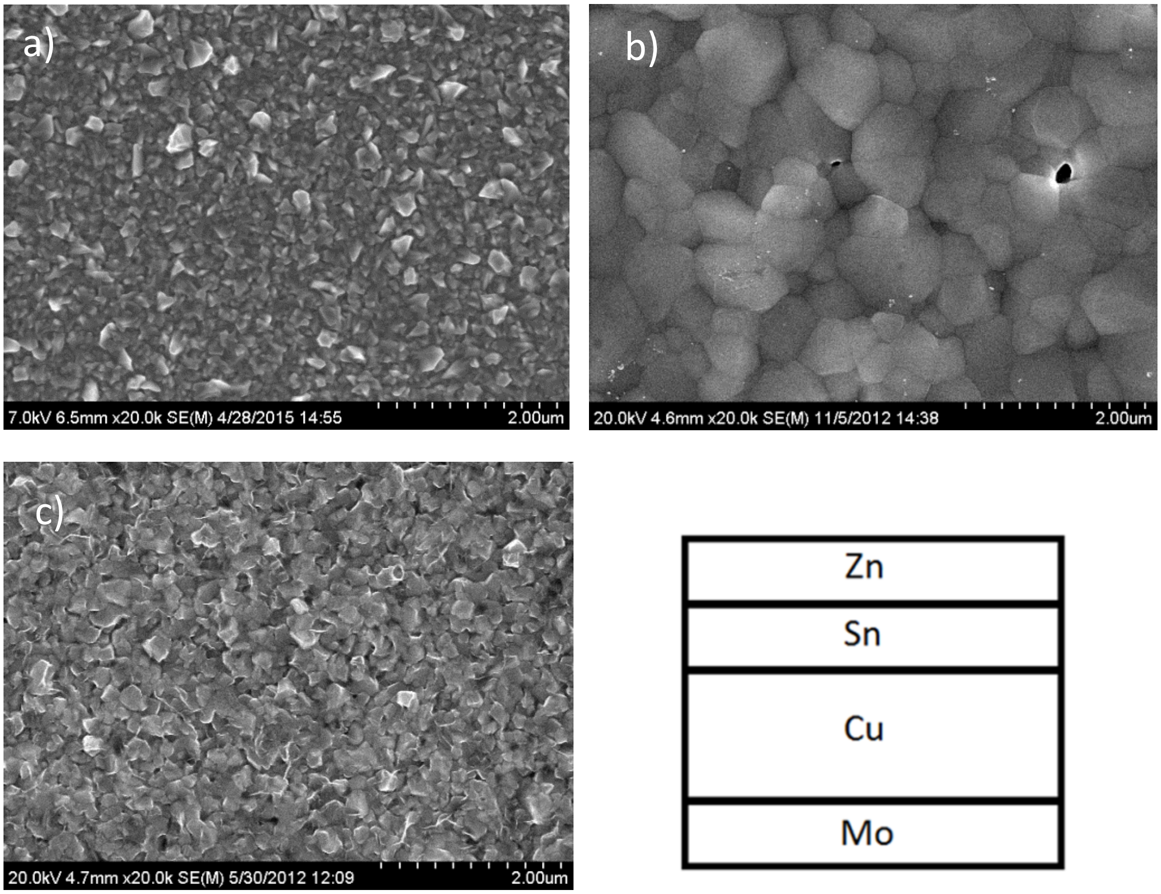

Figure 3.6: SEM top view images of (a) Cu layer on glass/Mo, (b) Sn layer on glass/Mo/Cu, (c) Zn layer on glass/Mo/Cu/Sn, as electro-deposited; (d) schematic representation of an as-deposited Cu/Sn/Zn stack, side view.

To assess the lateral homogeneity of composition at the microscopic scale, an EDX map of a Cu/Sn/Zn sample as deposited was measured on a 65 x 45 μm^2 area. From this EDX map, molar fractions of each metal are calculated and their distribution is displayed as maps, shown in figure 3.7. To be consistent with the representation of compositions on the Kesterite quasi-ternary diagrams, the same molar fractions are used in the case of the EDX maps, as described in section 2.2.2 (equations 2.5, 2.6 and 2.7).

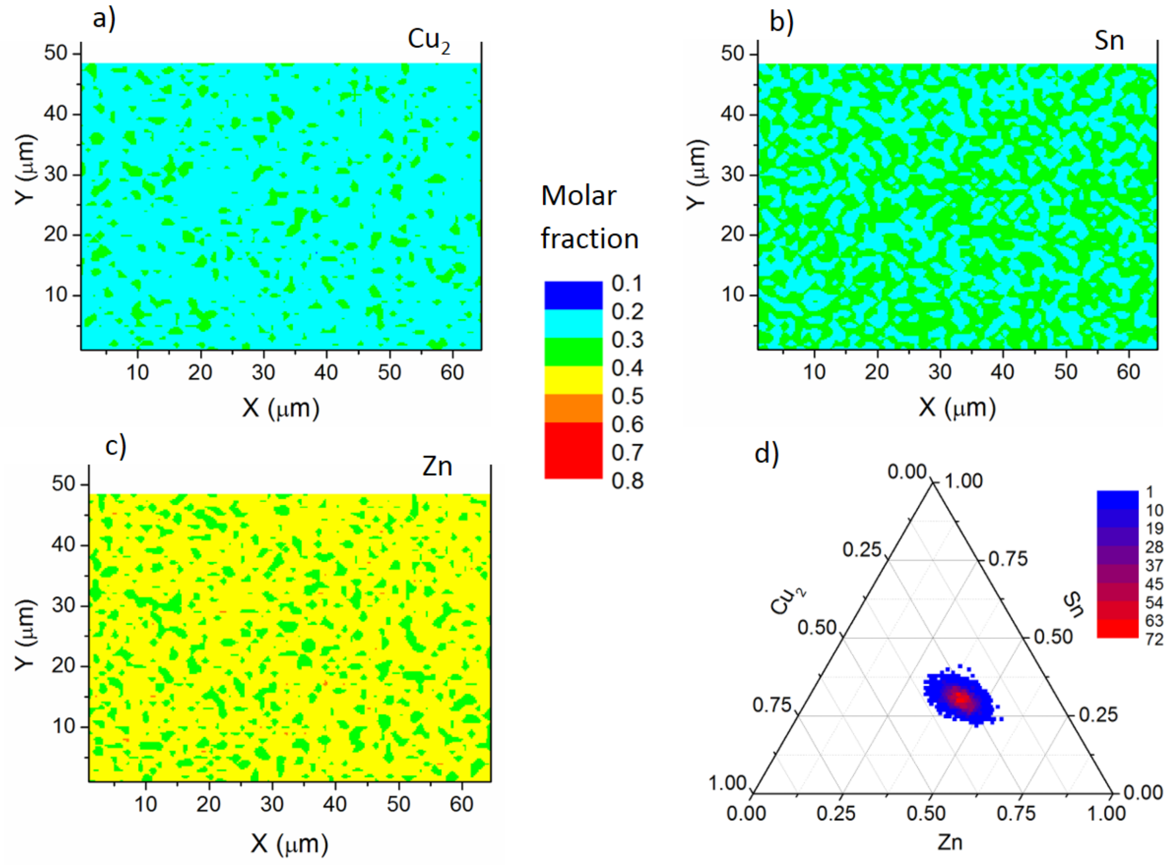

Figure 3.7: EDX mapping of Cu/Sn/Zn sample as deposited: (a), (b) and (c) lateral chemical maps displaying molar fractions of respectively Cu_2, Sn and Zn. The color scale of chemical maps is the same for 3.7a, 3.7b and 3.7c, and will remain consistent for all chemical maps presented in this thesis. (d) compositions of every point of the chemical maps 3.7a, 3.7b and 3.7c, each point of the ternary diagram is color-coded to represent the number of points of the chemical map which have the same composition.

The chemical maps generated from the EDX mapping on the surface of a Cu/Sn/Zn are shown in figure 3.7a, 3.7b and 3.7c. They perhaps reveal a minor segregation of the metals, at a scale of about 1-3 micrometers for all three metals. However, the overview of compositions on the analysed area (figure 3.7d) shows a fairly narrow distribution of compositions, meaning that no strong lateral segregation of metals has occurred at this step of the process at the microscopic scale. No equivalent study at this scale of more than 50 micrometers can be found in the literature.

3.3.3 Summary: electrodeposited stack properties

After the analysis of Cu/Sn/Zn stacks electrodeposited on glass/Mo substrates, four key figures (figure 3.8) and three main properties of these films can be underlined:

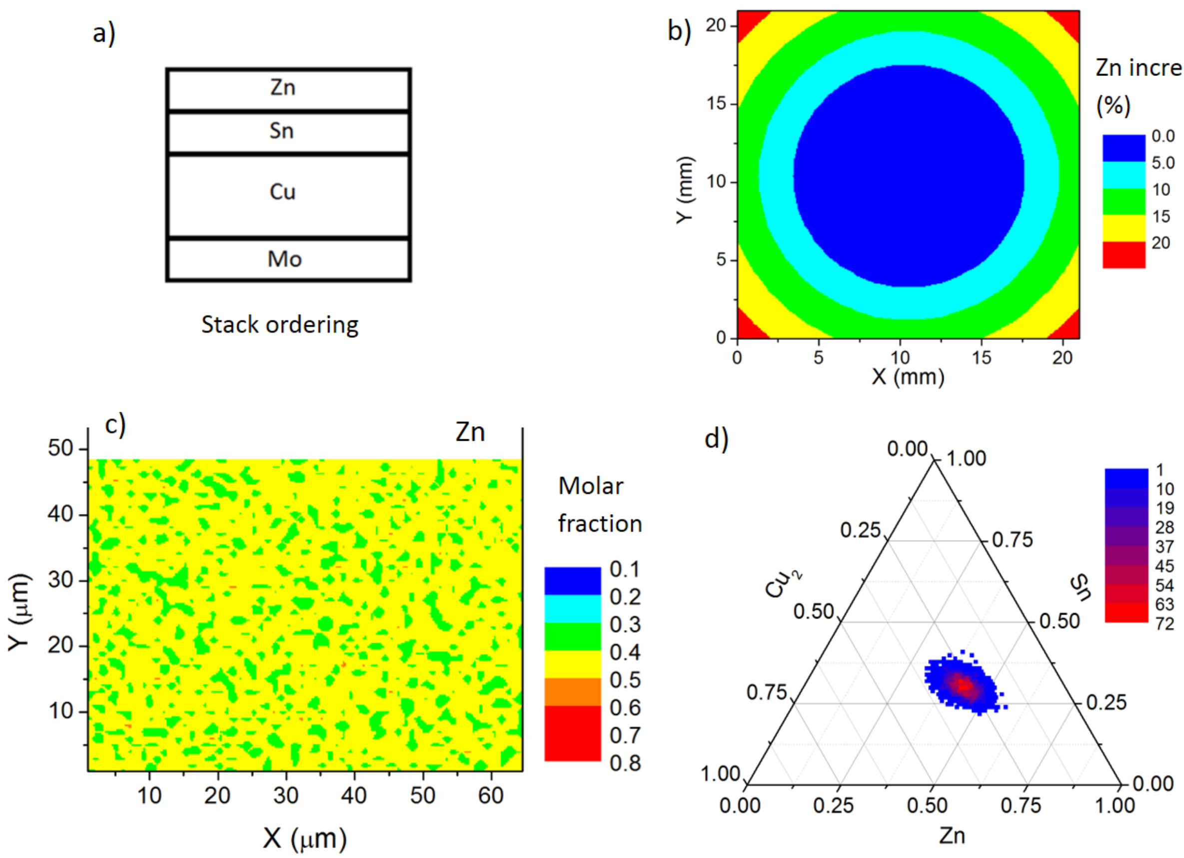

Figure 3.8: Key figures describing as deposited Cu/Sn/Zn samples: (a) cross section schematic, (b) evolution of zinc thickness laterally, (c) lateral chemical maps displaying molar fractions of Zn. (d) compositions of every point of the chemical map 3.8c, each composition being color-coded to represent the number of points which have the same composition.

A few key characteristics can be listed:

i) For all layers, the morphology is dense and the surface is flat and smooth.

ii) The composition at microscopic scale is fairly homogeneous (figure 3.8c and 3.8d), compared to distributions of elements at microscopic scale after alloying (the distribution of elements after alloying will be described in section 3.4), or after selenization (in section 4.4).

iii) The composition at microscopic scale is homogeneous over the total sample area (2.1x2.1 cm^2), except for an increase of zinc molar fraction at the edges, due to an increased thickness of zinc towards the edges of the deposit (figure 3.8b). A homogeneous zone can be used on the center of the sample, of about 1x1 cm^2, where the thickness standard deviation of Zn is comparable to that of Cu and Sn.

iv) There is a strong in-depth inhomogeneity, due to the architecture of the layers prepared, as stacks Cu/Sn/Zn (figure 3.8a).

3.4 Alloying of Cu/Sn/Zn stacks

3.4.1 Introduction

This section presents results on the alloying of precursor layers at 350°C. the first objective is to study the effects of alloying at the scale of the sample, and especially investigate the effect of the composition change over the surface, induced by the gradient of composition of zinc (increase of zinc content towards the edges of the deposited films). The second objective is to study the samples surface at a scale of 65 x 45μm^2, which was not yet done in the literature, with the objective to investigate the size of the segregation of metals in the layers after alloying. This study involves the use of mapping tools to understand in detail the lateral repartition of the metals. Focused ion beam (FIB) cross section images are also presented, to investigate the in-depth distribution of phases.

3.4.2 Description of alloyed sample at macroscopic scale

The standard alloying process which was used for this work was performed at 350°C for 30 min, in a RTP oven, which allows fast heating and cooling ramps (see chapter 2). A first analysis of a sample after alloying was done to investigate the in-depth distribution of metals (figure 3.9). It appears that the three metals are uniformly distributed in-depth, thus the structure is probably not a bilayer of Cu-Zn and Cu-Sn, and is rather columnar as described by Ahmed [40]. An increase of Zn signal is seen at the surface of the layer, which indicates the presence of a Zn-rich layer at the surface, probably ZnO.

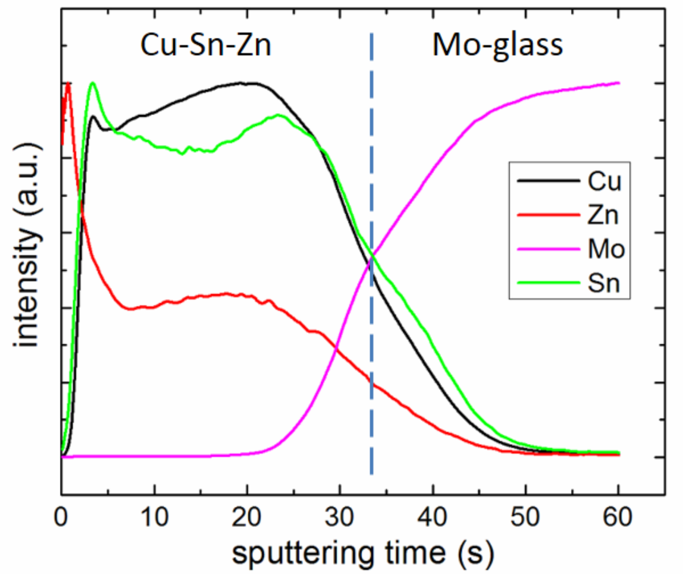

Figure 3.9: Glow discharge optical emission spectroscopy (GDOES) in-depth analysis of a Cu/Sn/Zn sample after alloying at 350°C for 30 min. Each element is normalized at its maximum value. The blue dashed bar indicates the probable limit between the layer and the Mo back contact.

Figure 3.10a shows a photograph of a sample after this process. A change of color is observed: the silver grey color of the zinc top surface is replaced by a brown color after alloying, due to the formation of alloys of Cu-Sn and Cu-Zn, and perhaps also because of the formation of an oxide layer on the surface of the thin film.

Another interesting feature which is observable on the picture of the alloyed sample (figure 3.10a) is the formation of a nearly-circular pattern of around 1.6 cm diameter, whose center corresponds to the center of the deposited area. This circular feature is not optically present in the as electrodeposited precursor, but is observed for all alloyed samples samples. This pattern was analysed, with the help of a profilometer and EDX to understand what it is, as well as what is its origin. For this, the sample presented in figure 3.10a was marked at different positions, as shown in figure 3.10b, to determine precise areas where EDX analyses are performed.

Figures 3.10c shows the evolution of the ratio Sn/(Cu+Sn+Zn) at the different positions of interest. The values far from the circle are nearly identical (positions 1 and 4), however close to the circle a strong increase of tin is observed on position 2, and a strong decrease at position 3, which corresponds to the circle. It can thus be speculated that the optical feature observed as a circle is a zone of the sample from which tin has migrated towards the center of the sample.

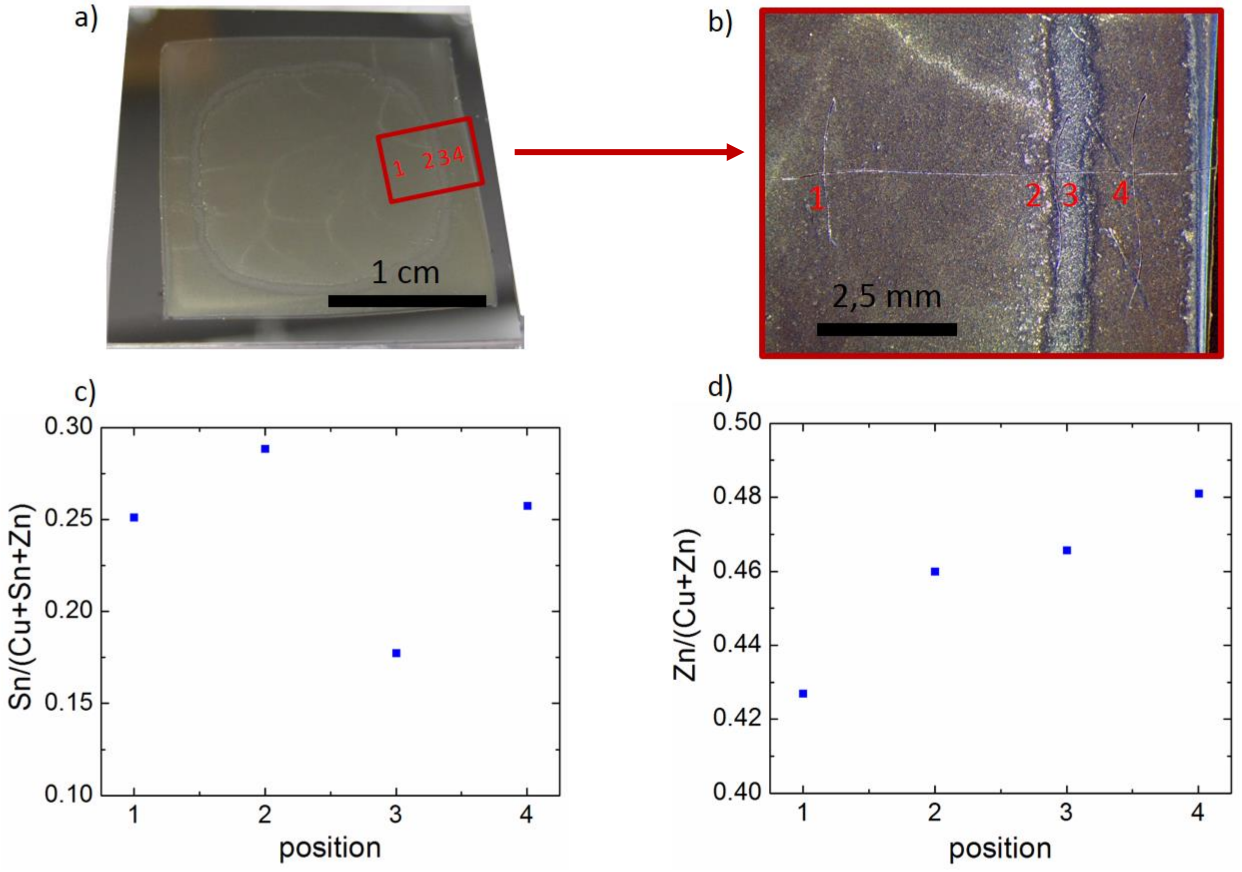

Figure 3.10: (a) Digital photograph of a Cu/Sn/Zn stack after alloying at 350°C for 30 min; (b) enlargement of image 3.10a (red square), the red numbers mark the positions of the EDX analyses, in the vicinity of the circular pattern. (c) and (d) evolution of ratios Sn/(Cu+Sn+Zn) and Zn/(Cu+Zn) as a function of position in the vicinity of circular pattern.

If the zinc ratio is calculated by excluding tin, as Zn/(Zn+Cu) shown in figure 3.10d, the evolution of this ratio is as expected, increasing due to the increased quantity of zinc towards the edge of the sample (due to the electrodeposition, explained in 3.3.1), which strengthens the idea that Cu and Zn did not migrate, and only tin migration is responsible for the change of Sn/(Cu+Sn+Zn) ratio. Furthermore, tin being the only liquid species at the alloying temperature, it is the most likely to diffuse over a large distance of more than 600 microns.

To help understand the driving force of this phenomenon, chemical alloying reactions occurring during the annealing have to be considered (reactions 3.2 and 3.3).

$\mathrm{Cu+Zn} \rightarrow \mathrm{CuZn}$ $\Delta G = -8$ to -12 $\mathrm{kJmol^{-1}}$ at 300 K (3.2)

$\mathrm{6Cu+5Sn} \rightarrow \mathrm{Cu_6Sn_5}$ $\Delta G = -7$ $\mathrm{kJmol^{-1}}$ at 473 K (3.3)

Assuming a linear relationship between Gibbs free energy of reaction and reaction rates, because of the higher Gibbs formation energy of CuZn compared to Cu_6Sn_5, Cu alloys preferentially with Zn. Thus, as a first approximation, the reaction of formation of Cu-Zn alloys can be considered first, and tin reacting afterwards. Figure 3.10d shows that from point 1 to point 4, there is a linear increase of Zn/(Cu+Zn) ratio from values of 0.43 to 0.49, which is in agreement with the model of section 3.3.1 (figure 3.4b).

Figure 3.11a shows that at 350°C, in the range of Zn/(Cu+Zn)= 0.42 to 0.5, two different systems are present: below Zn/(Cu+Zn)=0.47, a phase of β' CuZn is present together with a phase α, constituted mostly of Cu. Above Zn/(Cu+Zn)=0.47, only a phase pure of β' CuZn is present. This is shown in figure 3.11b, to compare this observation with the data of Zn/(Cu+Zn) at different positions close to the circular pattern of the prealloyed sample.

Figure 3.11b shows clearly that the position of the circle (position 3) corresponds to a change from a 2-phase Cu-Zn system to a single phase system. In this single phase system, all Cu is alloyed with Zn, thus Sn migration is favored towards the inside of the sample, where the α Cu phase is present, with which Sn can alloy. Thus, this decrease of free copper could be the driving force for the migration of tin. As said before, non-alloyed tin is liquid at the temperature of the alloying, which can explain the ease for this metal to migrate over a relatively long distance.

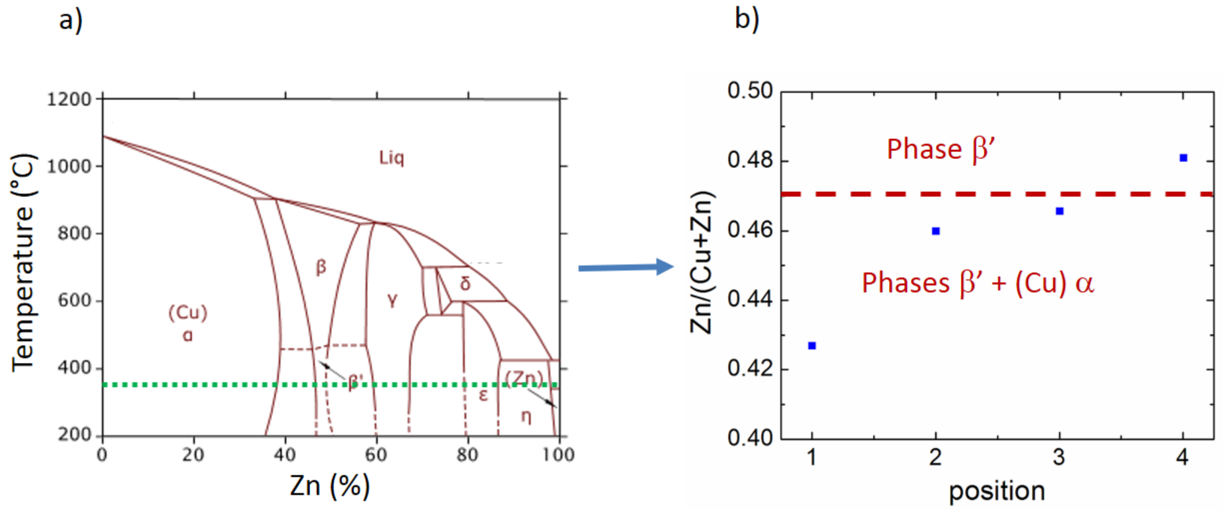

Figure 3.11: (a) Phase diagram of Cu-Zn reproduced from [68]**, the green dotted line indicates the temperature of 350°C, (b) evolution of ratio Zn/(Cu+Zn) as a function of position in the vicinity of circular pattern (figure identical to 3.10d), with indication of corresponding alloy phases at 350°C and dotted red line indicating phase transition, from phase diagram of figure 3.11a. β' is the phase CuZn.**

3.4.3 Microscopic analysis after alloying

This section describes all changes that occurred in the thin film of Cu-Sn-Zn after alloying. The results presented in this section are all obtained by studying a single sample, at a specific position, unless stated otherwise. The sample is referred to as “reference sample”, and the specific position as “position of interest”. In the following chapter, this reference sample will be analysed at the same position after selenization, using the identical location microscopy method, which was adapted for the needs of this thesis (see chapter 2, identical location analysis). In case of the analysis of a different sample, the term “sister sample” refers to a sample which was grown under the exact same conditions as the reference sample.

Microscopic scale analysis was performed on the reference sample on the area of interest. Figure 3.12 compares the top view SEM images of a sample before alloying (figure 3.12a), and after annealing at 350°C for 30min (figure 3.12b). A clear change is observable: the image of the as electrodeposited sample is uniform over the total area, whereas the annealed sample has regions with different brightness. Two distinct regions are clearly observed: 10-20 μm sized dark islands (region 1) surrounded by a speckled brighter area (region 2). It is also interesting to note that these same different regions are observable with an optical microscope, by comparing figures 3.12b and 3.12c.

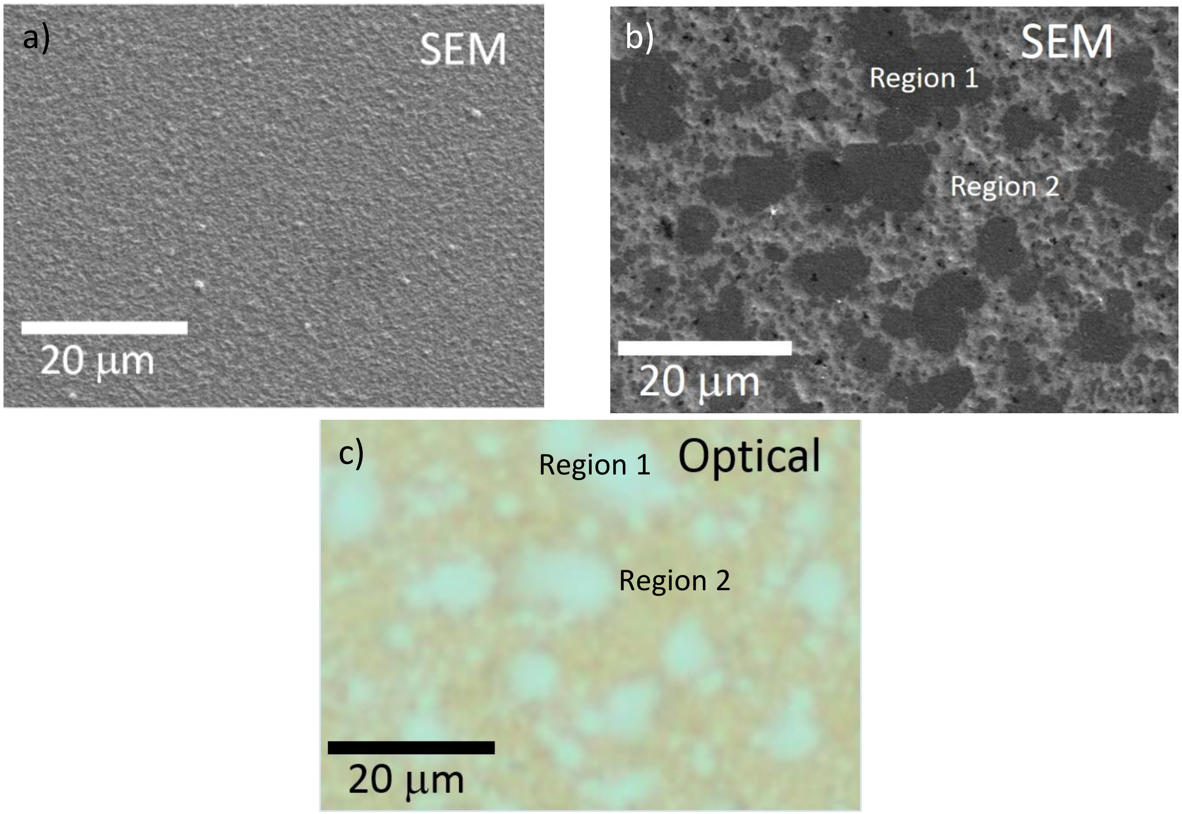

Figure 3.12: SEM top view image of (a) as deposited sister sample, and (b) annealed sample (reference sample). (c) optical microscope image of the reference sample, at the identical position.

To analyse the structure of an annealed sample in-depth, a sister sample grown under the same conditions as the reference sample was used to perform a focused ion beam microscope analysis of a cross section. The images are presented in figures 3.13a and 3.13b. The similarity of the surface in figure 3.13a to that of figure 3.12b should be noted. Figure 3.13b is a zoom showing where the cross sectional image was taken. Figure 3.13c shows an image of the cross section. Region 1 appears single phase and compositionally homogeneous in-depth, i.e. this region is called phase 1, whereas region 2 seems constituted of a second phase (phase 2) along with grains of phase 1.

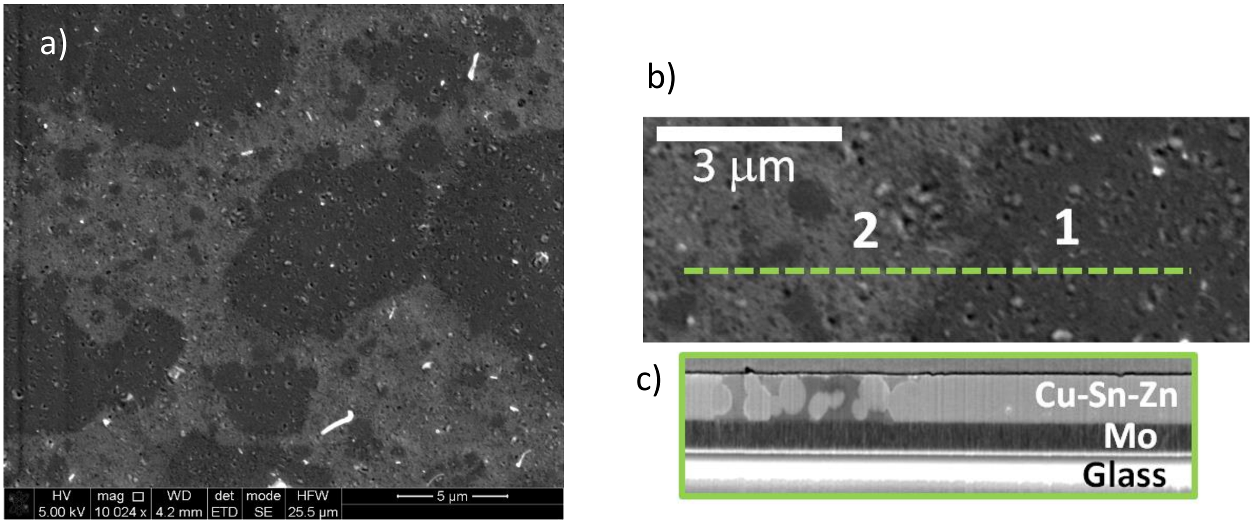

Figure 3.13: (a) Top view SEM image of an annealed sister sample, (b) zoom of top view SEM image 3.13a showing where the cross section was cut, (c) the SEM cross section image.

Grazing incidence XRD measurements of the reference sample show the presence of Cu_5Zn_8 and Sn phases (figure 3.14). The additional presence of CuZn and Cu_6Sn_5 is possible, but not certain due to the combination of overlapping peaks with other phases and the absence of unique peak for these alloys in the diffractogram. From the Cu-Sn-Zn phase diagram of Huang et al [63], these four alloys can be expected. A more detailed composition analysis will follow (chemical mapping of the surface of interest, figure 3.15).

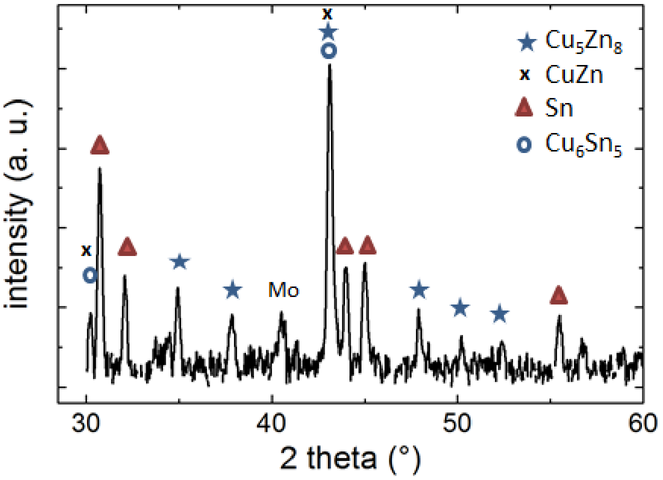

Figure 3.14: XRD patterns of reference sample after prealloying at 350°C for 30 min.

To identify the composition of the two regions, an EDX map of the area of interest was measured. From this EDX map, molar fractions of each metal are calculated and their distribution is displayed as maps. Figure 3.15 compares the SEM top view image of this area with the chemical maps of the same area displaying molar fractions of Zn, Sn and Cu. The reader is here reminded that the molar fractions displayed on the chemical maps are defined identically to the molar fractions shown on ternary diagrams (considering the ternary system Cu_2 – Sn – Zn), for easier comparison between figures.

To aid the comparison between the image and the maps of figure 3.15, a contour line is displayed on each figure, corresponding to a molar fraction of Sn=0.25. After comparison of the three chemical maps shown on this figure, several points can be noted:

(i) The tin map shows the highest compositional variation (molar fraction ranging from 0.1 to 0.6), among the three maps (zinc between molar fractions of 0.3 and 0.6, Cu between 0.1 and 0.4). There is a clear correlation between region 1 of the SEM picture figure 3.15a) and tin-poor areas of the chemical map.

(ii) There is a compositional anti-correlation between the tin and the zinc, as well as between tin and copper. Zinc and copper dominate region 1, but there is still a significant amount of these metals in region 2.

From these observations, region 1 can be assigned to a Cu-Zn phase, and region 2 to phases containing Cu-Sn-Zn. Knowing that a ternary Cu-Sn-Zn phase does not exist under the conditions that are investigated, it can be assumed that region 2 contains two binary metal alloys, Cu-Sn and Cu-Zn. This is in accordance with the observations made with FIB cross section analysis of alloyed sample (figure 3.13), where it was concluded that region 1 contains a single phase (Cu-Zn), while region 2 contains 2 phases: inclusions of this same phase of region 1 (Cu-Zn), in another phase (Cu-Sn).

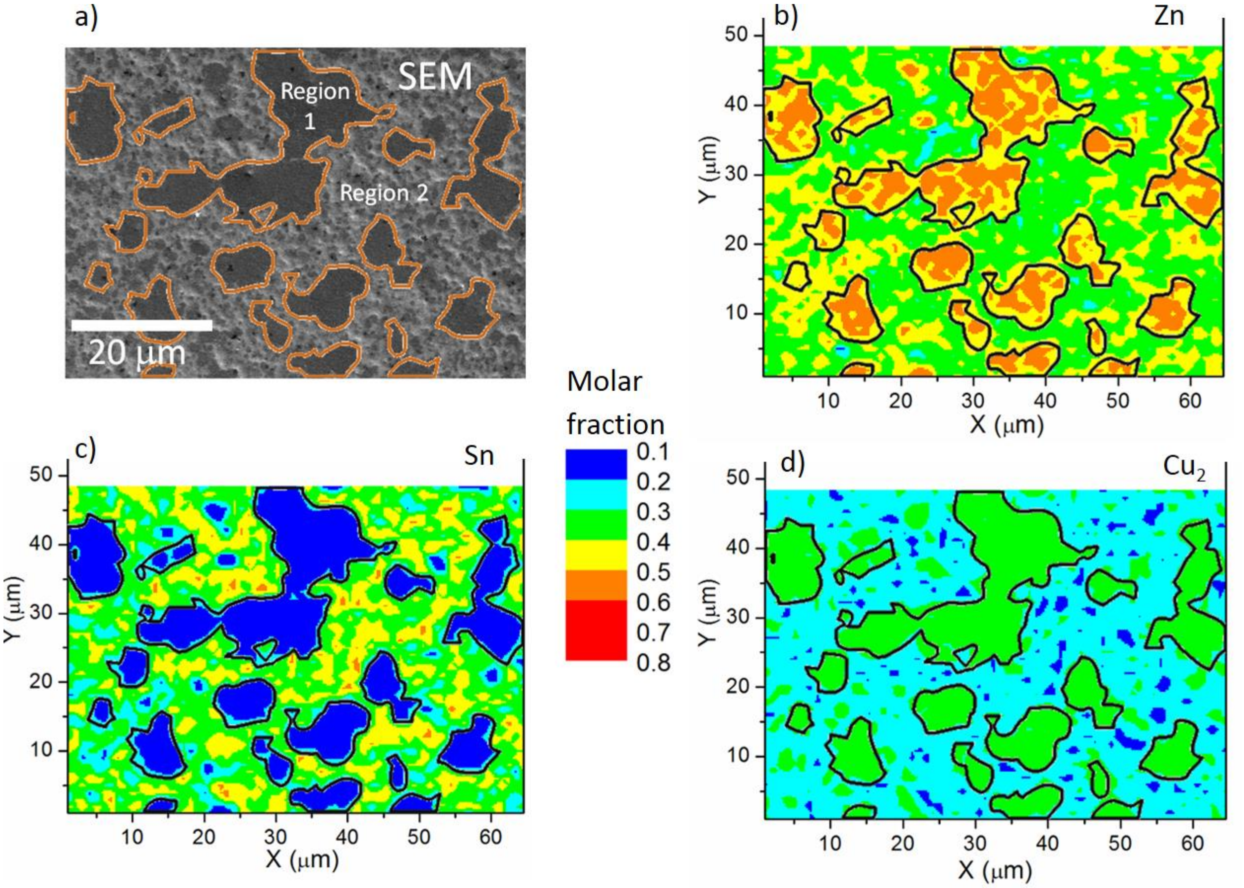

Figure 3.15: (a) SEM top view image of the reference sample after annealing at 350°C (repeated from figure 3.12 for convenience) and molar fraction maps of (b) Zn, (c) Sn and (d) Cu. The color scale of the chemical maps is the same for 3.15b, 3.15c and 3.15d. Contour lines (orange in figure 3.15a, black for others) are the same for the four figures, and are defined by a molar fraction of Sn=0.25 (see figure 3.15c).

To investigate further the composition of the area of interest, figure 3.16a provides an overview of all compositions of the area on the common Cu_2-Zn-Sn ternary. The green oval delimiting the as electrodeposited composition is much smaller compared to the composition spread after alloying, which confirms that a strong lateral inhomogeneity in composition was generated during this step. A clear bimodal distribution of composition is revealed, with a narrow tin-poor area, and a broader area more tin-rich. It is interesting to note that there is a near-invariance of ratio Cu/Zn, in other terms the changes of composition observed are mainly dominated by a change of tin molar fraction.

Sn-poor compositions, which are attributed to region 1 of the area of interest (figure 3.15), are centered on (0.34 Cu_2, 0.15 Sn). Considering the phase diagram of Huang et al. [63] (figure 3.16b), it corresponds mostly to phase β’CuZn(5% Sn).

The more Sn-rich compositions (that were attributed to region 2 of the area of interest) range from 0.25 Sn to 0.5 Sn. The broader dispersion of composition is due to the coexistence of CuZn and CuSn alloys, as was described previously. Figure 3.16b shows that these compositions are mainly in a three phase field lying mostly along the β'CuZn(5%Sn) and Sn (+2% Zn and 2% Cu) tie line with a minority composition of Cu_6Sn_5 [63]. A larger solubility of the tin and the zinc is expected because here the alloying step is carried out at 350°C. Metallic Sn was clearly detected by XRD in accordance to the phase diagram.

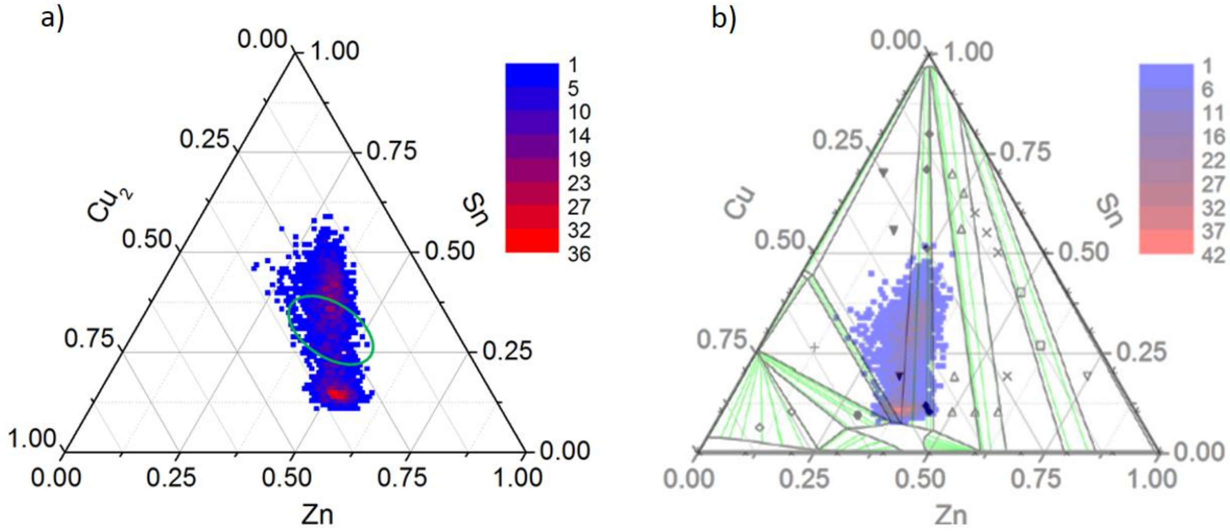

Figure 3.16: (a) Compositions of every point of the chemical maps of figure 3.15, each composition being color-coded to represent the number of points which have the same composition. The green oval shows the limit of spread of compositions of the map of the as-deposited sample (figure 3.7d). (b) superposition of the data from figure 1.16a onto 250°C ternary phase diagram from Huang et al. [63]**. The reader's attention is drawn to the fact that the 3.16b ternary diagram has Cu-Sn-Zn as axes, and not Cu_2-Sn-Zn, to match the ternary coordinates of Huang et al.**

In terms of phase composition, these results are consistent with what was known previously [44]. Concerning the size of the metals segregation after alloying, the results are very different to what was previously reported. In the same case of a tri-layer Cu/Sn/Zn precursor, Arasimowicz [42] reported the formation of a columnar structure of Cu-Zn and Cu-Sn alloys. This is similar to the case shown here, except for the size of the Cu-Zn alloys. Our analysis method at a larger scale allows the observation of segregated alloys of a size of 10-20 microns, which is one order of magnitude larger than previously reported. It seems clear that chemical segregation of zinc and tin to such a large scale will influence the Kesterite growth. Formation of large sizes of alloys results from a successive coarsening of the phases, which is due to the tendency of the system to decrease the interfacial area between the different phases. It is described in metallurgy [69] or in emulsions where it is referred to as "Ostwald ripening" [70]. In order to form the maximum Kesterite phase during the selenization step, diffusion of tin and zinc will therefore have to occur at this length scale, otherwise formation of ZnSe and Cu_2SnSe_3 is expected respectively on the Sn-poor and Sn-rich areas.

3.5 Summary: electrodeposition and metals alloying.

The electrodeposition process of Cu/Sn/Zn stacks has been proved to be robust, and the layers formed are smooth and dense. The thicknesses are uniform over the entire deposition area, except for the zinc layer for which there is a 15-20% thickness increase at the edges. However, the samples have a homogeneous zone of 1.2 x 1.2 cm^2 in the center. Partial delamination is some times detected, forming blisters of 10-20 micrometers diameter in the layers, because of the formation of hydrogen between the Mo substrate and the copper layer during the electrodeposition.

The study of alloying process showed that at macroscopic scale, the increase of zinc content at the edges induces local diffusion of tin at the scale of a few hundred micrometers, which is thought to be due to a lack of pure copper in zones where zinc thickness is increasing. At microscopic scale, the formation of Cu-Sn and Cu-Zn alloys, and their segregation at large scales of 10 – 20 micrometers are observed. This was never reported in the literature, and this observation was made possible by analyzing samples at a larger scale than previously reported. It can be anticipated that using a precursor with such a metal segregation will have an effect on the subsequent selenization step: if Zn and Sn cannot diffuse at these scales, the segregation will remain, which will induce a segregation of secondary phases. This will be investigated in the following chapter.

4 Selenization of Cu-Sn-Zn thin films

Aim of the chapter

The objective of this chapter is to investigate the mechanism of formation of kesterite and its secondary phases during the selenization of metallic precursors. Knowing that the domain of existence of single phase kesterite is very narrow [71], it is crucial to understand the formation route of the secondary phases and the origin of their segregation, since these compounds are harmful for the efficiency of the solar cells [37]. Knowing the reaction mechanism should allow to tune the process in order to select the type of phases present, their quantity and ultimately their position in the films in order to have the least harmful phase(s) remaining, or to have it (them) in a place where it (they) can be removed.

4.1 Introduction

4.1.1 Background

The mechanism of formation of Kesterite and secondary Kesterite phases has already been studied by several groups, in the selenide Kesterite system as well as in the sulfide case, which is often comparable. However, no clear mechanism of formation is established for the moment. This is mainly due to the fact that many different fabrication processes are investigated, where the precursors are different: mixed metals and chalcogen precursor layers were investigated [72], as well as metals-only precursors [42] which are investigated in this thesis. The metallic precursors can be stacks of metal layers, with different stacking orders, or can be alloys of Cu-Sn and Cu-Zn with many different possible microstructures, such that a strict comparison between reaction mechanisms of different processes is difficult. Selenization or sulfurization processes can also strongly differ from a study to the other: type of oven, sealed/non-sealed annealing chamber, among others are as many parameters which can strongly influence the reaction pathway. However, similarities between all studies can be observed, which will be compared with the results that were obtained for the thesis.

Several mechanisms of reaction have been proposed by Hergert et al. [73] for the formation of Kesterite: either the simultaneous reaction of binary chalcogenides (reaction 4.1), or a sequential reaction, with Cu_2SnSe_3 as an intermediate product (successively reactions 4.2 and 4.3):

$$Cu_2Se + SnSe_2 + ZnSe \rightleftharpoons Cu_2ZnSnSe_4 \quad (4.1)$$

$$Cu_2Se + SnSe_2 \rightleftharpoons Cu_2SnSe_3 \quad (4.2)$$

$$Cu_2SnSe_3 + ZnSe \rightleftharpoons Cu_2ZnSnSe_4 \quad (4.3)$$

However, these binary and ternary selenide phases are not formed simultaneously, due to their different stabilities, and the different kinetics of reaction of each species. Thermodynamically speaking, the standard Gibbs free energy of formation of a compound represents the gain of energy obtained during the reaction of formation, starting from elemental reactants. Thus the more negative the free energy of formation of a compound is, the more it is stable. Values of standard Gibbs free energies of formation of the binary selenides are: ZnSe (-310 kJ/mol) < Cu_2Se (-200 kJ/mol) < SnSe (-170 kJ/mol) < $SnSe_2$ (-105 kJ/mol) < $CuSe_2$ (-25 kJ/mol) [42]. ZnSe is thus the most stable phase, compared to Cu-Se or Sn-Se phases. However, most of the studies of the mechanism of formation of selenides agree on the fact that Cu-Se species are formed first in the selenide system at temperatures around 250-350°C [42], [74]–[78]. The reaction pathway is thus mainly governed by kinetic factors. After formation of binary selenides, Kesterite is starting to form in the films at temperatures around 320-370°C [74], [75], [78]. Furthermore, in several cases where the precursor sample has a Cu-poor and Zn-rich composition (target composition for the solar cells to achieve the best power conversion efficiencies), it was reported that at the surface only ZnSe remains, and no SnSe is detected [42], [74]. However, no study of the reason for the absence of Snse is provided in the literature. This will be investigated in this chapter.

Concerning the segregation of secondary phases, the microstructure of the metallic samples before the selenization seems to strongly influence the position of the phases. Arasimowicz et al. investigated a very similar process to that presented in this thesis, and demonstrated that selenizing a sample composed of a bi-layer Mo/Cu-Sn/Cu-Zn leads to the formation of ZnSe on the whole surface of the absorber, whereas using a precursor with a succession of columns of Cu-Sn and Cu-Zn leads to the formation of only small islands of ZnSe on the surface of the Kesterite layers. This will as well be investigated further in this chapter in order to elucidate the reason of this behavior.

4.1.2 Structure and objectives of the chapter

One main objective is to understand why mainly ZnSe and Kesterite are remaining at the end of the selenization process. Considering the copper poor and zinc rich ($Cu/(Zn+Sn)<1$ and $Zn/Sn>1$) precursor compositions, SnSe is also expected, but Arasimowicz [42] shows that mainly ZnSe is present by using a very similar synthesis process to the one investigated for this thesis. No explanation of this phenomenon is provided in the literature, but a similar phenomenon was observed by Johnson et al. in the sulfide case. In a recent publication, they report the observation of a self-regulation mechanism of Cu/Sn ratio in the synthesis of Cu_2ZnSnS_4 films [43]: in the presence of SnS (g) phase during the selenization, the evaporation of SnS from the sample (in case of tin excess), or the incorporation of SnS from the gas phase in case of lack of tin in the sample self-regulates the Cu/Sn ratio. Thus a hypothesis is that the same occurs in the selenide system, which will be investigated in this chapter. For this, the first objective is to clearly establish the reaction mechanism, and to follow the composition of the films during each step of the selenization. Then different compositions of precursors will be investigated to study this tin self-regulation mechanism more globally.

As described in 4.1.1, many studies on reaction mechanism were already reported by other groups, but most of them investigate it by performing annealings at different temperatures, to see which species are formed first. However, here the objective is to study the kinetics of reaction by deconstructing the mechanism into simple sequential steps. Thus the selenization process will be stopped after different times to analyze the phases present, their position and the composition of the films. This approach was already investigated by Berg [46] in the sulfur case, however it appears that at temperatures higher than 500°C the reaction is too fast and the material is already fully converted to Kesterite even at very short times <1 min.

In order to tackle this problem of the reaction being too fast to allow the observation of its sequential steps, a second study of the mechanism was performed, with a lower temperature (400°C) in order to decrease the reaction rates and have the possibility to observe the reactions occurring during the selenization. The results will be compared with a similar study by Arasimowicz [42], who also investigated the reaction mechanism at different selenization times. The method reported in that case is different and consisted to increase the background pressure of gas in order to lower significantly the diffusion of selenium during the selenization, and thus decrease its activity. The type of annealing chamber is also different in the case of Arasimowicz, since it is not tightly closed and allows a significant quantity of selenium to leave the reaction chamber and thus differs more from the standard selenization processes investigated in this thesis.

Then a study of the evolution of composition after a standard selenization process (550°C for 30 minutes) is done, in order to show evidence of the tin self-regulation mechanism and understand for which compositions it occurs.

The second main objective of this chapter is to investigate the segregation of ZnSe on the surface of the absorbers, and especially the influence of the presence of a large segregation of metals in the precursors before incorporation of selenium. It is very probable that during a standard selenization process, the metals will alloy before the incorporation of selenium in the film. Figure 4.1 shows the evolution of the temperature and of the vapor pressure of selenium as a function of the time of annealing during the selenization process. During the heating ramp, the vapor pressure of selenium is too low thus the layers are only subjected to heating, before the incorporation of selenium.

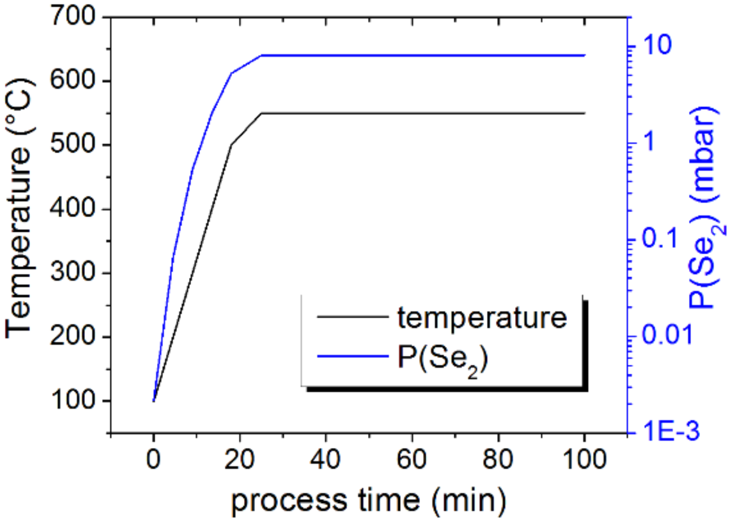

Figure 4.1: Evolution of the temperature and vapor pressure of selenium during a selenization process at 550°C (only the heating part from 100°C to 550°C and an arbitrary dwelling time at 550°C are represented). Selenium vapor pressures are calculated in [44] **from** [79]**.**

Thus, the objective is to analyze the consequences of the alloying process on the layers obtained. The hypothesis is that the formation of large alloys of Cu-Zn that was described in chapter 3 creates a segregation of zinc and tin, which are then the cause for the segregation of ZnSe.

This chapter is built with the following structure:

i) Investigation of Kesterite formation mechanism (short time, low temperature selenizations)

ii) Composition change after selenization: self-regulation of Cu/Sn ratio.

iii) Investigation of influence of metals segregation in the precursor on the segregation of ZnSe phase.

4.2 Mechanism of Kesterite formation

4.2.1 Timescale of Kesterite formation

Preliminary investigations on the timescale of Kesterite formation were done at 550°C on stoichiometric precursor samples. The choice of stoichiometric samples was motivated by the need to maximize the formation of Kesterite phase, and to avoid as much as possible secondary phases of any type. For this purpose, 2.5 x 2.5 cm^2 samples are cut, to provide four identical samples on which to perform the selenizations at four different times. Samples were selenized for various times at 550°C, 500 mbar N_2/H_2, with 100 mg Se and 15 mg SnSe in the reaction box. This process is done in an RTP oven to allow fast heating and cooling of the samples.

The phases present in the thin films are detected by XRD and Raman spectroscopy. These two techniques are complementary: XRD can probe the samples in the full depth of the material, whereas Raman spectroscopy is very surface sensitive, and analyses until less than 100 nm from the surface with a green laser (even lower with a blue laser). Because of their very similar XRD patterns, it is not possible to discriminate CTSe and ZnSe from Kesterite. Kesterite can only be distinguished by observing minor XRD peaks which are unique for this phase (at 2theta angles of 36.2° and 38.9°). Raman spectroscopy can differentiate these phases.

Figure 4.2a shows Raman spectra on the samples after selenization times of 30 s, 60 s, 120 s and 240 s. It can be observed that Kesterite (major CZTSe peak at 194 cm^{-1} [80], [81]) is already formed after only 30 s at the surface of the films. XRD diffractograms of the same samples (figure 4.2b) also show that the two Kesterite unique peaks at 22.2° and 28.5° are present, which indicates that Kesterite is present in all the layers. No Cu-Zn, Cu-Sn or pure metallic phase is observed, thus all metals reacted with selenium and the films are totally selenized. This observation is comparable to the case of sulfur: the sulfurization of a metallic sample at 550°C for a nominal time of 0 min (the sample is directly cooled down when the temperature reaches 550°C) leads to a film which does not contain any metallic phase [82].

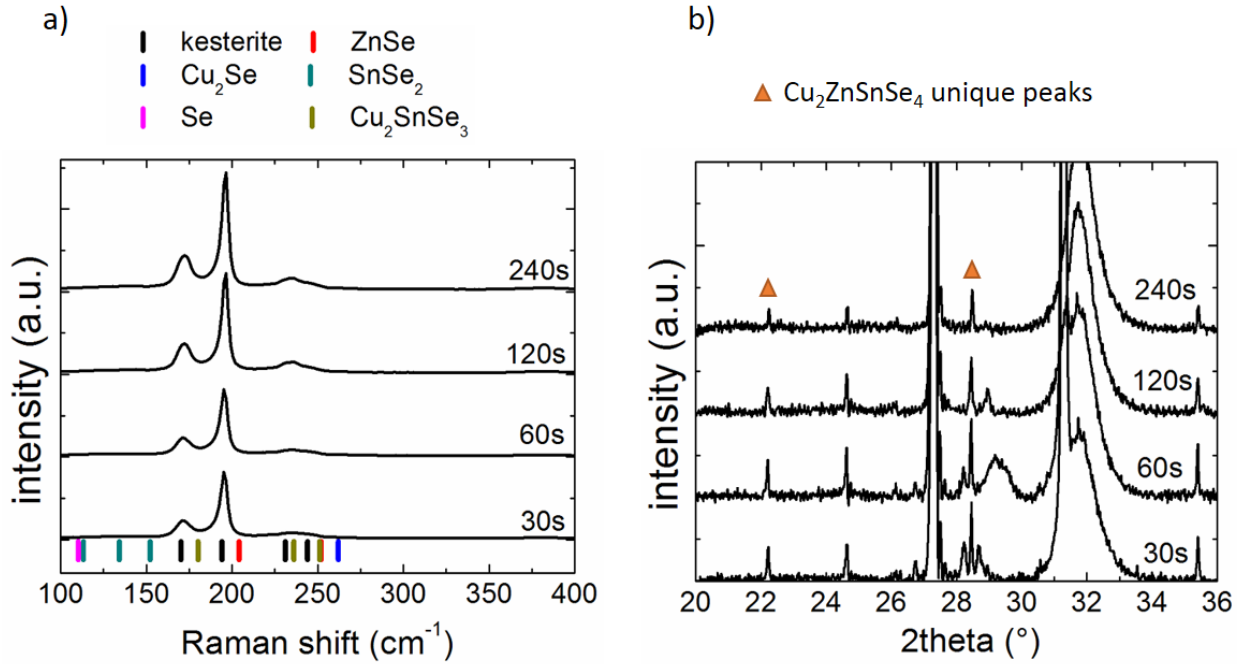

Figure 4.2: (a) Raman spectra and (b) XRD patterns of samples selenized at 550°C for times between 30 s and 240 s.

SIMS measurements were performed on all the absorbers synthesized for the study. Interestingly, only little change in the evolution of the chemical depth profiles was observed between the different selenization times. A typical SIMS compositional depth profile is shown in figure 4.3a.

Figure 4.3a shows that Cu and Sn have nearly the same evolution from the surface to the half of the depth. In the second half of the sample to the bottom of the layer, Cu decreases more slowly than Sn and Zn, indicating a probable presence of high concentration of Cu at the back of the absorber. In the case of Zn, the signal is decreasing at the back of the film, indicating a larger concentration of ZnSe on the surface. This is in agreement with SEM top view image (see figure 4.3b) showing large areas covered with ZnSe, and also in agreement with results reported by Arasimowicz [42] who reports segregation of ZnSe at the front of the thin films. A detailed microscopic study on ZnSe formation will be presented in section 4.4.

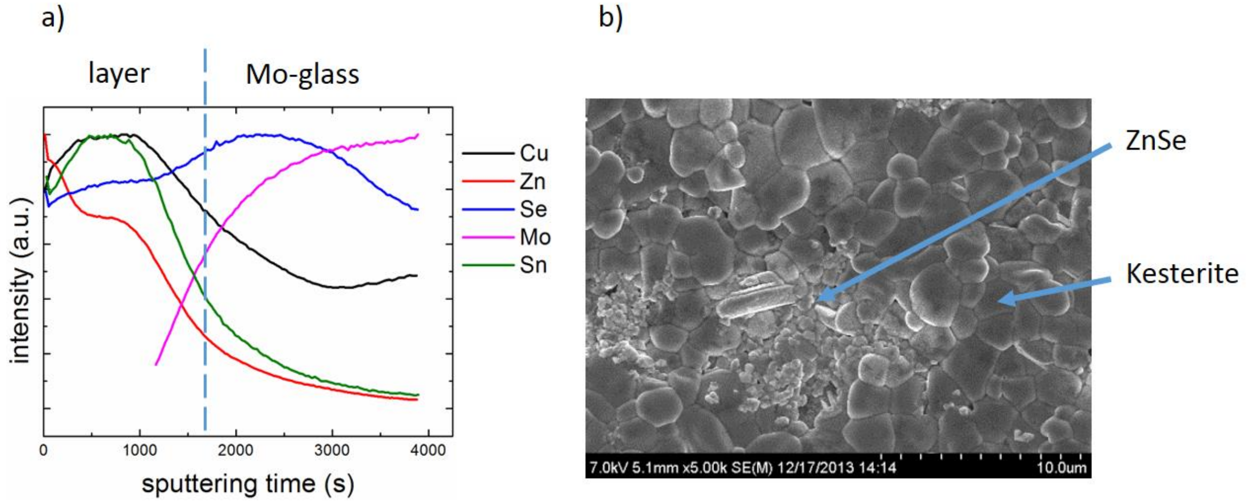

Figure 4.3: Stoichiometric Cu/Sn/Zn metallic stack selenized for one minute at 550°C in a Se and SnSe atmosphere: (a) SIMS composition depth profile, the signal of each element was normalized to its maximum value, the blue dashed bar indicates the probable position of the interface sample/back contact; (b) SEM top view image.

The only significant change with selenization time that was observed in this study concerns the evolution of composition, measured by EDX (figure 4.4). At early selenization times, a strong deviation from precursor composition is observed. The sample after 30s selenization appears to contain less Sn and more Zn, which can be explained by i) loss of Sn and/or ii) overestimation of Zn due to ZnSe patches at the surface of the samples. The evaporation of Sn is described by the following equation 4.4 [38]:

$$2\ Cu_2ZnSnSe_4 \rightleftharpoons 2\ Cu_2Se(s) + 2\ ZnSe(s) + 2\ SnSe(g) + Se_2(g). \quad (4.4)$$

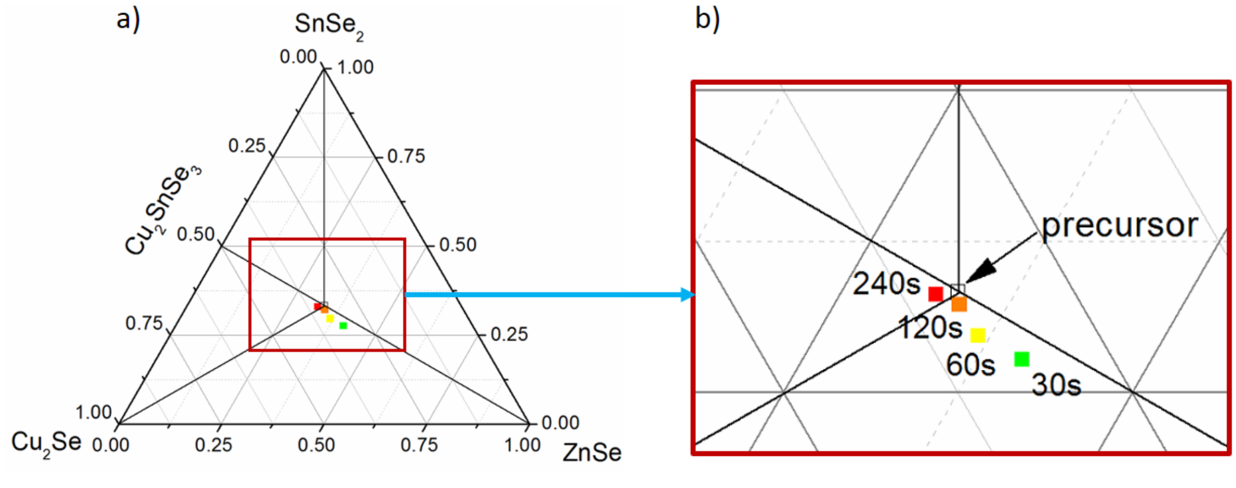

Figure 4.4: (a) Evolution of the composition of stoichiometric samples after selenization at 550°C for different times. (b) is a zoom of 4.4a.

With longer selenization, the composition recovers back to near the initial composition. This phenomenon has not been reported in the literature to the best of our knowledge, and a tentative of explanation of the mechanism can be done as described in figure 4.5.

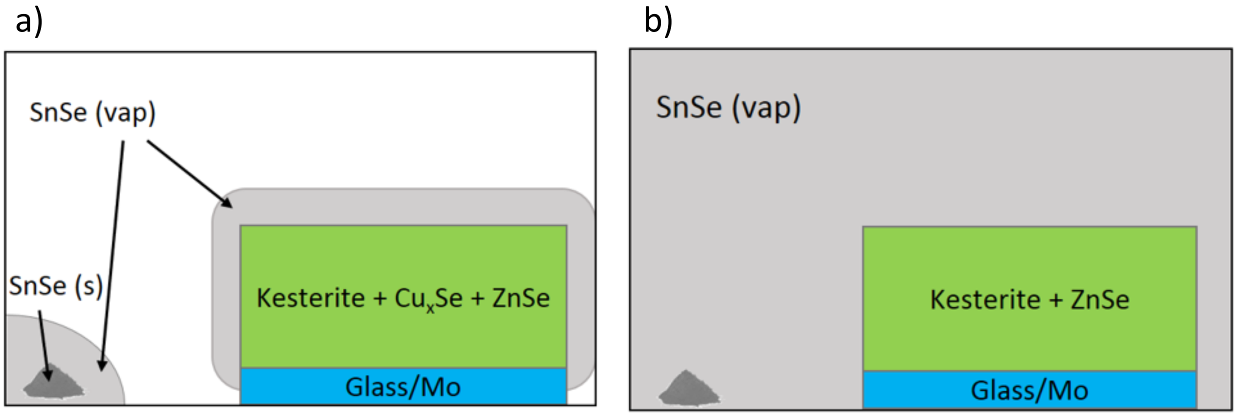

Figure 4.5: Schematic of sample during selenization (a) at time< t_1, and (b) at time > t_1.

Figure 4.5 represents the sample in the selenization chamber, together with SnSe powder on the side (Se powder is not represented here). t_1 is defined as the time when SnSe vapor evaporating from the SnSe powder starts to reach the sample. Before the time t_1, the SnSe vapor pressure on top of the sample is only generated by the evaporation of SnSe from the sample. Thus, during the selenization, the SnSe formed evaporates, and ZnSe and Cu_2Se formed segregate respectively at the front and at the back of the layer. Then, for time >t_1, the vapor of SnSe from the powder in the graphite chamber reaches the surface of the sample, which causes a re-incorporation of Sn in the sample, this sample reacting with Zn and Cu to form Kesterite. This re-incorporation occurs until the composition reaches the precursor composition.

In conclusion, this study of selenization at 550°C showed that after 30s at this temperature, the samples are already totally selenized. Only tin gas phase exchange is observed; phase formation (for Kesterite) and disappearence (ZnSe and Cu_2Se) are supposed. XRD, Raman and SIMS analyses all suggest that Kesterite formation is nearly complete after a selenization process at 550°C for 30 s. Thus lower selenization temperatures were investigated, and the temperature of 400°C was retained for the following study.

4.2.2 Mechanism of selenization

In order to investigate the Kesterite reaction mechanism the temperature was lowered to 400°C to decrease the rate of reactions and have the opportunity to observe the intermediate reactions. At this temperature, most of the literature investigating selenization temperatures shows that Kesterite is forming (see section 4.1.1). For this study, 2.5 x 2.5 cm^2 samples of the same composition as the reference sample of chapter 3 are cut, to provide four identical samples on which to perform selenizations at four different times. The results will be presented by technique: first the in-depth distribution of elements is analysed on samples selenized for 1 s, 30 s, 100 s and 300 s by SIMS, then the same samples are analysed with XRD, Raman and finally EDX.

After only 1 s of selenization at 400°C, SIMS measurements (figure 4.6a) show that Se is only detected at the surface of the sample (zone 1 of the spectrum). In this surface zone, the only other element detected by SIMS is zinc. This thin layer (100-200 nm) of Se and Zn can be observed on the SEM cross section image 4.6b. It probably contains ZnSe together with condensed pure Se. The sample bulk (region 2 on spectrum 4.6a) is only composed of Cu, Sn and Zn which are alloyed.

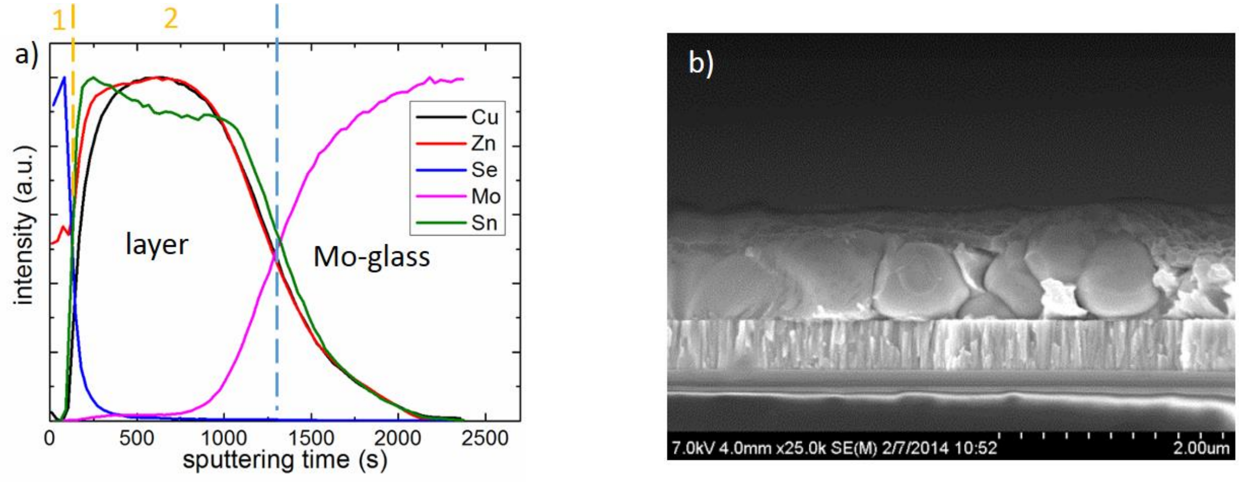

Figure 4.6: (a) SIMS composition depth profile and (b) SEM cross section image of a sample after 1s selenization at 400°C. The dashed lines on figure 4.6a indicate the limits between different zones of the samples: substrate, sample region 1 and sample region 2.

The evolution of distribution of the elements at different selenization times is presented in the following figure 4.7. These results confirm the observations of Arasimowicz, who shows very similar depth profile SIMS results by investigating different times of selenization with a high background pressure of N_2/H_2. Because of the different processes investigated, the times corresponding to each type of profile are different. Only the first profile (after 1s selenization) is not observed in the study by Arasimowicz: the first profile reported corresponds to a nearly fully selenized sample which resembles that of figure 4.7b. This figure 4.7b shows that after 30 s, Se is much more incorporated in the film than after 1 s. This remarkably leads to a strong shift of Sn content to the back of the layer, as evidenced by SIMS, suggesting that either Sn diffuses to the back of the sample, as proposed by Arasimowicz [42] or Cu and Zn diffuse to the front of the film, and react with Se to form Cu_2Se and ZnSe. This is in accordance with thermodynamic and kinetic data [83].

An alternative explanation for the tin depletion from the surface can be given by considering results from the previous study (section 4.2.1). Due to the lower background pressure of SnSe at early selenization stages, SnSe easily evaporates if it does not react either to form the ternary Cu_2SnSe_3, or to form Kesterite.

Thus, part of the SnSe appearing at the surface evaporates, which could explain why Sn content is decreasing from the back to the surface of the sample. Then, at longer selenization times, Sn appears at the front of the sample, by reaction of gas phase SnSe (SnSe powder is present in the selenization chamber to provide a partial pressure of SnSe in the vapor phase) with Cu_2Se and ZnSe to form Kesterite, as described in section 4.2.1. This can be the origin of the tin self-regulation mechanism.

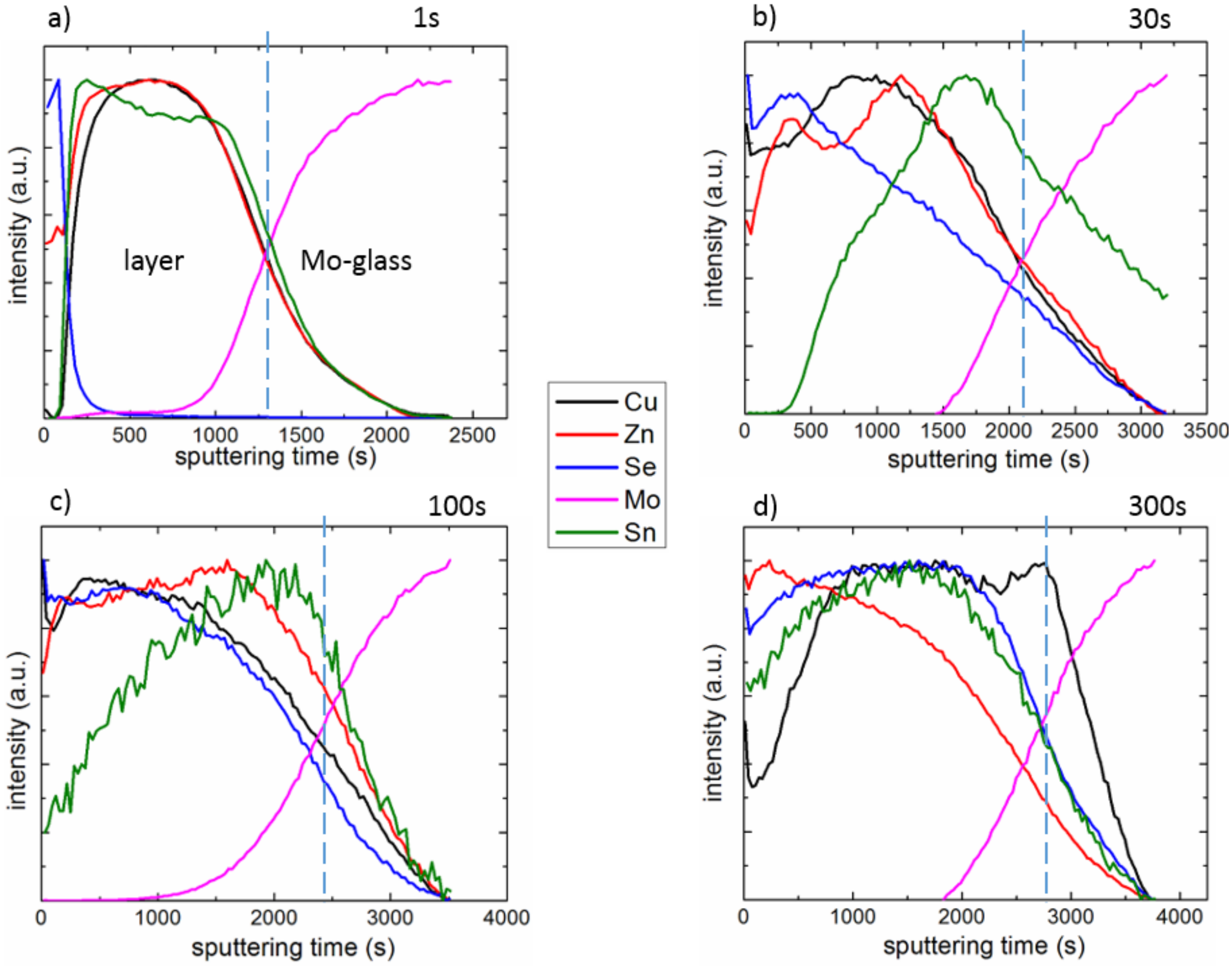

Figure 4.7: SIMS composition depth profiles of samples selenized at 400°C for (a) 1 s; (b) 30 s; (c) 100 s and (d) 300 s.

Figure 4.7 shows that for Cu and Zn, at 30 s and 100 s the profiles are relatively similar, both are quite homogeneously distributed in the films (with a decrease at the back of the layers, due to the higher Sn content). However, at 300 s Zn is more at the surface of the sample, which indicates a probable segregation of ZnSe at the surface. Interestingly, at 300 s the Cu seems to be diffusing into the $MoSe_2$ back contact.

XRD analyses were performed as well on the same samples. It allows following the phase formation or disappearance as a function of the selenization time. However, due to the complexity of the system displaying numerous possible phases, three of which have a large number of common reflection peaks

(Kesterite, Cu_2SnSe_3 and ZnSe), it is quite difficult to detect without doubt certain phases. Only the study of unique peaks associated only to one of the phases can lead to a conclusion on the presence of the phase, but such unique peaks are normally the least intense. A summary of the phases that can be detected is thus presented in figure 4.8, showing at which times of selenization these phases appear or disappear in the samples. For more details on the method of detection of these phases and which XRD peaks were studied, the complete results are shown in the appendix A.

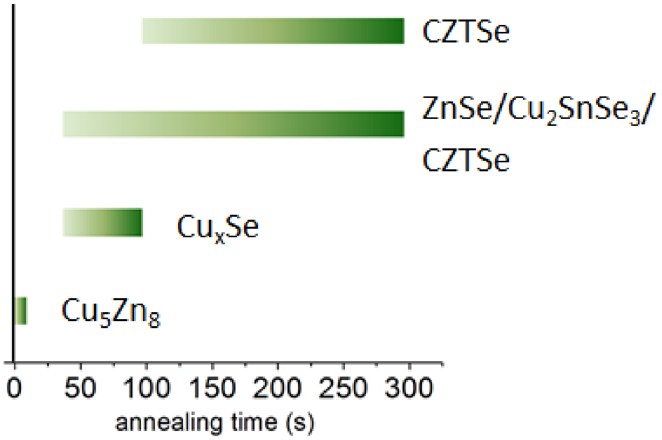

Figure 4.8: Evolution of observed crystalline phases after selenization at 400°C identified by XRD measurements. The CZTSe bar at the top of the figure represents the evolution of the unique Kesterite peaks.

After 1 s selenization, only metallic phases are detected, which confirms the analysis done with SIMS data, stating that only a 100-200 nm thin top layer contains Se, and the rest of the layer is composed of alloys of Cu-Sn and Cu-Zn. Kesterite appears to form only after 100 s in the samples, which as well correlates with SIMS results, showing Sn arrival to the front of the samples and thus reacting with Cu, Zn and Se to form Kesterite. Cu_2Se phase is also detected, but only in the layers selenized for 30 s and 100 s.

Micron resolved Raman measurements were performed to analyse the surface of the samples. This analysis area is very local compared to SIMS (≈ 2500 μm^2) and XRD (≈ 0.5 cm^2). Thus, it is possible to distinguish between different zones of each sample, and in particular to avoid Cu_2Se crystals on the surface. The following results concern measurements performed on samples regions free from the large surface Cu_2Se crystals. Only the green laser excitation spectra are shown in figure 4.9.

After 1s, the Raman signal is very low. Only two peaks corresponding to ZnSe (Raman mode at 250 cm^{-1} [84]) and perhaps a very small Kesterite peak (major CZTSe peak at 194 cm^{-1} corresponding to the A1 vibrational mode arising from Se vibrations [80], [81]) are detected. After 30s, a Cu_2Se peak appears (263 cm^{-1} [85]), which is detected on all areas of the samples that were analysed (even by avoiding the large Cu_2Se crystals), suggesting that Cu_2Se is present everywhere on the surface at this stage of selenization. The Kesterite peak is already present after 30 s, and is increasing at 100 s and 300 s. Blue excitation Raman spectra show the presence of ZnSe on the surface of the samples at all the times.

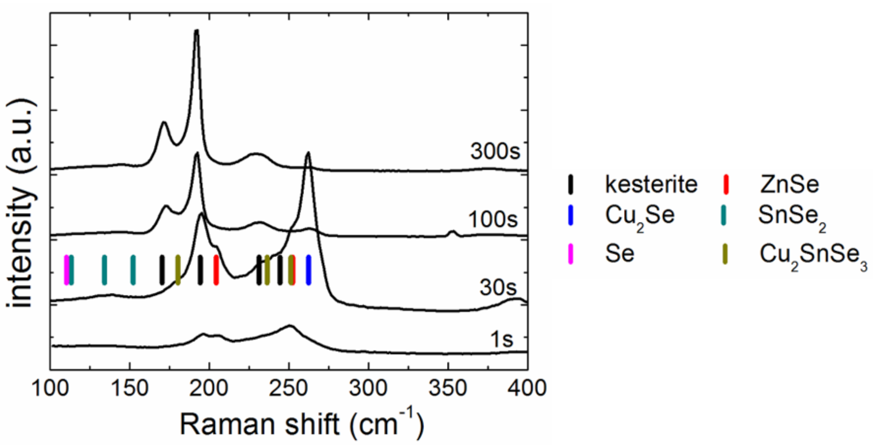

Figure 4.9: Raman spectra of the surface of samples after selenization at 400°C for different times. The laser wavelength is 532 nm.

Large area EDX measurements were made on all the samples, and the metallic composition was calculated and plotted onto a ternary phase triangle shown in figure 4.10. As shown on ternary diagrams of this figure, the evolution of composition of the samples as a function of selenization times is indicated by the arrows. The composition measurements are difficult to interpret due to the non-uniform depth distribution of the elements as observed in the SIMS depth profiles. Nevertheless, in accordance with the previous measurements, a general trend can be observed: first the decrease of Sn quantity at the front of the sample, and a segregation of ZnSe at the top of the layer which leads to an overestimation of Zn by EDX. The segregation of ZnSe at the front induces a decrease of Cu and Sn contents in this area for the longer selenization times (300 s).

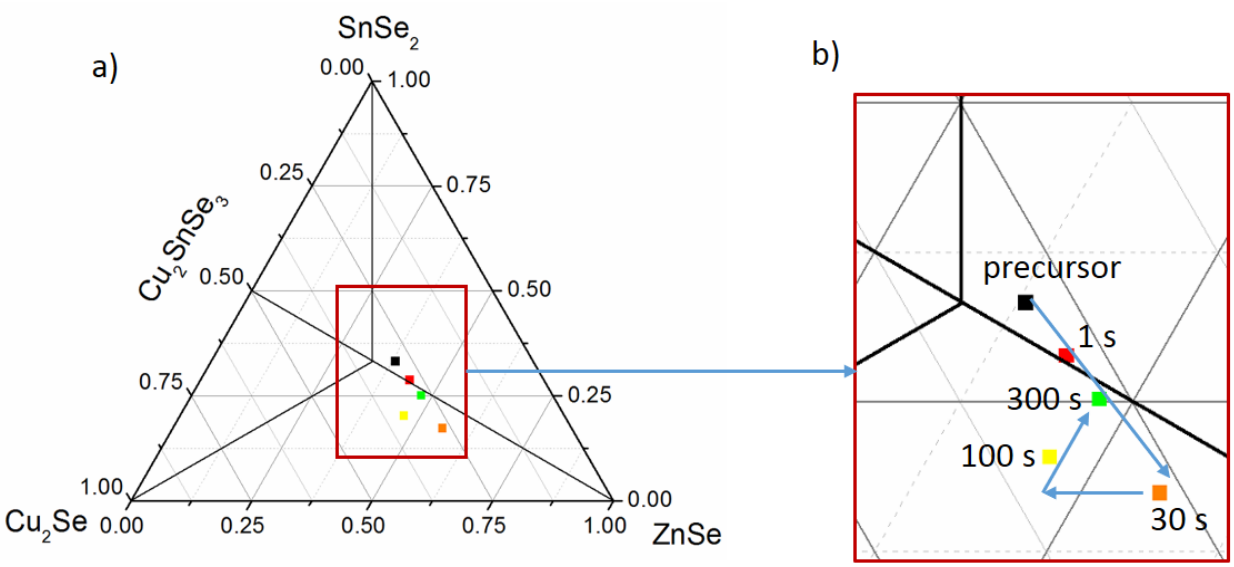

Figure 4.10: (a) Composition of samples selenized at 400°C for different times measured by EDX. (b) is a zoom of 4.10a.

Figure 4.11 shows images of the surface of the samples selenized at 400°C. Cu_2Se grains (large dark grains on the surface) are present at 30 s and 100 s only. This is in agreement with XRD results. Top view images also show a quite inhomogeneous distribution of ZnSe on the surface. ZnSe grains appear as small brighter grains, and form islands of some 10 - 20 microns on the surface. The apparition of Cu-Se phases at the beginning of the process followed by its disparition from the surface was reported in several studies [74], [76], [77].

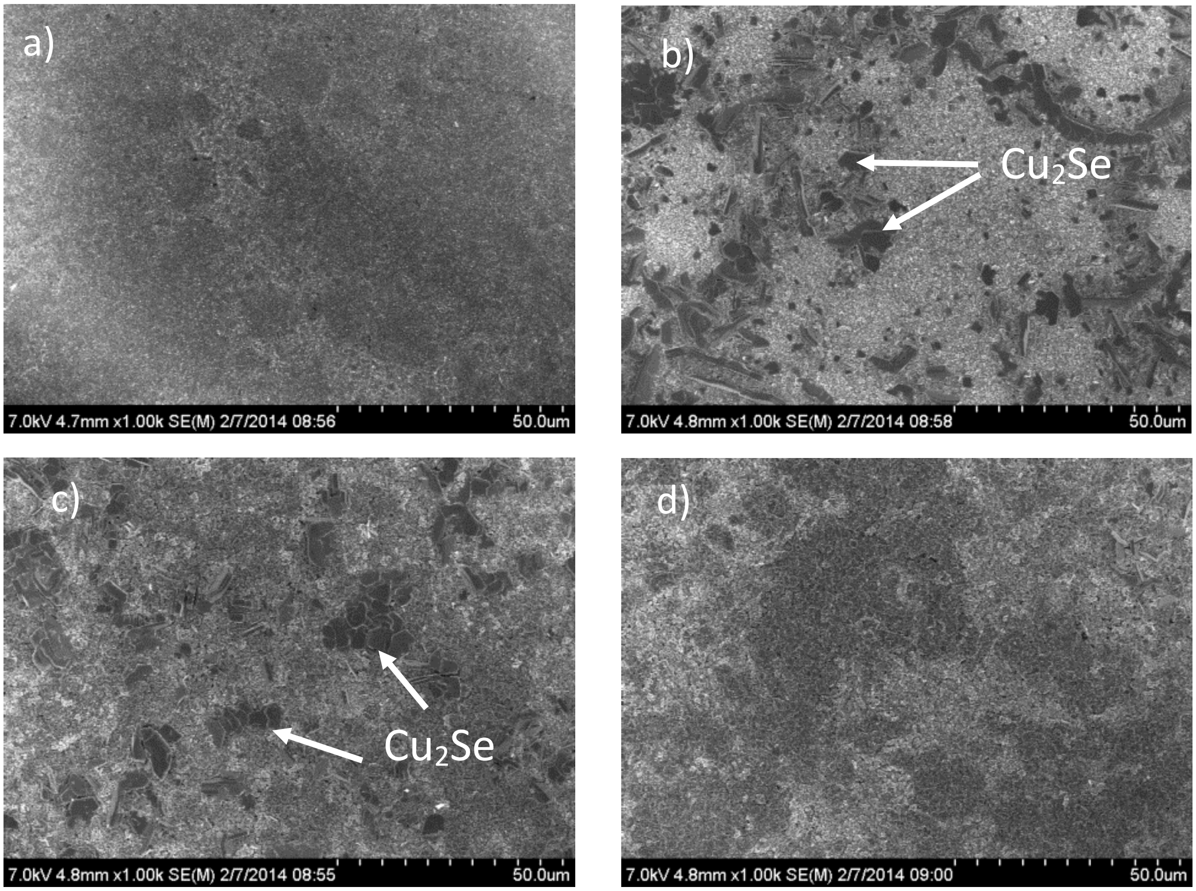

Figure 4.11: SEM top view images of samples selenized at 400°C for (a) 1 s, (b) 30 s, (c) 100 s, (d) 300 s.

Considering the evidence gathered by all analyses of the composition and phases present in the films, a summary of the selenization mechanisms is proposed in figure 4.12. It describes the most probable structure of the samples at each of the times investigated in the study.

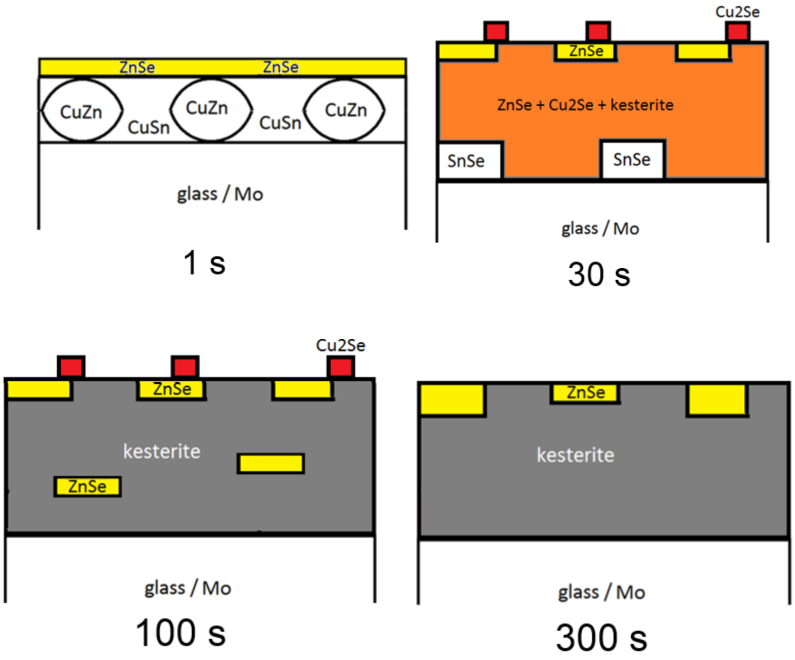

Figure 4.12: Schematic representation of Kesterite formation mechanism.

At 400°C after 1 s selenization: only the first 100-200nm reacted with Se, to form mainly ZnSe.

After 30 s, the layer is partially selenized, Sn has evaporated as SnSe from the front. Cu_2Se forms large crystals at the surface of the samples, and is also mixed with ZnSe and some Kesterite at the surface.

After 100 s, Sn supplied from SnSe gas phase is reincorporated in the film to react with ZnSe, Cu_2Se and Se to form Kesterite with the reaction 4.5.

$$\mathrm{ZnSe\ (s) + Cu_2Se\ (s) + SnSe\ (g) + Se \rightleftharpoons Cu_2ZnSnSe_4\ (s)} \tag{4.5}$$

The quantity of Kesterite is then sufficient to be detected unambiguously by XRD. Cu_2Se is still present on the top of the layers.

After 300 s, more Kesterite has formed and Sn is no more segregated at the back. At the surface of the sample, more ZnSe is present, and Cu_2Se is no longer detected. Diffusion of Cu to the back of the layer is detected by SIMS, possibly in the $MoSe_2$, however no evidence of the presence of Cu_2Se at the back of the layer was found.

This first study helps to understand how and when Kesterite and secondary phases form during the selenization process, which is a first step to the global understanding of phase formation. During the beginning of the incorporation, binary selenides are formed as expected and in agreement with the literature. The novelty of this study is to show that during this first formation of binary selenides, a high quantity of tin is disappearing from the front of the layers, most probably due to the evaporation of SnSe. Then, the reincorporation of Sn in the layers is observed, via reaction of SnSe with ZnSe and Cu_2Se to form Kesterite (or formation of CTSe). The supply of tin via gas phase seems to be sufficient to convert all the Cu_2Se into Kesterite. The second important analysis step is the study of selenization under a standard selenization process (550°C for 30 min), to investigate the evolution of composition after this step, which will be presented in the following.

4.3 Self-regulation of tin content.

This section aims at understanding the changes of composition which occur during a standard selenization, and in particular study in details the effects of the decomposition reaction of Kesterite 4.6 [38], which was already presented in the introduction 1.3.4:

$$2\ Cu_2ZnSnSe_4 \rightleftharpoons 2\ Cu_2Se(s) + 2\ ZnSe(s) + 2\ SnSe(g) + Se_2(g). \qquad (4.6)$$

For this, Cu-Sn-Zn samples of different compositions are selenized using the "standard selenization process", which corresponds to an annealing at 550°C for 30 min in a tubular furnace, in presence of Se and SnSe powders. These samples are analysed with EDX after this process, to measure their composition, which changes strongly, as will be described now.

A very broad range of compositions was chosen (figure 4.13, square points). The compositions before and after selenization are shown in figures 4.13a and 4.13b. Interestingly, only four samples out of the eight prepared have a near-invariant composition after selenization: points 4, 5, 6 and 7. This can be explained by the fact that they are in domains of the phase diagram where the phases present have all very low vapor pressures: point 4 is composed of $Cu_2ZnSnSe_4$ and Cu_2SnSe_3, point 5 corresponds to pure Kesterite, point 6 contains $Cu_2ZnSnSe_4$ and ZnSe, and point 7 a mixture of Cu_2Se and $Cu_2ZnSnSe_4$. For points 1, 2 and 3, the change of composition is quite important: all compositions have apparently lost tin, and the final compositions remarkably lie all on the line of the ternary phase diagram which corresponds to Cu/Sn=2. Thus, there is a self-regulation of the ratio Cu/Sn in this region, which can easily be explained by the combination of the following equations 4.7 and 4.8.

$$2\ Cu_2ZnSnSe_4 \rightleftharpoons 2\ Cu_2Se(s) + 2\ ZnSe(s) + 2\ SnSe(s) + Se_2(g). \qquad (4.7)$$

$$SnSe\ (s) \rightleftharpoons SnSe\ (g) \qquad (4.8)$$

At 550°C, the vapor pressure of SnSe is 3.6×10^{-3} mbar [39]. Thus, until complete formation of Kesterite and ZnSe, all excess SnSe evaporates, and the excess tin is lost from the sample.

Furthermore, this regulation seems to also occurs for tin-deficient samples, for which Cu/Sn>2. In the case of sample 8, a slight increase of tin content is observed, however the incorporation of tin is not sufficient to reach Cu/Sn=2. This can be explained by a consumption of SnSe(s) provided by the equation (4.8), to form Kesterite by reacting with ZnSe and Cu_2Se (reaction 4.7). Similarly, in the case of sulfide compounds Berg et al. [86] showed that Kesterite absorbers can be formed by performing a sulfurization process on a sample containing Cu and Zn only. All tin necessary for the formation of Kesterite is provided via evaporation of SnS.

A very similar observation was recently reported, in the case of sulfur annealings [43], where a same self-regulation of Cu/Sn ratio is found to occur, with the difference that this regulation also occurs fully for tin-deficient samples, for which Cu/Sn>2. These samples also reach Cu/Sn=2 after sulfurization.

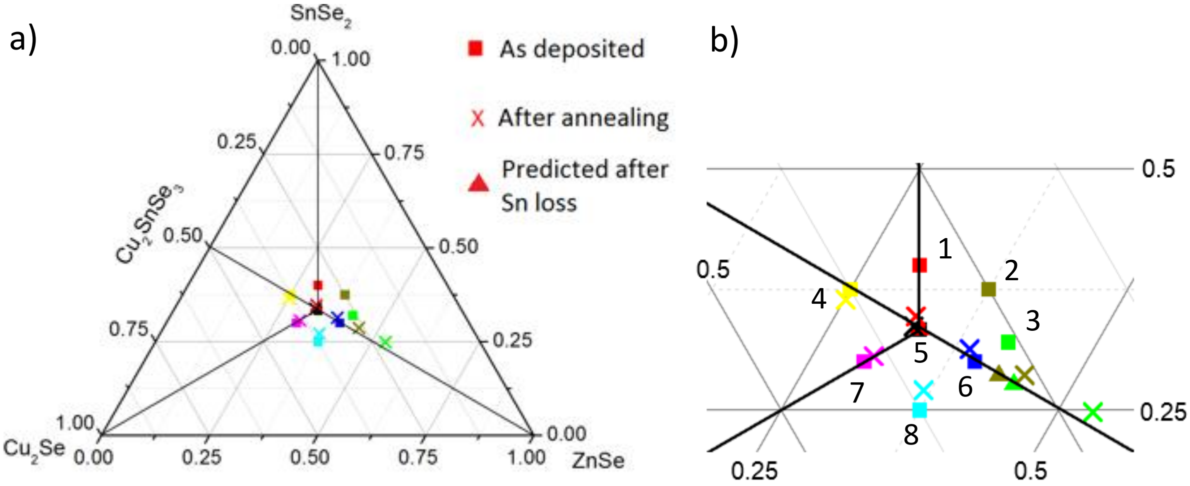

Figure 4.13: (a) Composition of Cu-Sn-Zn samples as deposited (squares), and after selenization (crosses) at 550°C for 30 min with Se and SnSe, plot on the usual Cu_2-Sn-Zn ternary diagram. The name of each sample is a number, placed next to the plot of the as deposited composition. Each color corresponds to a single sample. (b) is a zoom of the central part of the ternary diagram (a). For samples in the Zn-rich region, a predicted composition after tin loss is represented (triangle points).

To go further into the analysis of composition change, the expected composition of samples 1, 2 and 3 assuming tin loss was calculated, and plotted in figure 4.13b (triangles). These compositions were calculated by only subtracting the amount of tin necessary to reach a value of Cu/Sn=2. It can be seen that tin loss occurred, but also a gain of zinc had to occur for points 2 and 3. This can be explained easily by the fact that ZnSe has a tendency to grow on the surface of the samples, which causes an overestimation of zinc ratio by EDX.

A second more detailed study was done in the domain of Cu-poor, Zn-rich compositions, as shown in figure 4.14.

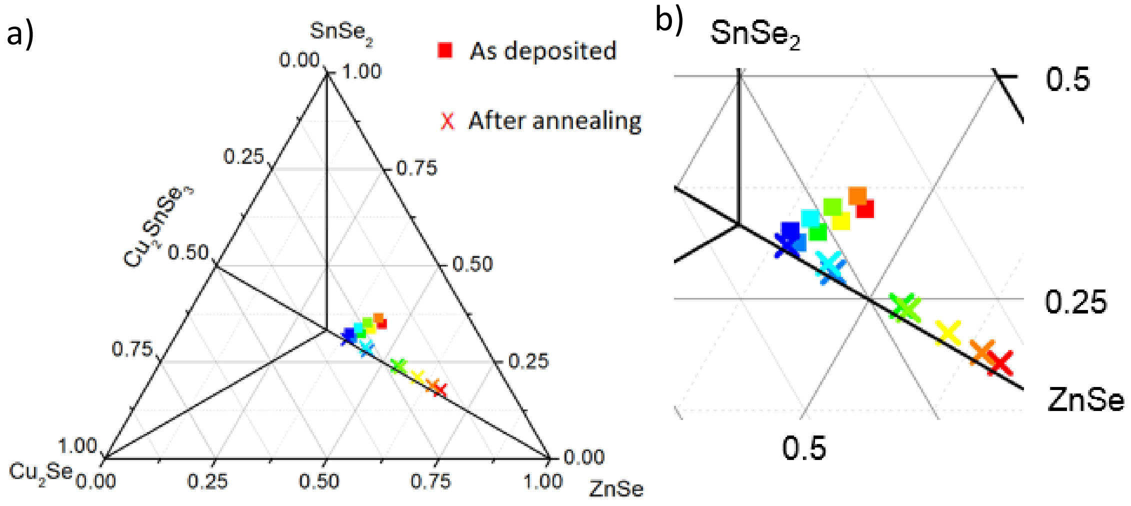

Figure 4.14: (a) Composition of Cu-Sn-Zn samples as deposited (squares), and after selenization (crosses) at 550°C for 30 min with Se and SnSe, plot on the usual Cu_2-Sn-Zn ternary diagram. Each color corresponds to a single sample. (b) is a zoom of the central part of the ternary diagram (a).

The change of composition after selenization of these samples show clearly the same effect (figure 4.14), which was just described: all samples lose their excess tin, such that their composition reaches final ratio Cu/Sn=2. And here as well, an overestimation of zinc is observed, an effect which is increasing with the zinc excess of the sample, due to surface ZnSe. All samples grown for this study were implemented into solar cell devices, the results are presented in the next chapter.

This study shows that under the standard selenization conditions used for this thesis (annealing at 550°C for 30 min in presence of Se and SnSe powders, in 10mbar N_2/H_2), no SnSe phase is expected to remain on the samples after selenization if the precursors have a composition with Cu/Sn<2 and Cu/Zn<2 (the domain where are the points of figure 4.14), because of the evaporation of all excess Sn via formation of volatile SnSe. Only Kesterite and ZnSe are the phases expected.

In the following section and chapters of this work, all samples presented are grown with ratios of Cu/Sn<2 and Cu/Zn<2, thus the predominant secondary phase is ZnSe. The last section of this chapter will be concentrated on this secondary phase, which becomes now clearly the main challenge to achieve efficient solar cells.

4.4 Segregation of zinc selenide

As was shown in section 4.2, ZnSe mainly appears on the surface of the absorbers, and a large segregation of this phase at the scale of dozens of micrometers is usually observed. This section presents an investigation of the causes of large segregation of surface ZnSe, and tries to provide solutions in order to minimize this problem. The results of the investigation have been published in reference [87].

To explain the size of ZnSe "islands" on the surface of the thin films, it was first hypothesized that prealloying mechanisms could be the origin of the segregation. As a reminder, it was shown in section 3.4.3 that Cu-Zn alloys of large sizes are segregating because of alloying mechanisms at 350°C. Furthermore, even if the standard process used for this thesis does not include any deliberate prealloying (annealing at 200-350°C) treatment before the selenization, the selenization step necessarily includes a first part during which the sample is only heated, and the temperature is not sufficient to evaporate Se (section 4.1.2).

Thus, for the study that is about to be presented, the samples were prealloyed after electrodeposition, in order to be able to first observe the segregation of metals, and afterwards to compare the repartition of elements before and after selenization. For this analysis, the same sample which was presented in the section 3.4.3 (effect of alloying), called reference sample, is analysed at the exact same "position of interest" after selenization, by the same method of EDX mapping, combined with other techniques such as micro-Raman, micro-PL and XRD. For easier comparison, some of the results already described in chapter 3 will be shown again. The analysis of this sample at the same position is made possible by marking of the surface (identical location technique, described in chapter 2). This type of investigation at a large scale (50 micrometers) on an identical location is the first to be reported. All previous literature reports on the alloying of precursor samples are done at a low scale of less than 10 micrometers (at this scale, the extent of Cu-Zn islands cannot be detected), and without tracking of the segregation of metals at an identical location on a sample.

Figures 4.15a and 4.15b show images of the surface of the reference sample at the exact same position, before and after selenization. To analyse the distribution of elements, the same method was applied as described in chapter 3: an EDX map of the area of interest after selenization was measured, and from this EDX map molar fractions of each metal are calculated and their distribution is displayed as maps. All molar ratios presented in this section 4.4 are metallic molar ratios, as described in section 4.1. They are the same as the molar fractions presented in chapter 3, for an easier comparison with previous results.

Figures 4.15c and 4.15d are shown here as a reminder and an example of the composition maps that were obtained from EDX mappings. They display molar fractions of tin before and after selenization. As a broad reminder of the investigations of the section 3.4 (alloying), the area of interest is composed of a Cu-Zn phase in region 1, and of a mixture of Sn, Cu-Sn and Cu-Zn in region 2. For more details, the reader is invited to refer to section 3.4.3.

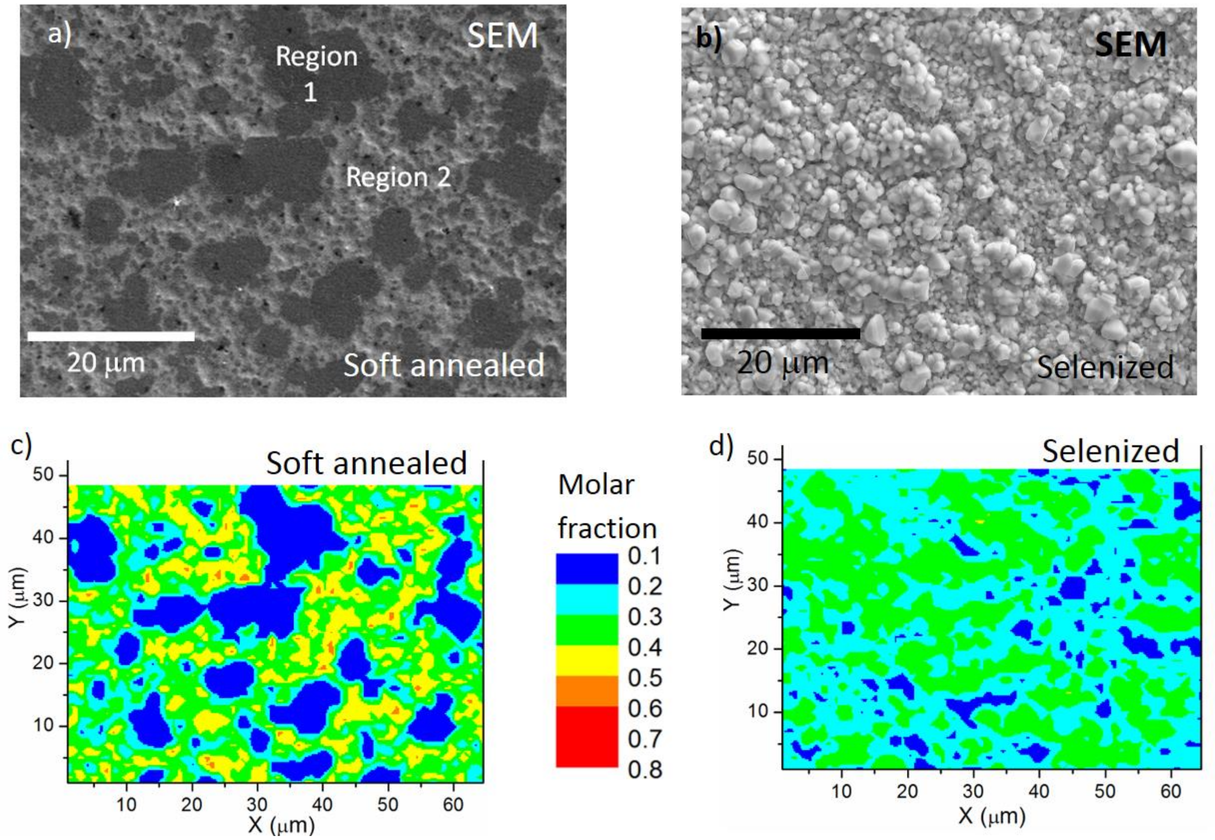

Figure 4.15: Images and chemical maps of the reference sample on the area of interest: (a) SEM image after alloying at 350°C for 30 min, (b) SEM image after selenization, (c) tin molar fraction distribution after alloying and (d) tin molar fraction distribution after selenization. The molar fraction color scale is the same for all chemical maps presented in the thesis.

To investigate in details the changes that occurred after selenization, the distribution of compositions over the total area measured with EDX is first considered. These compositions are displayed in figure 4.16a (before selenization) and 4.16b (after selenization). There is a noticeable change in the distribution of composition from bimodal and globally invariant Cu_2/Zn ratio for the metallic alloy precursor to unimodal, with globally invariant Cu_2/Sn ratio for the selenized absorber layer (figure 4.16b). Most of the compositions in the area of interest are centered on the Kesterite composition (0.33 Cu_2 0.33 Sn) with a tail of compositions along the $Cu_2ZnSnSe_4$–ZnSe tie line. Less than 3 % of the area of interest has a composition where Cu_2SnSe_3 could be present. The extension of compositions to very zinc-rich zones of the ternary diagram (ratio of Zn of around 0.7) can be explained by the formation of ZnSe preferentially at the surface of the films, which then induces an overestimation of the Zn content measured by EDX.

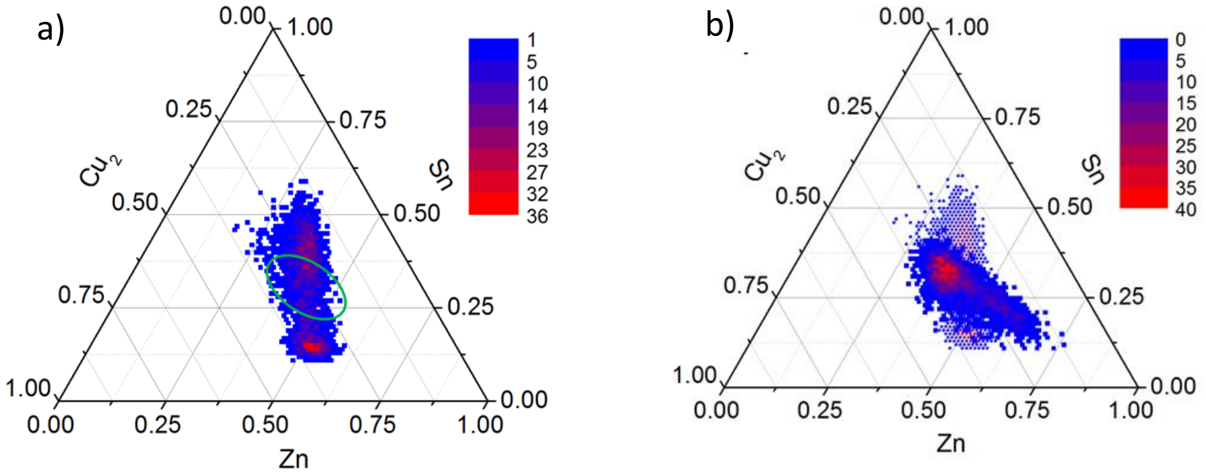

Figure 4.16: (a) Compositions of every point of the chemical maps after alloying. The green oval shows the limit of spread of compositions of the map of the as-deposited sample (figure 3.8b); (b) compositions of every point of the area of interest after alloying (faded points) and after selenization (bold points). Each composition on these diagrams has been color-coded to represent the number of points which have the same composition.

Figure 4.17a, 4.17b and 4.17c show the Sn, Cu_2 and Zn molar fractions over the position of interest. As expected from the distribution of compositions of figure 4.16b, the element which has the highest amplitude of molar fractions is zinc. Considering only the zinc chemical map (4.17c), the position of ZnSe phase should be in areas for which Zn molar fraction is the highest. Studies of Choubrac et al. show for example that the domain of stability of Kesterite phase extends only to a zinc molar fraction of around 0.41 [71] at 750°C. It is thus expected that at a lower temperature of 550°C, this domain of stability is reduced. Over the value of zinc molar fraction of 0.41, ZnSe phase must then exist, together with Kesterite. This was confirmed by µ-PL/Raman measurements of the position of interest. The PL intensity was measured and integrated in the range 1.22-1.52 eV in figure 4.18 (which is the fingerprint region for doped ZnSe in Kesterite [88]), providing a PL map (figure 4.17d). A good agreement is observed between the PL map and regions of the selenized film with Zn molar fraction > 0.45.

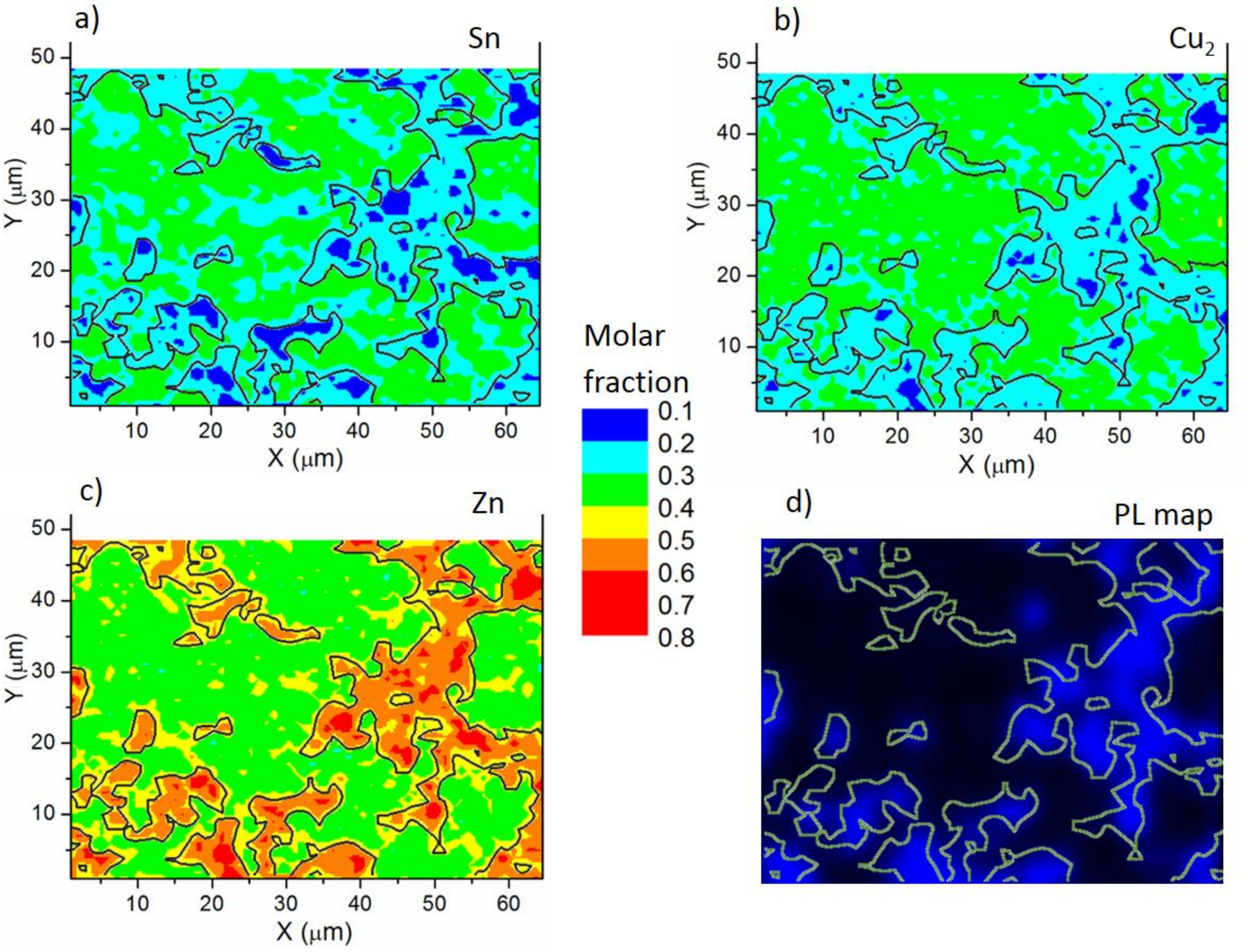

Figure 4.17: Chemical maps displaying Sn (a), Cu_2 (b) and Zn (c) molar fractions of area of interest after selenization. (d) micro-PL map showing integrated intensity between 1.22 and 1.52 eV of area of interest after selenization. All maps are overlaid with a contour map of iso-Zn with molar fraction 0.45 (in black for a, b, c and in green for d). The molar fraction color scale is the same for all the chemical maps (a, b and c).

Examples of PL and Raman spectra from very low and very high ZnSe containing areas are shown in figure 4.18. The Raman spectra confirm the presence of Kesterite in both areas. This also shows that ZnSe is on or near the top surface, because otherwise, its luminescence emission would be absorbed by the Kesterite which has a bandgap below 1eV.

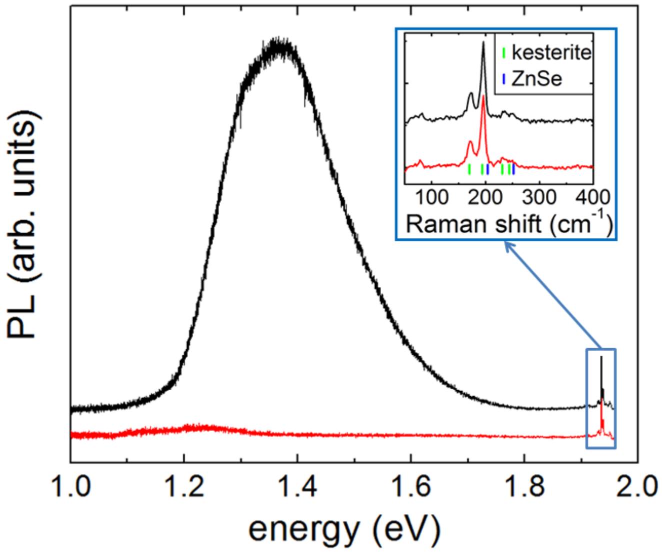

Figure 4.18: Examples of PL spectra obtained in high-zinc (black) and low-zinc (red) areas with Raman spectra of Kesterite observed in both cases (inset).

The comparison of zinc chemical maps before and after selenization provides very interesting insight on the origin of segregation of ZnSe: unexpectedly it appears that the location of ZnSe on the area of interest coincides more with the position of Zn-poor and Sn-rich areas before selenization (falling outside the black contour lines on map 4.19a). Quantitatively, 73% of the areas that have a ratio of Zn>0.45 are on zones which had a ratio of Sn>0.25 before selenization. It thus means that 73% of the ZnSe is placed on areas which were rich in tin (region 2) before the selenization, which confirms this tendency of formation of ZnSe on formerly Zn-poor and Sn-rich regions.

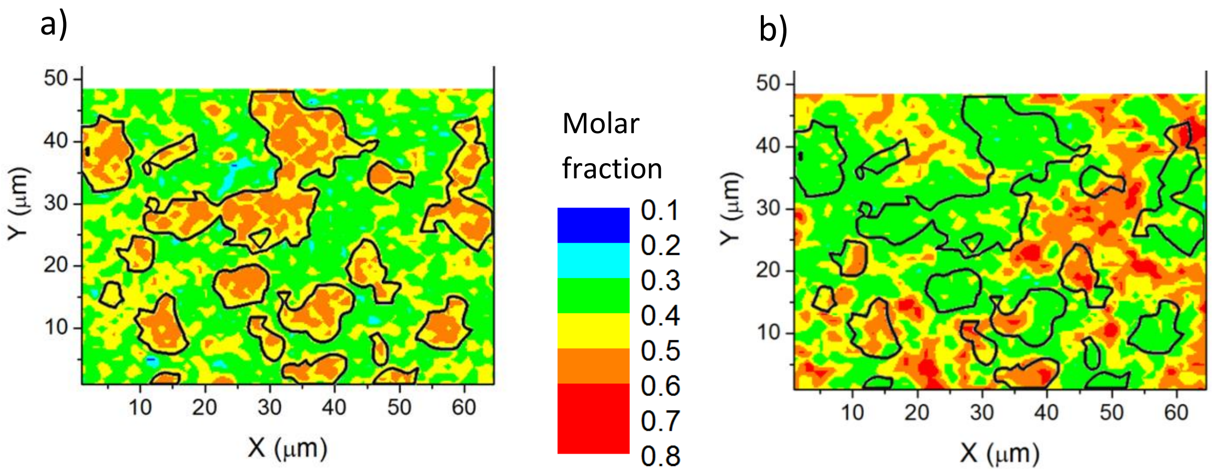

Figure 4.19: Chemical maps displaying Zn molar fraction of area of interest (a) after alloying and (b) after selenization. Black contour lines are the same for the two figures, and are defined by a molar fraction of Sn<0.25 (see figure 4.15c).

The greater presence of ZnSe in regions which were initially tin rich could be explained by different kinetics of formation of kesterite in the two different zones described, as shown on the mechanism proposed in figure 4.20. During the selenization of the layer, Kesterite will form faster in the tin-poor areas (zone 1 in figure 4.20) than in the Sn-rich areas. This is due to the fact that Sn-rich areas contain mainly tin, with inclusions of Cu-Zn as described previously. Thus most of the selenium incorporated in the tin rich zone 2 will be "lost" by evaporation of SnSe. Differently in zone 1, Kesterite will directly form because of the presence of mainly Cu and Zn, the tin being provided either by gas phase (from zone 2 or from the SnSe powder present in the selenization box). As shown by the quasi-ternary diagrams with plots of the distribution of compositions before selenization (figure 4.16a), the ratio Cu/Zn is nearly invariant over the sample surface. Thus Cu/Zn can be assumed to be identical in zones 1 and 2. Furthermore, the value of Cu/Zn is lower than 2 (Cu is the limiting factor for the formation of Kesterite which requires two copper atoms for one zinc atom), thus the formation of Kesterite will decrease this ratio. Finally, because of the higher rate of formation of Kesterite in zone 1, Cu/Zn becomes lower in zone 1 than in zone 2, which is then a driving force for the migration of Cu from zone 2 to zone 1, and of Zn in the opposite direction. This is supposed to be the reason for the preferential formation of ZnSe in zone 2.

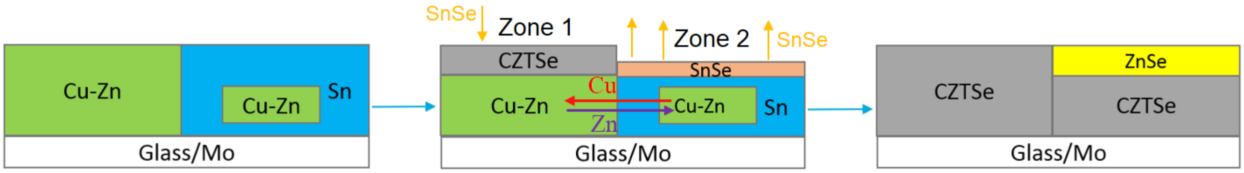

Figure 4.20: Mechanism of selenization proposed showing the preferential growth of ZnSe on area which are rich in tin before the selenization.

It can be concluded that the extent of metal alloy segregation occurring during a heating step affects significantly the extent of secondary phase segregation in the selenized Kesterite film. Counter-intuitively, ZnSe appears to segregate preferentially on areas formerly poor of Zn. Reducing the physical size of the metal alloys formed should reduce secondary phase segregation and improve device efficiency.

4.5 Summary: formation and segregation of Kesterite and secondary phases

The study of section 4.2 investigates the mechanism of reaction of selenization of metallic Cu-Sn-Zn layers. It shows the order of formation of the different selenide phases, which confirms the literature available on the subject. It further investigates a new concept of Sn self-regulation mechanism which is evidenced here and also in section 4.3 which shows that during selenization, any sample grown in the Cu/Zn and Cu/Sn region will lose its excess Sn to finally reach a ratio of Cu/Sn=2. This is due to the evaporation of SnSe. This study shows that after selenization, the system is expected to be mainly biphasic (Kesterite together with ZnSe). Thus, investigations were then concentrated on the formation of ZnSe phase, and especially its large scale segregation on the surface of the samples.

The last study (section 4.4) employs a method which is reported for the first time in the field of analysis of Kesterite solar cells, and consists to analyse a sample at a specific location at several stages of a process. Here, this investigation shows that the large extent of segregation of ZnSe at the surface of the absorber is due to alloying mechanisms, which lead to segregation of Cu-Sn and Cu-Zn compounds at scales of 10 - 20 micrometers. Unexpectedly, ZnSe is found to preferentially form on the places which formerly were poor in tin. This was explained by a lowering of formation rate of Kesterite in Sn-rich areas.

By combining the results of chapter 3, sections 4.2 and 4.4, a mechanism can be proposed as described in figure 4.21. Alloying of the metallic Cu/Sn/Zn stacks induces the formation of Cu-Zn islands of 10-20 micrometers, surrounded by Sn (and some Cu-Sn) with inclusions of Cu-Zn, as shown on figure 4.21a.

When selenium starts to be incorporated in the layers, it will form first Cu_2Se and ZnSe in the zone 1 of figure 4.21b. CZTSe will form as well later by incorporation of SnSe from the gas phase (SnSe evaporating from the SnSe powder or from zone 2). In zone 2, mainly tin is present, thus most of the selenium incorporated will form SnSe which evaporates because Cu_2Se and ZnSe are not yet present to react with SnSe. This is described in figure 4.21b, and corresponds approximately to a process time of 30s in the study of section 4.2.2. The higher rate of formation of Kesterite in zone 1 compared to zone 2 will decrease the ratio Cu/Zn in zone 1 faster than in zone 2, such that Cu/Zn (zone 1) < Cu/Zn (zone 2). This induces a migration of Cu from zone 2 to zone 1, and of zinc in the opposite direction. Probably the SnSe layer is too thin to be detected (the SnSe formed directly evaporates).

In the following step described (figure 4.21c), the film is fully selenized. ZnSe and Cu_2Se still remain in zone 1, and react with SnSe from the gas phase to form Kesterite (corresponds to 100 s of the study in section 4.2.2).

Finally, due to the migration of Cu to zone 1, the quantity of ZnSe in zone 2 is higher than in zone 1, which causes the segregation of ZnSe in zone 2.

This proposed mechanism is the first in the literature to propose an explanation for the tin self-regulation mechanism, and as well the first to show the link between segregation of metals during alloying and segregation of selenide phases.

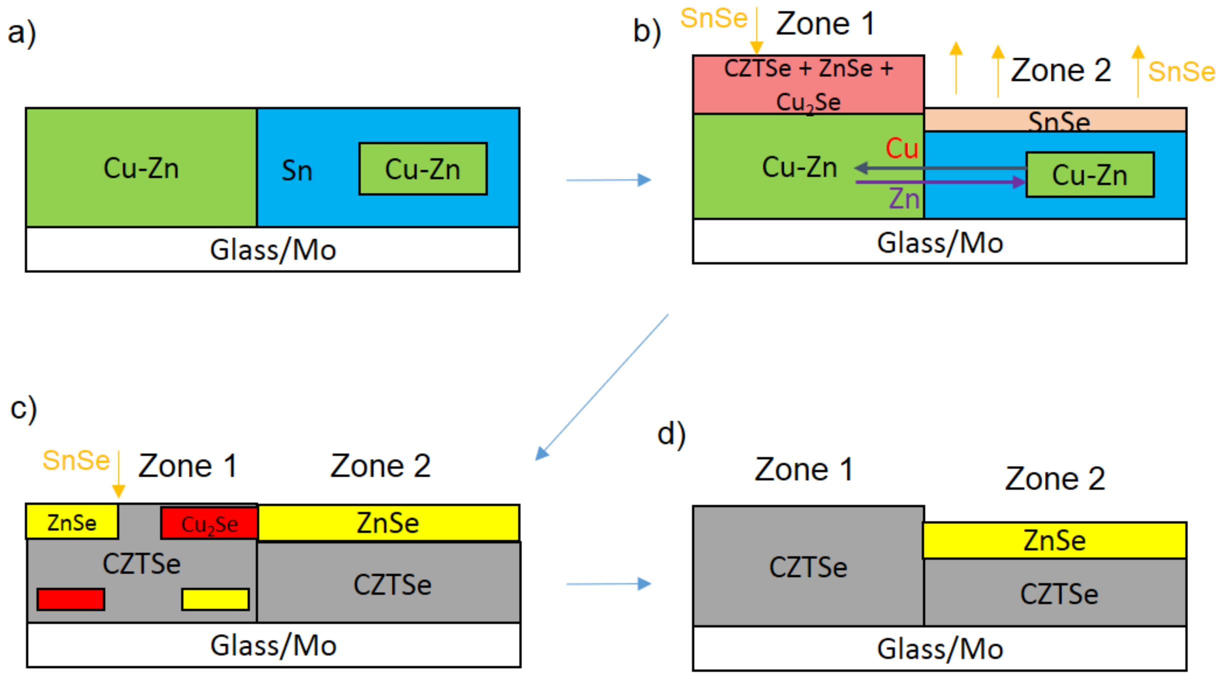

Figure 4.21: Schematic representation of formation mechanism of Kesterite, by combining results from chapter 2, section 4.2 and section 4.4.

5 Solar cells

Aim of the chapter

This chapter presents results concerning absorbers which were implemented into solar cell devices. The objective here is to analyze the performance of the solar cells prepared from the absorber layers described in chapters 3 and 4, and understand what parameters can be detrimental for the solar cells, in order to improve their power conversion efficiency. In particular, the effect of the presence of ZnSe in the layers will be investigated.

5.1 Introduction

5.1.1 Background

The highest efficiency reported for a pure selenide CZTSe device is 11.6 %, with an open circuit voltage of 423 mV, a short circuit current of 40.6 mA.cm^{-2} and a fill factor of 67.3 % [89]. The absorber is prepared by co-evaporation. For an electrodeposited precursor, the value of highest efficiency is 9.1%, with a V_{oc} of 421 mV, a J_{sc} of 33.4 mA.cm^{-2} and a FF of 64.6 % [41].

The bandgaps of the best selenide Kesterite devices usually reported are 1-1.02 eV [59], [89]–[91]. The corresponding open circuit voltage values are ranging from 380 mV to 430 mV, which correspond to a much higher V_{oc} deficit (difference between theoretical maximum V_{oc} and measured V_{oc}) than in the case of CIGS solar cells. Thus, improving the open circuit voltage of the Kesterite solar cells is currently one of the major objectives in this field.

Concerning the composition of Kesterite solar cells, as already mentioned in the previous chapter, it is widely accepted that secondary phases should be avoided [24]. However, the best efficiencies are obtained with Cu-poor and Zn-rich compositions [24], [92], [93], in order to limit the formation of detrimental secondary phases and to avoid some defects in the Kesterite. Secondary phases avoided are Cu_xSe, which creates shunts in solar cells because of its high conductivity [29], and Cu_2SnSe_3 which is reported to reduce their open circuit voltage [37], [94]. Thus, the ZnSe secondary phase is kept as the least harmful phase. It is reported to act as an insulator between the surface of the absorber and the CdS/ZnO/transparent conductive oxide, and reduces the short circuit current of the solar cells [45]. Having a Cu-poor and Zn-rich composition can as well promote the formation of V_{Cu} which is the most likely defect generating the p-type conductivity of the Kesterite. This composition also decreases the density of defects such as the anti-site Cu_{Zn} deep acceptor defect [34] or the deep donor defect Sn_{Zn} which can act as a recombination center [23].

In this range of optimal composition, ZnSe is the main secondary phase present. A study by Watjen et al. [45] shows on a single sample that the presence of ZnSe on the surface of the thin films causes a local decrease of the short circuit current collected. However, no investigation of the optimal ratio of ZnSe present in the films is available in the literature. An investigation of the optimal composition to reach highest values of power conversion efficiency, FF, V_{oc} and J_{sc} was presented by Fairbrother et al. [92], however the system is very different from that presented in this thesis, since no tin self-regulation mechanism is occurring in their case.

5.1.2 Objectives and structure of the chapter

In this chapter 5, the first objective is to understand more deeply the role of ZnSe on the short circuit current of the solar cells. Thus, solar cells with different compositions are investigated (same samples as in section 4.3 where the tin self-regulation mechanism was described). Knowing from Watjen [45] that surface ZnSe has a blocking effect on the short circuit current of the solar cells, it is hypothesized that there should be an optimal value of ratio of ZnSe for achieving high short circuit currents: decreasing ZnSe reduces the problem of current blocking, but then the composition should reach a point where other secondary phases should arise, due to local inhomogeneities of metals in the precursors. These other phases, such as Cu_2Se, being more harmful than ZnSe should then decrease the solar cells power conversion efficiencies. Investigating this is one objective of this chapter, and this investigation will be compared with the work by Fairbrother et al. [92] who studied as well the effect of a change of composition of the material on the characteristics of the solar cells, but in a different system where self-regulation of tin does not occur.

The following section (5.3) investigates the origin of low shunt resistances in the devices which was often observed during the work done for this thesis. They significantly affect the performance of the solar cells. Mini solar cells of 0.3x0.3 cm^2 are prepared on the full samples, in order to obtain a mapping of the cells parameters over their total area. It is shown that the probable origin of low shunt resistances is the formation of fragile blisters in the layers, which then cause short shunting paths from the CdS layer directly to the Mo back contact. Finally, section 5.4 describes a study of the effects of a prealloying step prior to selenization, used as an answer to reduce shunt paths in the solar cells. The effect of the duration of this additional step on the open circuit voltage is presented.

In this chapter, a new way of quantifying the composition of the samples is proposed, based on the findings of the previous chapter. As shown in section 4.3, a self-regulation of tin content occurs during the selenization of the samples (Cu/Sn=2 after selenization). If this Cu/Sn self-regulation is assumed, the system becomes one-dimentional, and is fully determined by the ratio of ZnSe/(ZnSe + Kesterite). Thus, in addition to the ratios usually reported, namely Cu/(Zn+Sn) and Zn/Sn, two new ratios would be introduced to describe the system, which seem to be more representative.

The system is assumed to be Cu-poor, and in the conditions of Cu/Sn self-regulation. Thus Cu is the limiting factor for the formation of Kesterite, and the quantity of Kesterite will be at maximum equal to the initial quantity of Cu/2. By assuming a complete conversion of Cu to Kesterite, the following occurs:

Ratio 1: $\frac{Zn-\frac{Cu}{2}}{Zn}$

Ratio 1 represents the molar fraction of ZnSe in the binary system (Kesterite + ZnSe):

$$\frac{ZnSe}{CZTSe+ZnSe} = \frac{Zn-\frac{Cu}{2}}{Zn}.$$

Ratio 2: $\frac{Sn-\frac{Cu}{2}}{Sn}$

Ratio 2 represents the percentage of tin which will be lost.

With this notation a precursor sample is defined by i) ratio 1 which quantifies the expected molar fraction of ZnSe and by ii) ratio 2 which predicts what percentage of the initial tin will be lost during the selenization.

5.2 Effects of composition

5.2.1 Experimental details and objectives

For the purpose of the study presented in this section, Cu/Sn/Zn precursors were electrodeposited with different thicknesses of Cu, Sn and Zn layers, in order to vary the stoichiometry of the metallic stack, while maintaining a constant total thickness of the complete stack. Results on these samples were already presented in section 4.3, to demonstrate the self-regulation mechanism of Cu/Sn in the Cu-poor and Zn-rich domain of compositions. The absorbers were implemented into solar cell devices, and the results will be presented in the next sections: 5.2.2 offers a global view of the compositions by investigation a wide range of stoichiometries, including Cu-rich and Cu-poor samples and the resulting efficiencies. Section 5.2.3 presents in details the Cu-poor and Zn-rich region of compositions, and the effects of Zn content on the short circuit current of the solar cells. Finally, 5.2.4 presents the evolution of the two other characteristics of the solar cells studied here, namely the open circuit voltage and the fill factor. In this section, only results from solar cells made in the central part of the samples are presented, in order to stay in the homogeneous composition zone, as shown in figure 5.1. The two cells considered for each sample in section 5.2 are thus in the area where the zinc content varies by less than 5%.

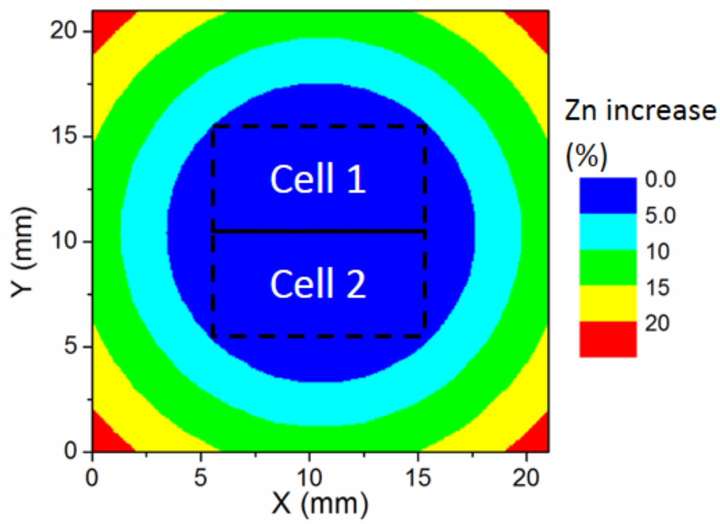

Figure 5.1: Position of two central cells on the map of zinc thickness increase (map from figure 3.4b). The positions are indicated by the black dashed lines.

5.2.2 Global view of composition changes

The first study of composition is done with a wide range of stoichiometries, as shown in figure 5.2a. This was already presented in section 4.3, and shows that most of the compositions are near-invariant after selenization, except for samples prepared in the Cu-poor and zinc rich area, where tin regulation occurs, via evaporation and absorption of Snse during the process, and results in a constant ratio of Cu/Sn=2. Solar cells were prepared with these samples and the corresponding efficiencies are shown in figure 5.2b.

The results obtained here confirm what is reported in the literature: all solar cells for which the ratio Cu/Zn is over or equal to two have very low efficiencies. Only cells grown with a ratio Cu/Zn of less than two are working, and the best efficiency is obtained with a ratio of Cu/(Zn+Sn)=0.71 and Zn/Sn=1.31 before selenization. Reasons for low efficiencies in the Cu/Zn>=2 region are most probably the presence of Cu_xSe which creates shunts in solar cells [29], and Cu_2SnSe_3 which is reported to reduce their open circuit voltage [37], [94]. Thus, Cu-poor compositions have to be used in order to avoid any of these harmful secondary phases.

Attention was then concentrated on understanding the effects of the presence of ZnSe, which is the predominant secondary phase in the cells that are studied in this thesis. A specific study of the influence of zinc ratio is presented in the following.

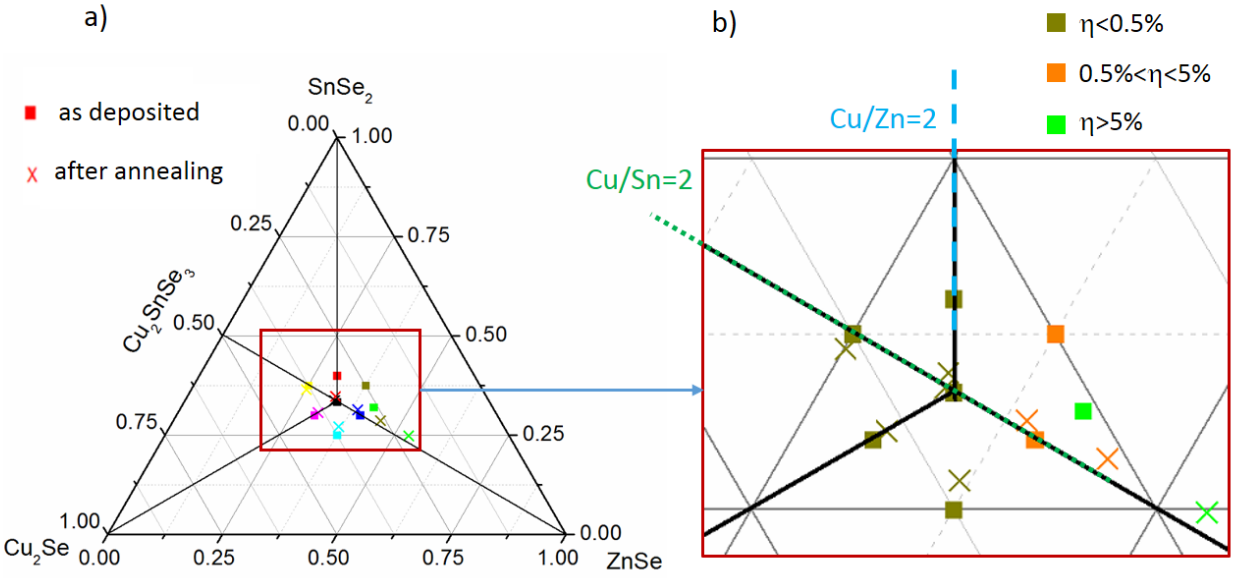

Figure 5.2: (a) Composition of Cu-Sn-Zn samples as deposited (squares), and after selenization (crosses) at 550°C for 30 min with Se and SnSe, plot on the usual Cu_2-Sn-Zn ternary diagram. Each color corresponds to a single sample (5.2a is a reproduction of figure 4.13a for convenience). (b) zoom of figure 5.2a, with a change of color coding representing the efficiencies (η) of the solar cells. The blue dashed line and the green dotted line represent respectively the compositions for which Cu/Zn=2 and Cu/Sn=2.

5.2.3 Current blocking behavior of ZnSe

Here, similarly as in section 5.2.2, the samples presented in section 4.3 were implemented into solar cells, and the effect of composition change on their characteristics is discussed. As a reminder, two series of samples are prepared, one has Zn/Sn=1.27, the other Zn/Sn=1.18, and each series contains four different values of Cu/(Zn+Sn): 0.51, 0.61, 0.71 and 0.81. In section 4.3, it was shown that the regulation of tin content in the absorbers during selenization via gas phase exchange of SnSe resulted in the presence of mostly two phases: Kesterite and ZnSe. The objective of this section is to understand the effect of ZnSe, by studying solar cells made with different ratios of ZnSe. As a reminder of the results presented in section 4.3, figure 5.3a shows the evolution of composition after selenization for the eight samples prepared for this study.

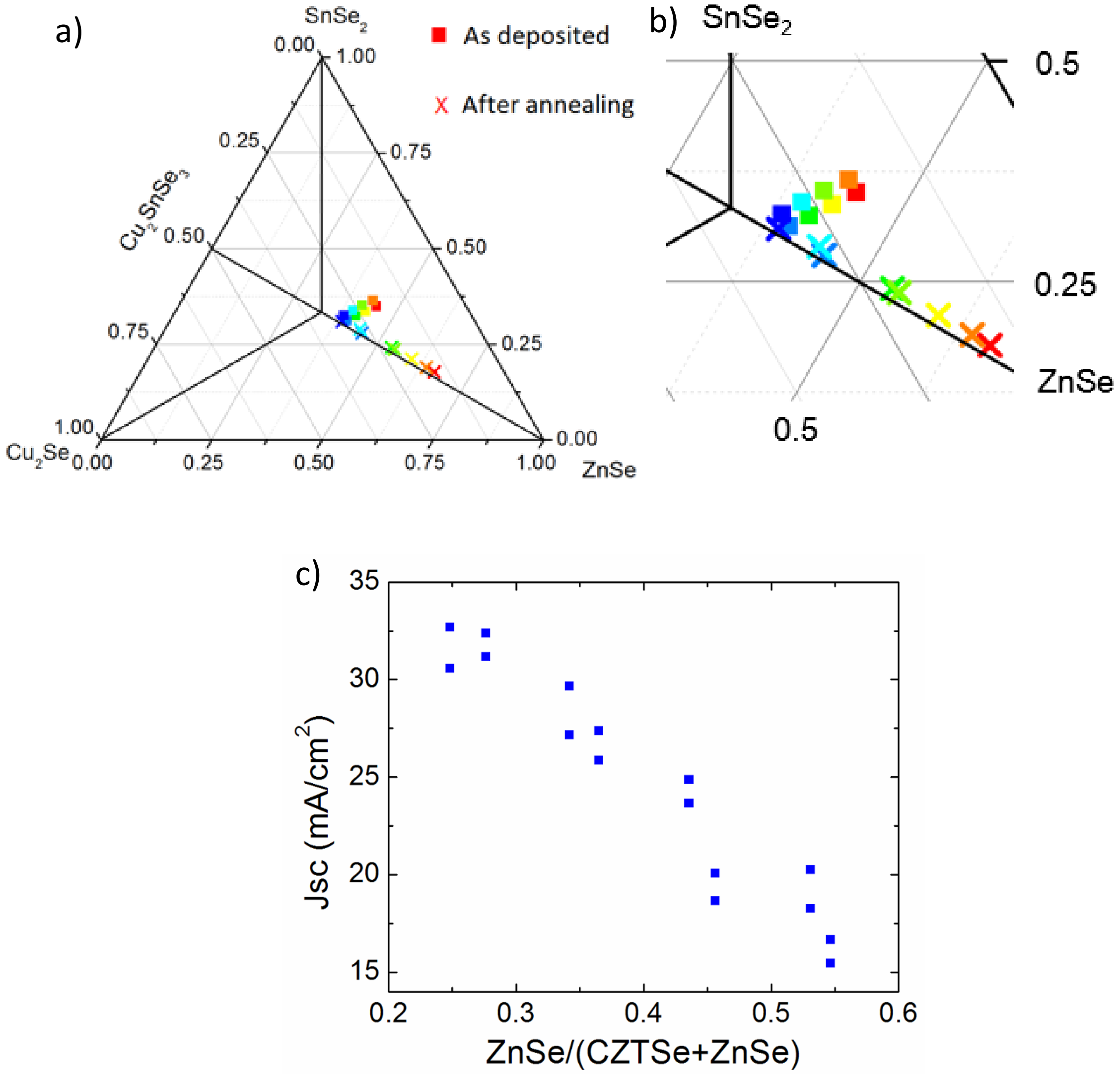

Figure 5.3: (a) Composition of Cu-Sn-Zn samples as deposited (squares), and after selenization (crosses) at 550°C for 30 min with Se and SnSe, plot on the usual Cu_2-Sn-Zn ternary diagram. Each color corresponds to a single sample. (b) zoom of the central part of the ternary diagram 5.3a. 5.3a and 5.3b are reproductions of figure 4.14, for convenience. (c) evolution of ratio ZnSe/(ZnSe + CZTSe) as a function of ratio of ZnSe. For each sample, the values of the two cells made in the center are displayed.

The self-regulation of Cu/Sn ratio is clearly visible: after selenization, all compositions lie on the axis CZTSe-ZnSe (axis of iso Cu/Sn=2). This results in samples containing mainly Kesterite, and ZnSe at different ratios. The evolution of J_{sc} of the corresponding solar cells is presented in figure 5.3c. Again, here only solar cells in the center of the samples are shown. A strong relationship between the short circuit current and the ZnSe ratio is revealed here: J_{sc} is linearly decreasing as a function of ZnSe ratio. This result is very interesting and goes further than the study of Watjen et al. [45], where the blocking current effect of ZnSe is demonstrated, but only on a single sample by comparing areas covered by ZnSe, and others not. In the case of the present study, samples with a higher zinc content result in selenized samples with higher amount of ZnSe. It was shown in the previous chapter 4 that ZnSe mainly segregates at the surface of the samples, thus the coverage of the absorber by ZnSe is higher when the ZnSe ratio increases. This consequently increases the insulated areas between absorber and CdS/ZnO/transparent conductive oxide. These results were published in [95].

Complementary analyses were performed on these samples, in order to get a more comprehensive view of the effects of ZnSe at the surface of the absorbers. EQE spectra of four samples of the series Zn/Sn=1.17 are presented in figure 5.4, to study the losses of current as a function of the wavelength of incoming light. This figure 5.4 shows a general decrease of the whole spectrum, independent of the wavelength, as the ZnSe molar ratio is increased.

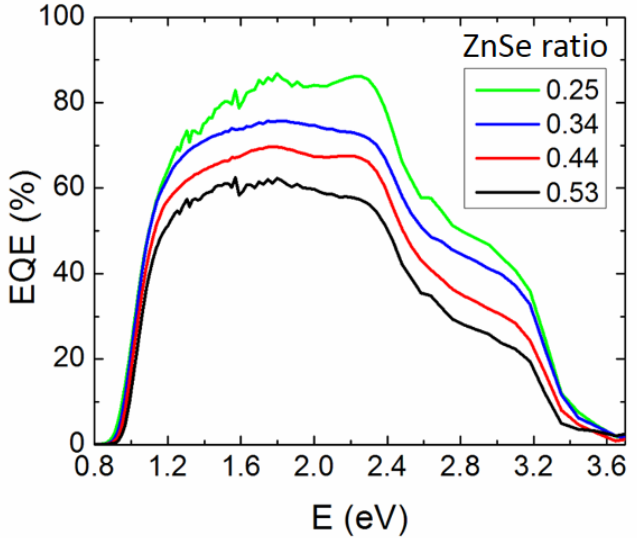

Figure 5.4: EQE spectra of devices obtained from absorbers with ZnSe mole fractions of 0.25, 0.34, 0.43 and 0.53.

The observations of modifications in EQE spectra that were made can be explained by considering the schematic cross section of a solar cell half covered with ZnSe, in figure 5.5. Because of the resistivity of ZnSe (because of its high bandgap), electrons generated in the absorber underneath the ZnSe cannot be collected by the transparent conductive oxide. Thus, all the light absorbed in zone 1 (see figure 5.5) will be lost. This phenomenon is independent of the wavelength of the incoming photon, and corresponds to the large current losses observed in figure 5.4. This was as well published in [95].

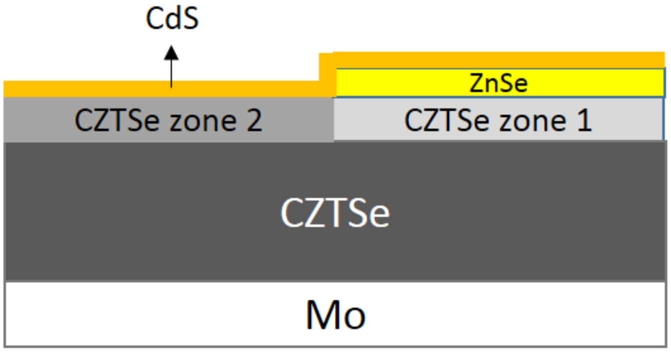

Figure 5.5: Schematic cross section of solar cell device, with partial surface ZnSe coverage.

As a conclusion, it was shown in this section that there is a linear relationship between the short circuit current of the solar cells and the ratio of ZnSe in the absorbers, due to the insulating effect of this phase. The next section presents the evolution of the other cells parameters (V_{oc} and FF) of the same solar cells than that shown in the present paragraph.

5.2.4 Variation of other cells parameters

As mentioned before, the very same solar cells than in the latter section 5.2.3 are presented here, which consist of two sets of four solar cells: one has a precursor composition Zn/Sn=1.27, the other Zn/Sn=1.18, and each series contains four different values of Cu/(Zn+Sn): 0.51, 0.61, 0.71 and 0.81. In this new section, the evolutions of open circuit voltage and fill factor are studied.

A first overview is given by figure 5.6. There is a quite strong scattering of the values of both V_{oc} and FF (figure 5.6a), which cannot be correlated to values of ratio of ZnSe. These changes are relatively higher than the changes of J_{sc}, and consequently the efficiencies of the solar cells also have a very scattered behavior, which is not correlated to the changes of composition (figure 5.6b).

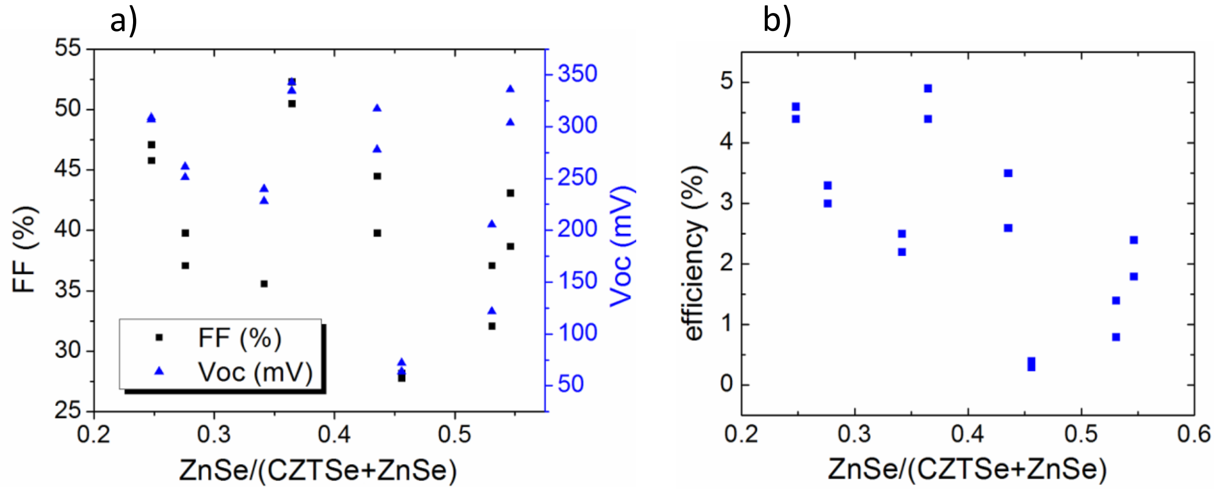

Figure 5.6: Evolutions of (a) open circuit voltage and fill factor and (b) device efficiency as a function of ZnSe ratio. For each sample, the values of the two central cells are displayed on each graph.

Further analyses of these solar cells are done, by fitting the IV curves of each solar cell, and extracting the values of series resistance and shunt resistance. This allows to find an underlying relationship between the shunt resistance of the solar cells and the V_{oc}, as described in figure 5.7: there is a relatively strong correlation between the increase of shunt resistance and the open circuit voltage of the solar cells.

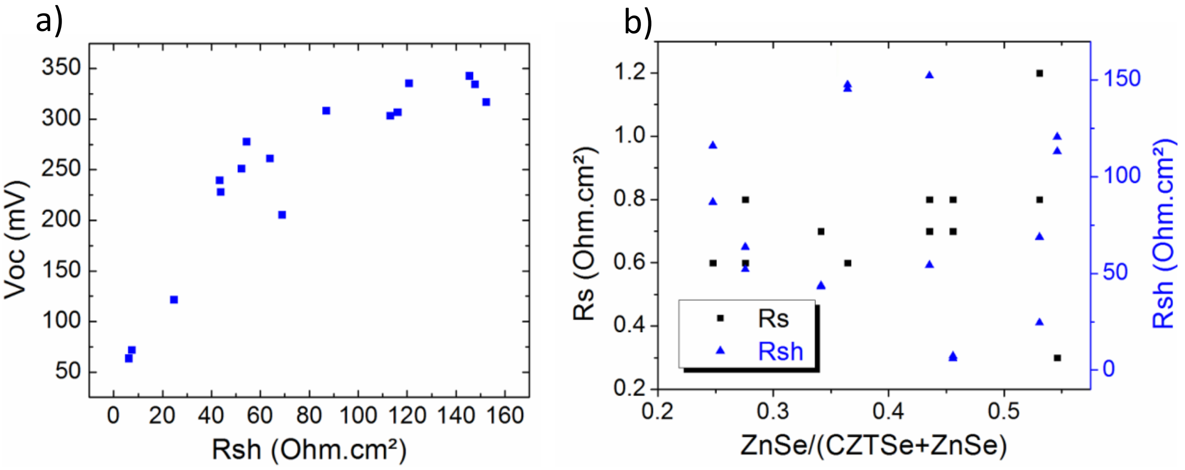

Figure 5.7: (a) Evolution of the V_{oc} of the center cells of all samples as a function of their shunt resistance. (b) scattering of shunt and series resistance measured under illumination for different values of ZnSe ratios.

As shown in figure 5.7a, the main drawback for the open circuit voltage of the solar cells seems to be the too low shunt resistances of some solar cells. Figure 5.7b shows no correlation between values of R_{sh} and ratio of ZnSe. Values of series resistance are all staying reasonably low and are not harmful in this case for the cells performances.

Figure 5.8 shows as an example the current voltage (JV) curves of two solar cells, the best cell obtained for the study, together with a cell obtained with a sample which has a close value of ZnSe ratio (0.34 vs 0.36), but with a much lower efficiency. Clearly, an important loss of efficiency is due to the higher slope of the curve at low values of voltage, which is characteristic of a higher R_{sh} (see the introduction of this chapter).

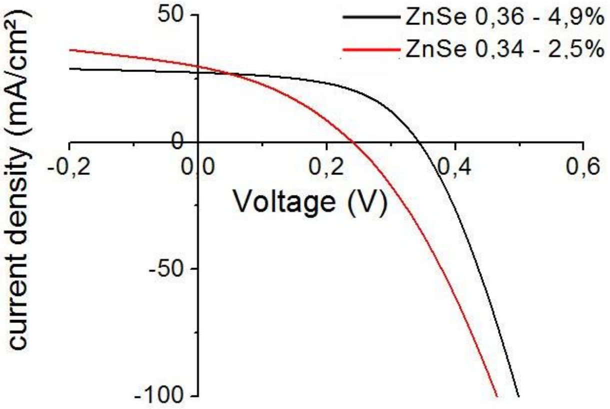

Figure 5.8: IV curves of samples with ZnSe ratio of 0.36 (black curve, 4.9% efficiency), and ZnSe ratio of 0.34 (red curve, 2.5%).

Thus, large changes of V_{oc} and FF are observed between different samples, with no relation with the change of composition, and these changes are correlated to strong changes of shunt resistances. These changes of shunt resistance will be investigated further in the next section (5.3).

5.2.5 Summary

As was described in this section, the change of ZnSe content in the layers affects the short circuit current strongly: ZnSe segregates on the surface of the films and creates a current blocking barrier, by shading the Kesterite absorber. The more ZnSe is present on the surface, the higher is the surface covered, and thus the lower the current. It was also demonstrated that the cells can often suffer from low shunt resistances, which decreases the V_{oc} and fill factor. The causes of these low R_{sh} are not yet explained in this section, and will be investigated in the next section.

As a summary, the perspective is enlarged to all the solar cells which were prepared in the central homogeneous area of a sample. These cells include several rounds of cells that were made identically to the ones that are presented in this section, except for the selenization (some samples are selenized alone in the graphite box, whereas two samples are selenized together for a standard process, and one sample is selenized with more selenium). For all these cells, the relationships found in this section were tested, with no consideration about the changes of process parameters, to study the potential universality of these phenomena. Figure 5.9 presents the data of all solar cells built in the homogeneous central area of the samples. These cells have all a Cu-poor and Zn-rich stoichiometry.

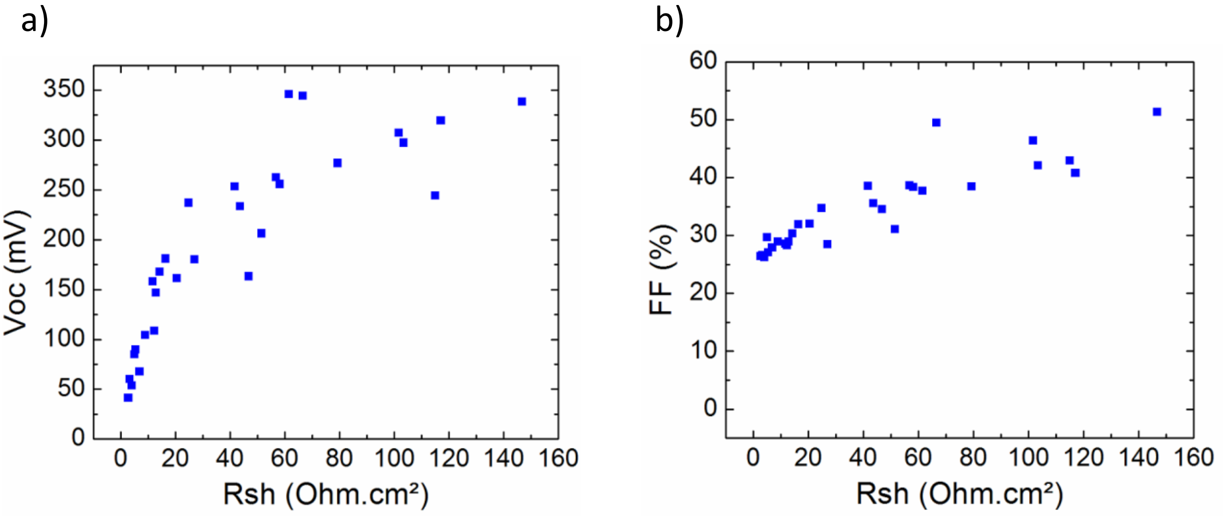

Figure 5.9: Evolution of (a) the average V_{oc} and (b) the average fill factor as a function of the average shunt resistance of cells in the center of samples. Averages are calculated for the two central cells of each sample.

The first relationship tested is the evolution of shunt resistance, which seems to be the strongest parameter influencing the cells efficiencies. Figure 5.9 shows the evolution of V_{oc} and FF for all cells, and apparently the observation made is holding here. Above R_{sh} values of about 100 Ohm.cm², decent open circuit voltages of about 300 mV and fill factors of about 40-50% are quasi-guaranteed. This strengthens the idea that shunt paths could be a main problem for the solar cells prepared via the process studied for this thesis.

Similarly, two other sets of samples were prepared with different precursor compositions. The results of these two new sets of samples are presented in figure 5.10a together with the results previously shown. Here, low values of ZnSe ratios are investigated in order to detect the optimal value of this ratio. A value where J_{sc} is maximum is found around 0.2 ZnSe/(ZnSe+CZTSe). Jsc attains values of 35-40 mA/cm² at this ZnSe ratio. As explained previously, the decrease of Jsc at values of Znse ratio lower than 0.2 can be due to multiple reasons: formation of other types of secondary phases such as Cu_2Se or Cu_2SnSe_3, formation of detrimental defects in the Kesterite, or alteration of the p-type behavior of Kesterite, due to the lower presence of V_{Cu} defects.

This can be compared with the study of Fairbrother et al. [92] who investigated the effect of the composition of the absorber for a wide variation of compositions, as shown in figure 5.10b. the compositions represented on their graph are compositions after selenization, and it can be clearly seen that in their case no self-regulation of tin is observed. If it was the case, all compositions should lie on the red line of figure 5.10b (ZnSe line). This is probably due to the different process investigated in the study of Fairbrother: the Cu-Sn-Zn precursors are cosputtered, thus all metals are intimately mixed in the films. This probably allows to decrease the evaporation of tin, which probably occurs strongly in the process described for this thesis because of the presence of large segregation areas containing free tin, as described previously. Nevertheless, the study of Fairbrother et al. shows that optimum values of J_{sc} is obtained for a range of composition values from (Cu/Zn=1.1; Cu/Sn=1.4) to (Cu/Zn=1.6; Cu/Sn=1.8).

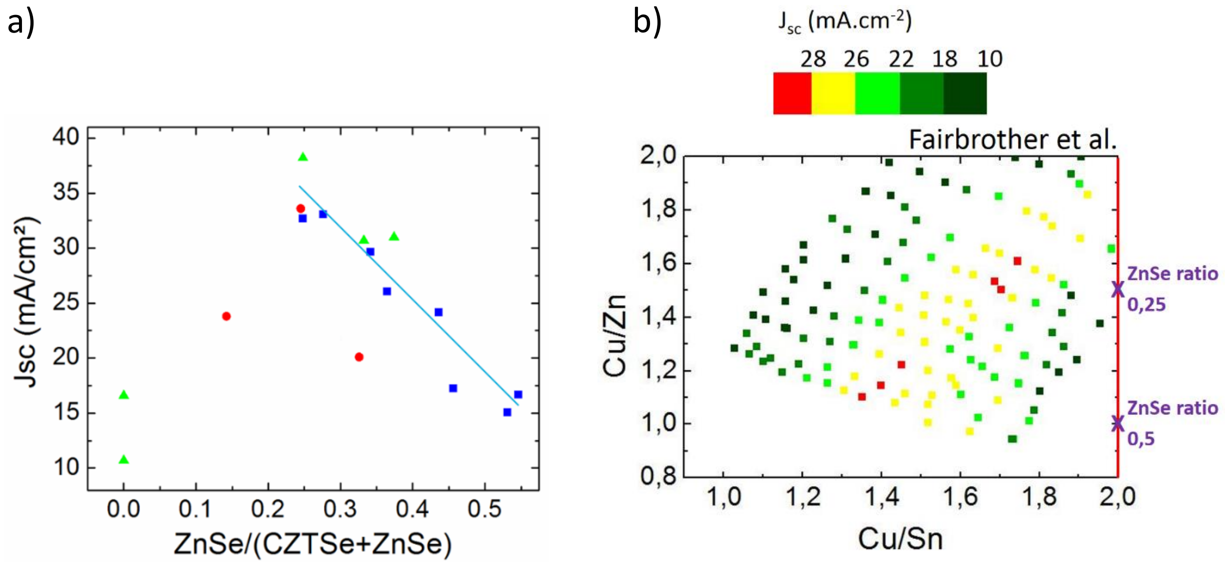

Figure 5.10: a) Evolution of average J_{sc} with ratio of ZnSe for cells from the study of section 5.2.3 (in blue) together with data from two other sets of solar cells (in green and red). The solar cells are made in the center of the samples (each point of the graph is the average of the short circuit current of the two central cells of a sample). b) data extracted from [92] **and re-plotted, showing the dependence of J_{sc} on the composition of the CZTSe absorber. The values of ZnSe/(CZTSe+ZnSe) of 0.5 and 0.25 (with Cu/Sn=2) are plotted on the graph, in order to aid the comparison with figure 5.10a.**

Thus, the conclusion of these investigations is that very reproducible values of short circuit currents are obtained, which are directly influenced by the molar ratio of ZnSe. An optimal value of molar ratio of ZnSe is found at 0.2, which allows the achievement of short circuit currents of about 35 mA/cm². V_{oc} and FF are varying between a sample to another because of significant variations of R_{sh} between samples, which causes are not yet understood, and are the subject of the next section.

5.3 Evolution of shunt resistance

5.3.1 Changes of shunt resistance within samples

In order to explain the low values of shunt resistances in the solar cells, a natural hypothesis is the presence of shunt paths through the absorber, which could be due to pinholes, or to conductive phases present in the layers. However, since very Cu-poor compositions are used, only ZnSe and Kesterite are expected, the second hypothesis seems to have a low probability to be true. Thus it was decided first to compare several samples with very different efficiencies, and find if pinholes can be observed. An analysis of optical microscope images of absorbers before cell finishing is done, with the objective to find morphological features which could be or lead to pinholes. A good candidate was found by comparing two solar cells from a same batch, with extreme differences of efficiencies.

Figure 5.11 shows the surface of absorbers which give good (5.11a) and very low (5.11b) efficiencies. On image 5.11b many darker dots can clearly be seen. An analysis of a different sample at different focus distances (figures 5.11c and 5.11d) show that the dots observed are protruding features, referred to as "blisters" in this chapter. Their height on the sample considered here is of about 6 micometers, compared to the surface of the sample. By comparing other samples, it appears that most of the samples which present these dots on the surface give then poor device efficiencies. These blisters appear to be very fragile, and thus easily a formation of pinholes is observed from these blisters, as shown in the following.

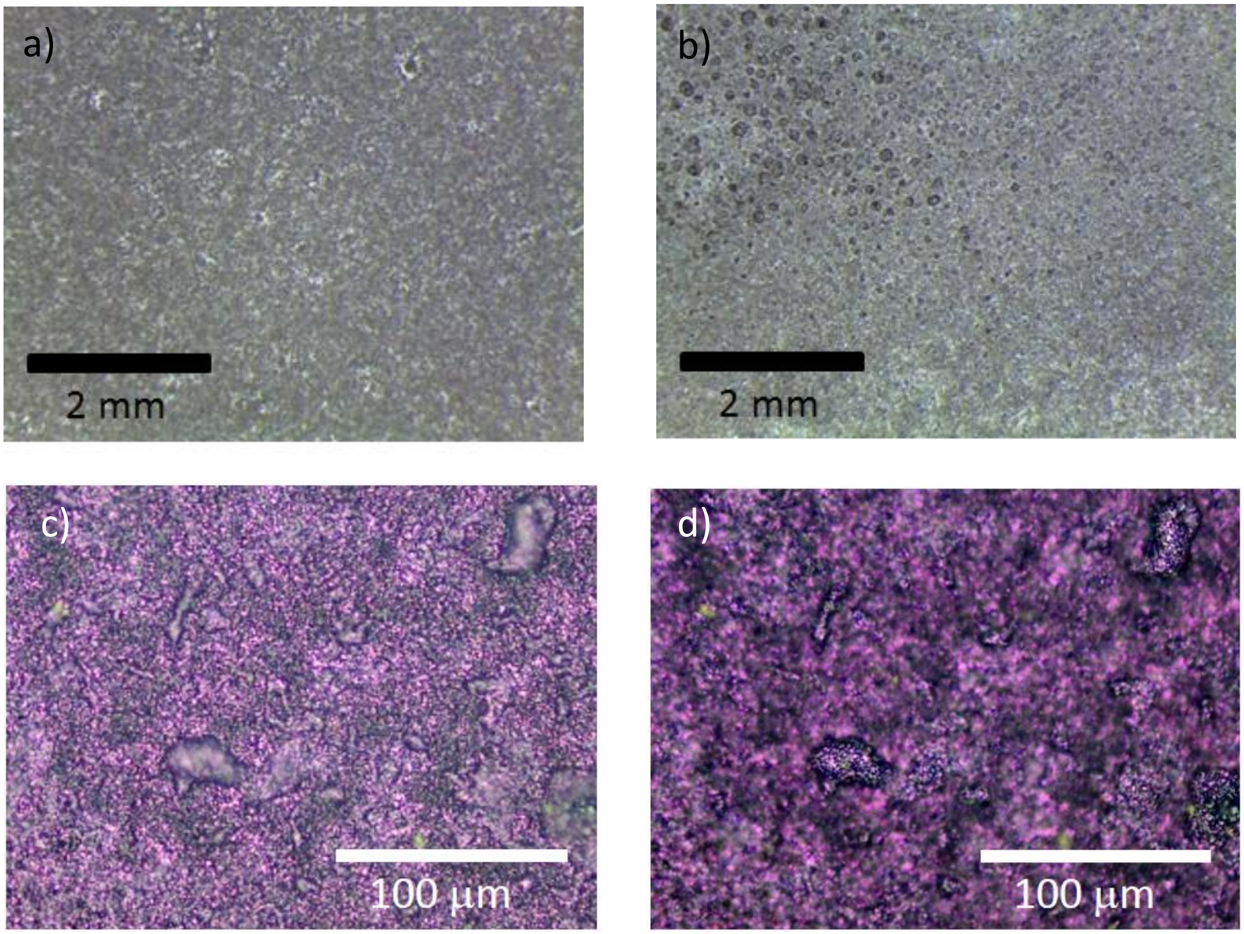

Figure 5.11: Optical microscope images of absorber layer surfaces. After cell completion the cells reach power conversion efficiencies of (a) 5.3% and (b) 0%. (c) and (d) are images of a different absorber. 5.11c is focused on the layer, and 5.11d is focused on the surface of the blisters. The focus difference is 6 micrometers.

A test is realized to assess the possibility of formation of pinholes from the blisters which are on the surface of an absorber layer, and is shown in figure 5.12. After simply a gentle touch (compressive stress) of the surface at the position where the blisters are seen, the material breaks and delaminates, leaving bare Mo, which thus may be a source of shunting in the solar cells. A further indication that these blisters are probably harmful for the devices is the study of optical microscope images of all absorbers which gave solar cells of efficiencies above 5.5%, presented in appendix B. On none of the images these blisters are seen.

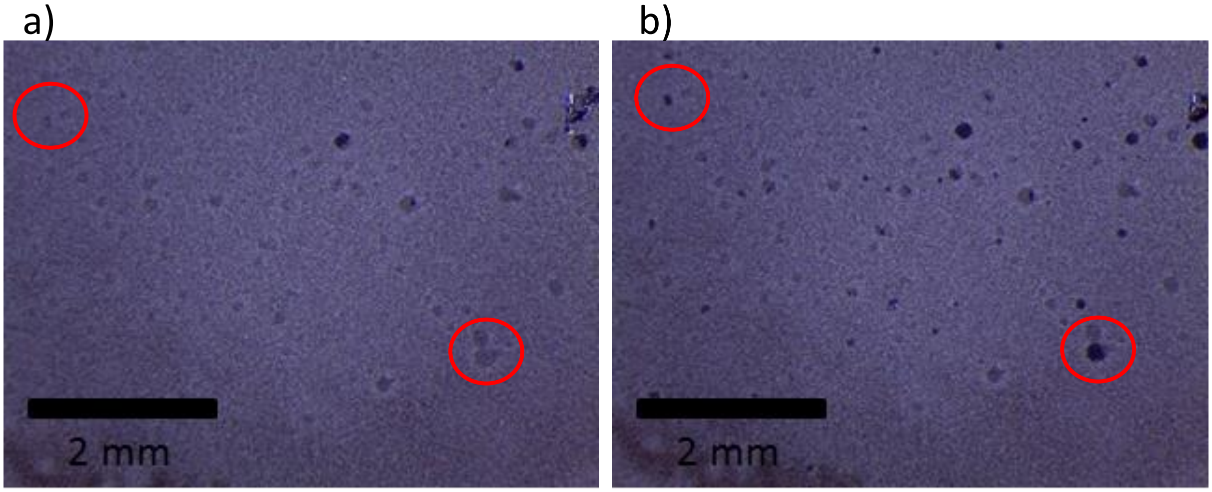

Figure 5.12: Absorber layer with blisters (a) before, and (b) after a gentle touch of the surface. A few pinholes are already present in image 5.12a, and more pinholes appear after applying mechanical compressive stress (touching) on the surface. The new pinholes appear at positions of former blisters (the red circles on the images highlight some of them).

From this observation, selection rules were implemented to avoid making solar cells with any sample which contains blisters. Thus before cell completion, all absorbers were analysed with optical microscope, and samples containing blisters were discarded. An improvement of the reproducibility was then observed, with much less variation of V_{oc} and FF than for example in the case of the composition study that was presented in section 5.2. Further information on the pinholing effect will be shown in the next section, where four samples are analysed on the complete 2x2 cm^2 area by making mini solar cells of 0.1 cm^2 to provide a mapping of solar cells efficiencies. This next study shows especially that blisters can be much smaller than those observed in the present paragraph (50-100 micrometers values of diameter for the larger blisters will be presented). A better reproducibility of the process is also visible.

5.3.2 Solar cells mapping

This section presents a study of a series of four samples (A, B, C and D), which all passed the “blister test” successfully. They were prepared identically, except for sample A. This sample was already used for normal 0.5x1 cm^2 solar cells, and after measurement of the efficiency, the CdS/ZnO/contacts were etched with 10% HCl for one minute. The absorber was then reused in the study presented now, and

CdS/ZnO/grids were deposited in the same batch as samples B, C and D. For each sample, small solar cells of 0.33x0.33 cm² were built on the complete absorber area (around 2.1x2.1 cm²), in order to obtain a mapping of cells parameters over the complete samples area. The 0.1 cm² solar cells were scribed and measured at IRDEP (Institut de Recherche et Developpement sur l Energie Photovoltaique, Chatou, France). The precursor compositions are Cu/(Zn+Sn)=0.8 and Zn/Sn=1.2. This corresponds to a ZnSe/(CZTSe+ZnSe) ratio of 0.2, which is the optimal value for obtaining high J_{sc}, as presented in section 5.2.

Figure 5.13 shows optical microscope images of the four absorbers, before deposition of CdS, ZnO and contact grids. No blister can be observed on any of these samples, and optically the surface appears to be homogeneous. The solar cells are presented in the following figure 5.14.

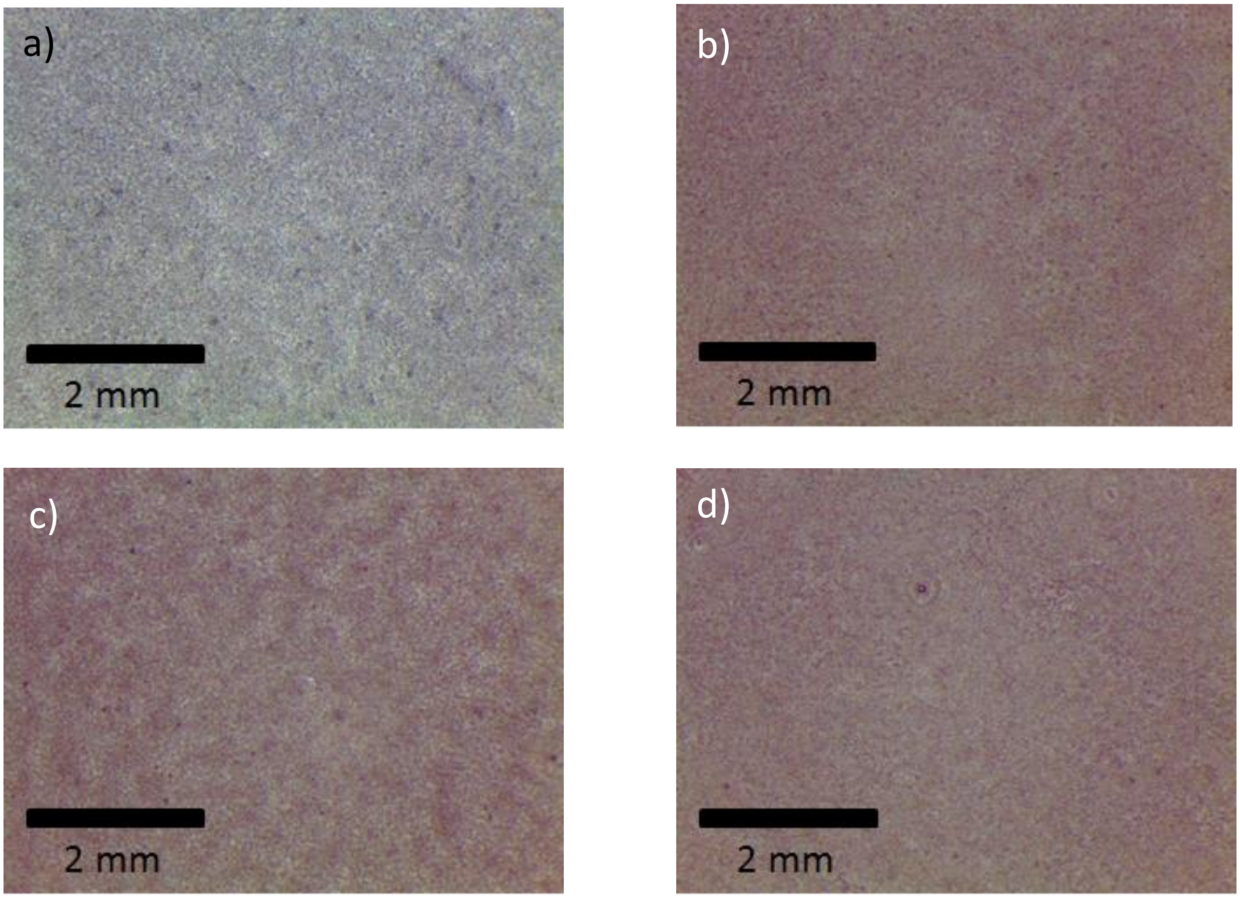

Figure 5.13: (a), (b), (c) and (d) are optical microscope images of the surface of the absorbers of samples A, B, C and D respectively, prior to deposition of CdS.

The solar cell devices efficiencies are shown in figure 5.14, together with the pictures of some of the samples with the solar cells scribed. As one can see, in this case metallic grids are not used, because of the small size of the solar cells, and electrical contact is made directly on the TCO surface for IV measurements. All efficiencies measured are displayed on the maps of figure 5.14. The first observation is that all samples reach similar efficiencies, with best values of around 5.5% for all of them. This is an indication that the process is more reproducible, probably thanks to the exclusion of blister-containing absorbers. Then, a general observation from these efficiency maps is that the highest values are obtained in the edges of the samples for most of them, namely B, C and D. Sample A is very homogeneous laterally. Variations of cells parameters are thus investigated in order to understand the origin of the differences of efficiency.

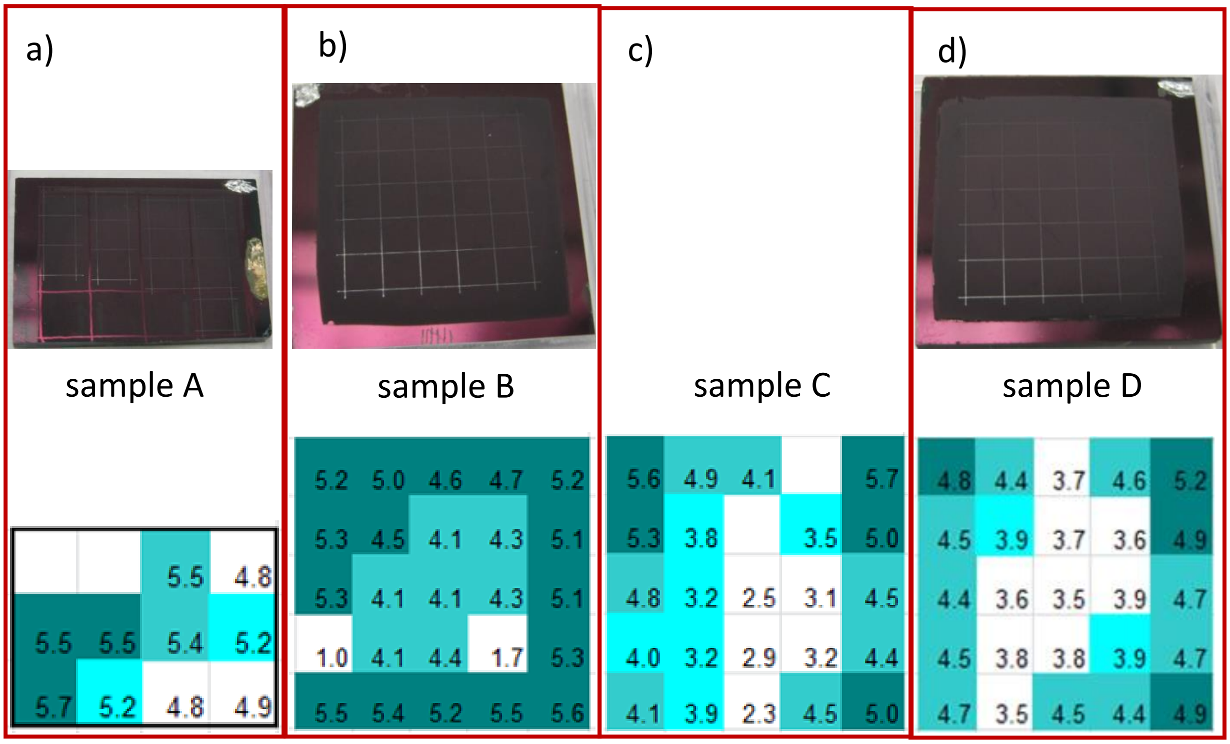

sample A

		5.5	4.8
5.5	5.5	5.4	5.2
5.7	5.2	4.8	4.9

sample B

5.2	5.0	4.6	4.7	5.2
5.3	4.5	4.1	4.3	5.1
5.3	4.1	4.1	4.3	5.1
1.0	4.1	4.4	1.7	5.3
5.5	5.4	5.2	5.5	5.6

sample C

5.6	4.9	4.1		5.7
5.3	3.8		3.5	5.0
4.8	3.2	2.5	3.1	4.5
4.0	3.2	2.9	3.2	4.4
4.1	3.9	2.3	4.5	5.0

sample D

4.8	4.4	3.7	4.6	5.2
4.5	3.9	3.7	3.6	4.9
4.4	3.6	3.5	3.9	4.7
4.5	3.8	3.8	3.9	4.7
4.7	3.5	4.5	4.4	4.9

Figure 5.14: (a), (b), (c) and (d) are digital images and maps of cells power conversion efficiencies of respectively samples A, B, C and D. No picture of sample C is available.

The relationships between efficiency and the three main J-V characteristics are presented in figure 5.15, in order to explain the differences of efficiency observed within samples. Apparently, the changes of efficiency are mainly driven by changes of fill factor and open circuit voltage. The figure 5.15c showing the evolution of efficiency as a function of J_{sc} is much more scattered than the figures 5.15a and 5.15b, where a correlation is clearly seen.

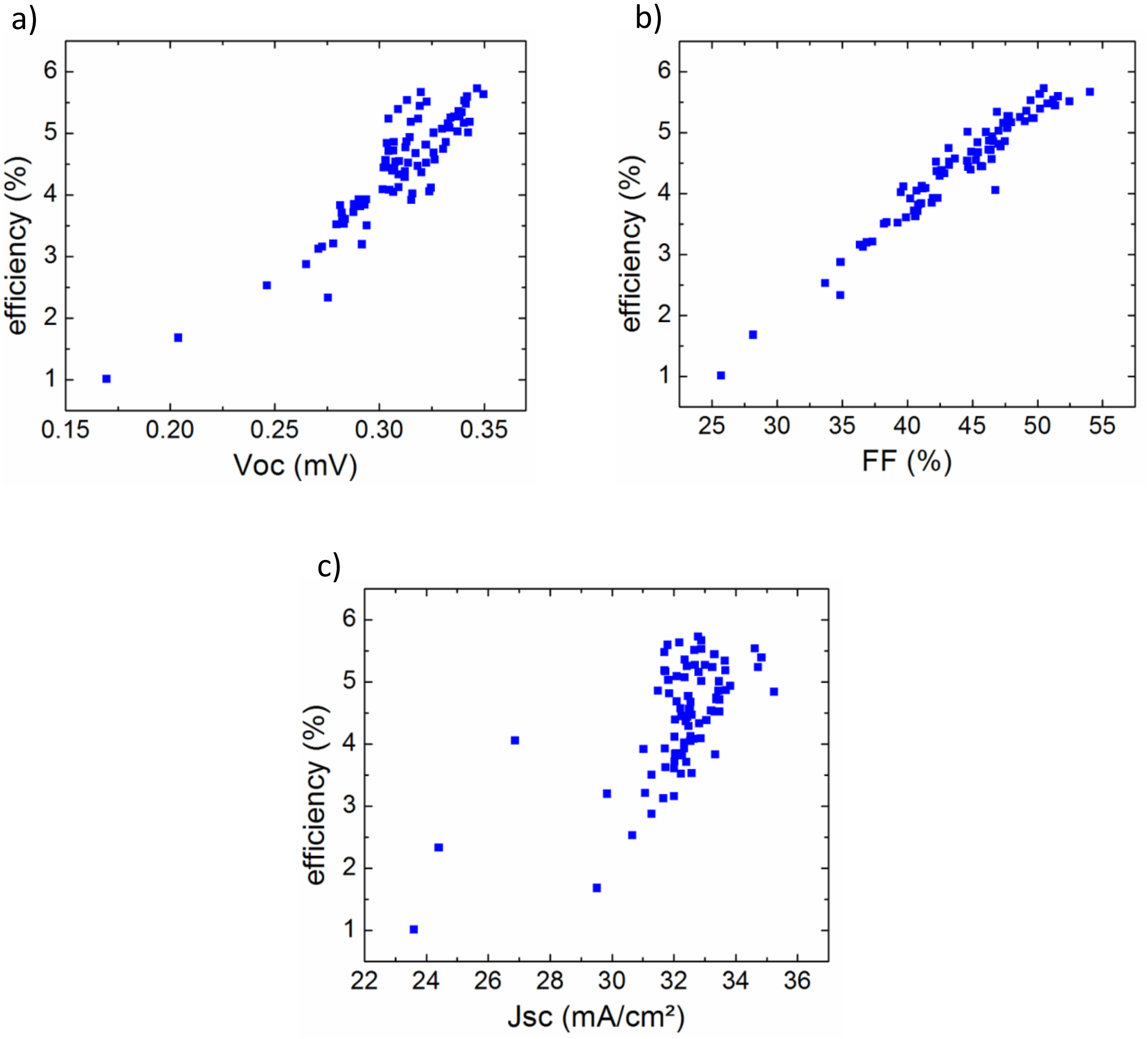

Figure 5.15: Evolution of power conversion efficiency as a function of (a) open circuit voltage, (b) fill factor, and (c) short circuit current. All solar cells made on the four samples A, B, C and D are presented there.

After analysis of the data in figure 5.16, it appears that again the differences of V_{oc} and fill factor are mainly due to variations of shunt resistance. As a consequence, a rather good correlation between the shunt resistance of the devices and the efficiency is found, which is due to the relatively low variation of short circuit current between cells, because of their similar composition. Between the center and the edge of these samples, the ZnSe ratio is expected to vary from 0.21 in the center to 0.33 at the edges, which corresponds to a variation of J_{sc} of about 5 mA/cm², if referred to the figure 5.10. This corresponds to the data of figure 5.16a and will be discussed further in the following. For further analysis, the surface of the samples was analysed with an optical microscope with a higher magnification than previously used, in order to observe the morphology of the samples at different positions, and see if differences can be found between center and edges of samples. The analysis was done on sample D, which has the highest variation between center and edge of the substrate.

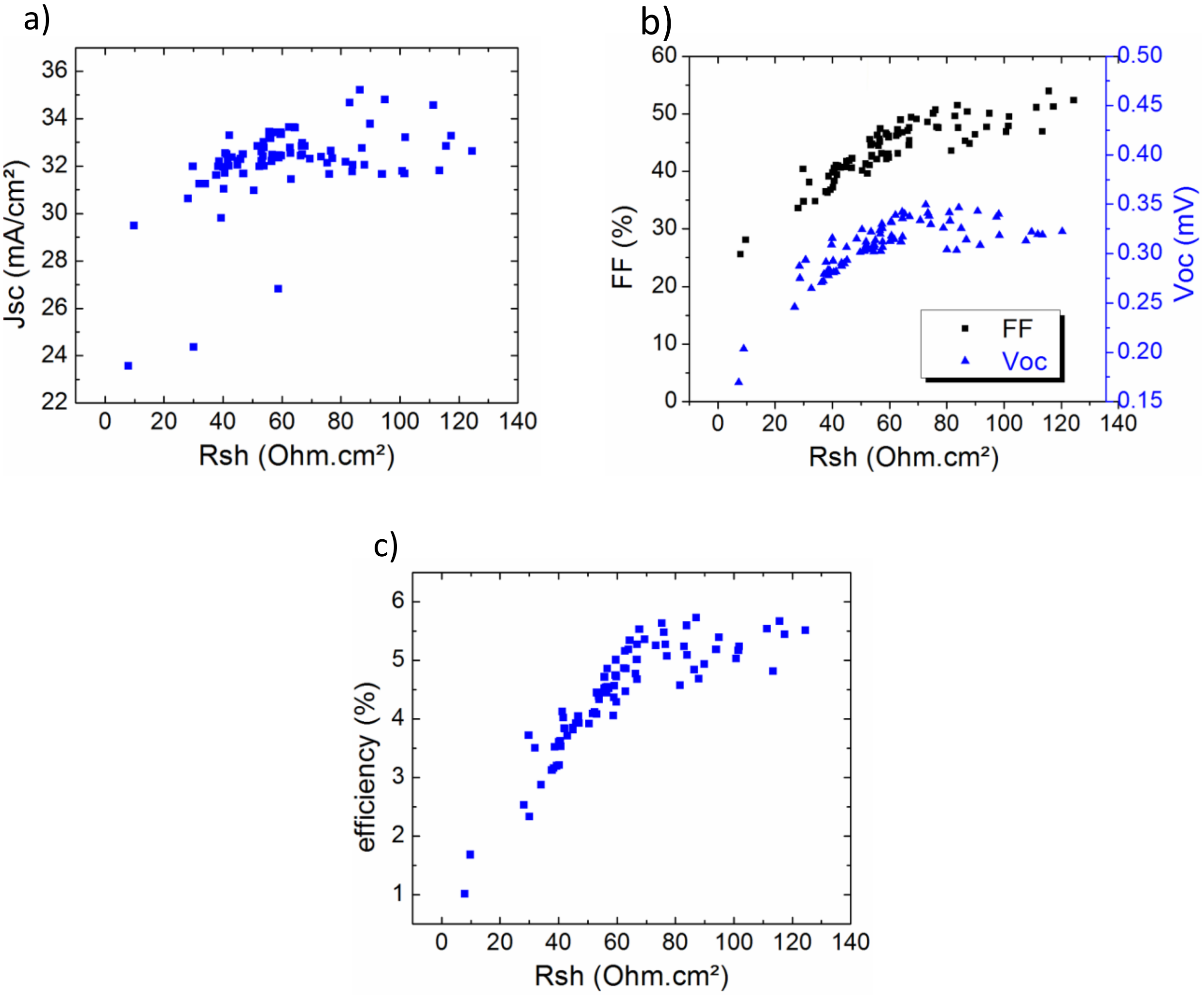

Figure 5.16: (a) Evolution of J_{sc} and (b) evolution of FF and V_{oc} as a function of shunt resistance. (c) evolution of efficiency as a function of shunt resistance. All data from the cells of samples A, B, C and D are displayed in each of these graphs.

For this analysis, an optical microscope with a higher magnification than previously is used. As shown in figure 5.17, 5 cells with a wide variation of power conversion efficiency are chosen from the center to the edge of sample D. These cells are analysed with the optical microscope at two random positions for each solar cell. The results are presented in appendix C. Blisters are detected here again, but at a much smaller scale than previously. And it is obvious that their quantity is decreasing from the center of the samples to their edges. From each of the images, the percentage of the surface covered with blisters is measured by ImageJ analysis. The average value for the two images of each cell is measured, and the results are presented in figure 5.18.

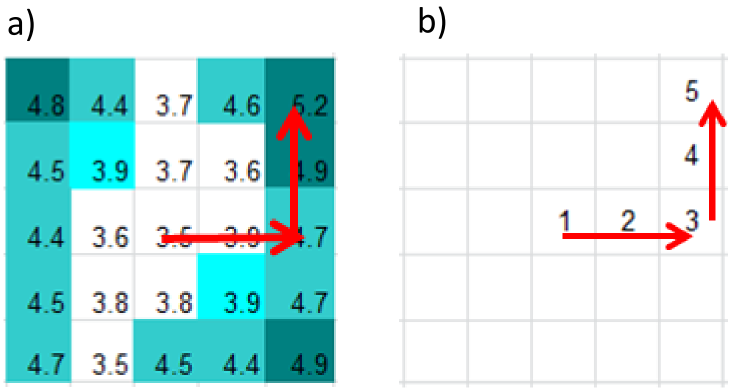

4.8	4.4	3.7	4.6	5.2
4.5	3.9	3.7	3.6	4.9
4.4	3.6	3.5	3.9	4.7
4.5	3.8	3.8	3.9	4.7
4.7	3.5	4.5	4.4	4.9

Figure 5.17: Position of solar cells analysed by optical microscope on sample D: (a) on efficiency map, and (b) name of the solar cells.

Thus, the blistering and pinholing effect is clearly related to the decrease of shunt resistances, as can be seen in figure 5.18. This strengthens the hypothesis that was made at the beginning of this section, which is that most of the losses of fill factor and V_{oc} are due to low shunt resistances, mainly due to pinholing effects. The last parameter which remains to be studied in this series of four samples (A, B, C and D) is the short circuit current.

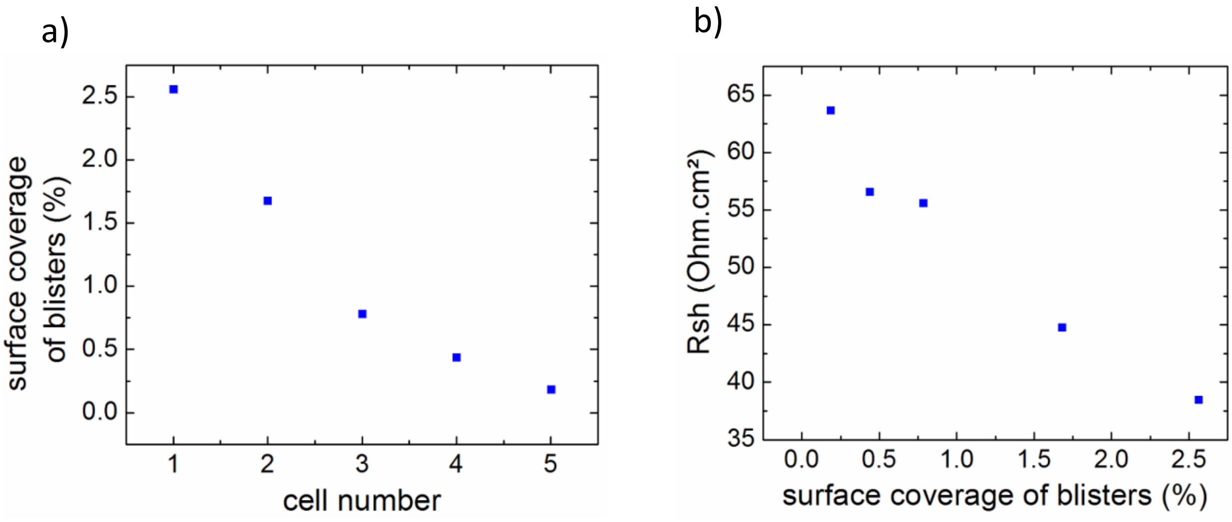

Figure 5.18: (a) Evolution of coverage of the surface by blisters on solar cells 1, 2, 3, 4 and 5 of figure 5.17b, (b) evolution of the shunt resistance of the solar cells with the blister surface coverage.

In the present study, samples A, B, C and D have a ZnSe molar ratio of about 0.21. From the graph 5.10 (evolution of J_{sc} with ZnSe ratio, in the section 5.2), the short circuit current expected is 34 mA.cm^{-2}. The solar cells which are the further from the center of the sample lie in the range of around +10% of zinc, which corresponds to a ZnSe ratio of 0.3. For these cells, the expected short circuit current is around 30 mA/cm^2.

To compare these data with J_{sc} values of the solar cells, a number is attributed to each of the solar cells of a sample, which increases with increasing distance between the solar cell and the center of the sample, as shown in figure 5.19a. From this cell numbering, averages of the cells with the same number are calculated. For these calculations of average values of J_{sc}, two very low efficiency cells were discarded from sample B (<2%). The results are shown in figure 5.19. The cell numbers are not proportional to the distance to the center, they are only meant to compare values of J_{sc} of cells at different positions.

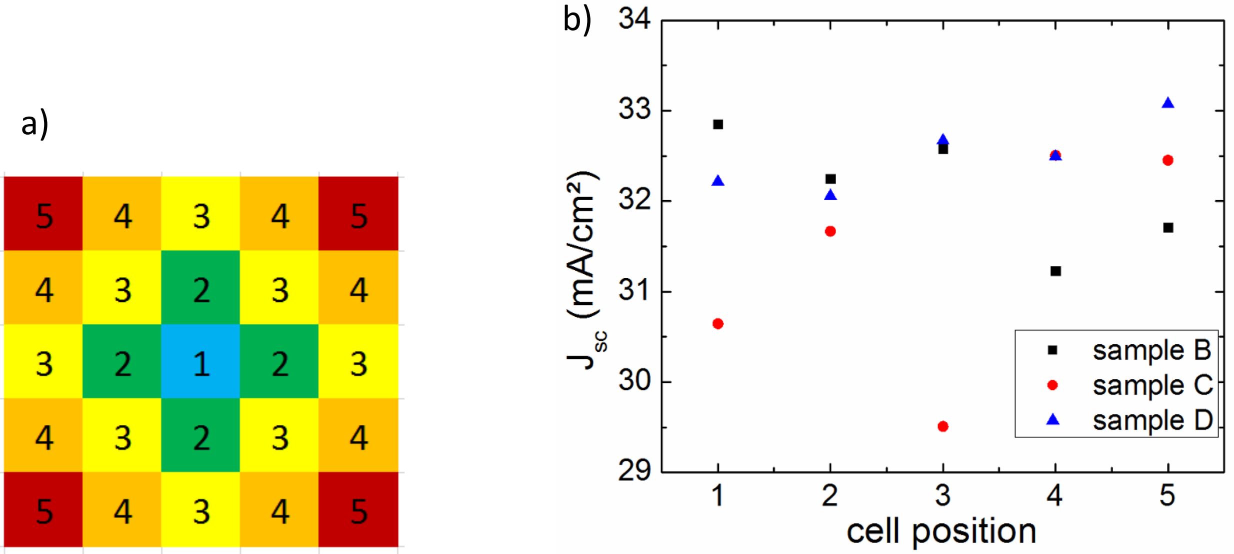

Figure 5.19: (a) Numbering of solar cells for average calculations. Numbers are given taking as reference the numbering used for pinholes counting (figure 5.17b): the same number is attributed to all cells which are equidistant to the center of the sample. (b) average short circuit current for each type of solar (see figure 5.19a for the correspondence of numbers on the samples). Only samples B, C and D are presented here, because sample A has only a measurement of a part of its surface.

As expected, figure 5.19 shows that J_{sc} values range from 30 to 33 mA.cm^{-2}. However, there is no trend of decrease of their values towards the edges of the samples (34 mA/cm^2 was expected for cell 0, and 30 mA/cm^2 was expected for cell 5). The differences of ZnSe ratio are probably too low to result in significant changes of J_{sc}.

The results of this section 5.3.2 show a good reproducibility of the process, since the four samples all reach efficiencies between 5 and 6% for their best solar cells, which tends to show that the selection of absorbers is fruitful. Furthermore, the analysis of distribution of cells efficiencies shows that best efficiencies are constantly attained at the edges of all the samples. Further examination shows that this is due to losses of shunt resistance from the edges towards the center of the samples, due to micrometer-sized blisters which become more and more abundant from edges to center. Thus, the same pinholing behavior than that presented in section 5.3.1 is detected here, but at a lesser extent since only the central part of the samples is affected.

5.3.3 Origin of formation of blisters

The blisters present in the selenized thin films are most probably originating from the electrodeposition. Blistering of Cu/Sn/Zn stacks during the deposition of the metals was described in section 3.2.2. The size of blisters observed in chapter 3 was of about 50-100 micrometers diameter (figure 3.1), and the size of the blisters observed in chapter 5 is also about the same (figures 5.11 and 5.12). Furthermore, the fact that the blistering of the samples during electrodeposition is not controllable and occurs at different extents for different samples explains the strong discrepancies of R_{sh} values for solar cells made with similar processes, and the need to select the samples before deciding to implement them into solar cell devices.

5.4 Effect of prealloying before selenization

The influence of the alloying step at 350°C between electrodeposition and selenization is investigated in this last section, with the initial motivation to try to improve the adhesion of the metallic layers and reduce problems of blistering. For this, four samples were prepared with a precursor composition of Cu/(Zn+Sn)=0.8 and Zn/Sn=1.2. Each of them was annealed for a different time (1 min, 5 min, 25 min and 125 min). The samples were then selenized with a standard process (550°C for 30 min in 10 mbar N_2/H_2).

Figure 5.20a shows that very high V_{oc} values are obtained at times of 1, 5 and 125 min. The values are higher than the best V_{oc} which were previously obtained: without prealloying process, the best V_{oc} values were 350 mV, and here values of 390 mV are obtained with 1 min prealloying. The distributions of their values are very narrow as well, which shows a very good homogeneity over the complete surface of the samples, which also differs from non-prealloyed samples. These high values of V_{oc} result in increased efficiencies: a best solar cell of 7.2% conversion efficiency is obtained at 1 min prealloying.

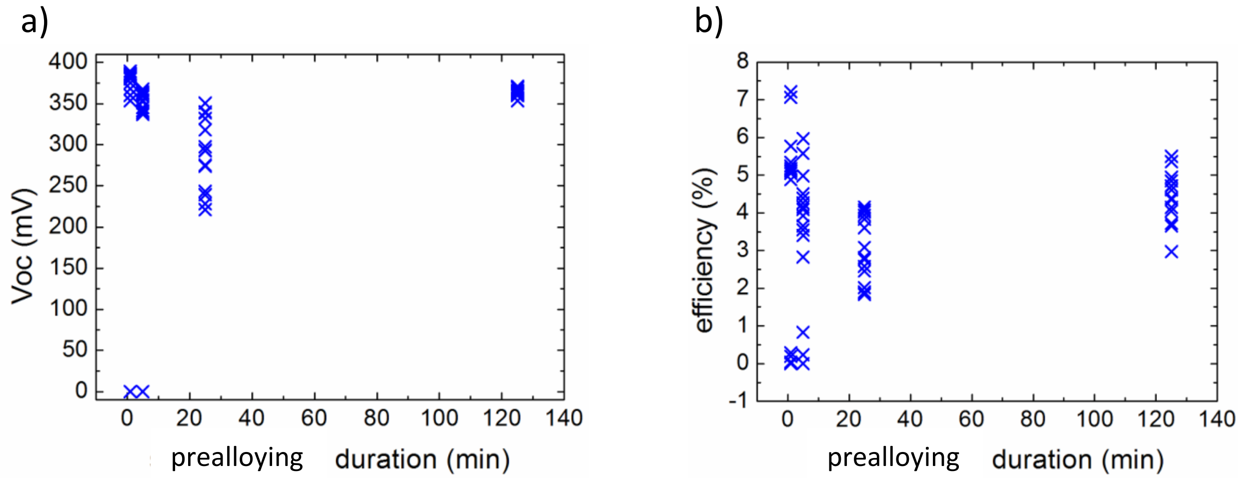

Figure 5.20: Evolution of (a) V_{oc} and (b) efficiency of solar cells from samples prealloyed for various times. 16 solar cells are built on each sample.

The alloying of 25 min gives different results: V_{oc} values are lower and more scattered, which resembles more the samples made without prealloying. Figure 5.21 shows the J-V curve of the best solar cell, obtained by using the sample alloyed for 1 min. The fact that at longer times of prealloying the V_{oc} is decreasing is in contradiction with findings of Jiang et al [96], who found an increase of all cells parameters (efficiency, J_{sc}, FF and V_{oc}) with increasing time of prealloying. In this paper, the reason which is given for the improvement observed is an increased smoothness of the film after longer prealloying, which then reduces the interface absorber/CdS, and thus decreases interface recombination. However, it is rather difficult to make a clear comparison between our study and the study of Jiang et al, because of the different types of layers obtained between Jiang s process and the process of this thesis.

Short times of prealloying (1 to 5 minutes) process clearly allow to reach very high values of V_{oc} of around 390 mV, which are homogeneous over the full surface of the samples. However, a drawback of this process is that values of FF and J_{sc} become very variable over the surface, which affects the efficiency of the solar cells.

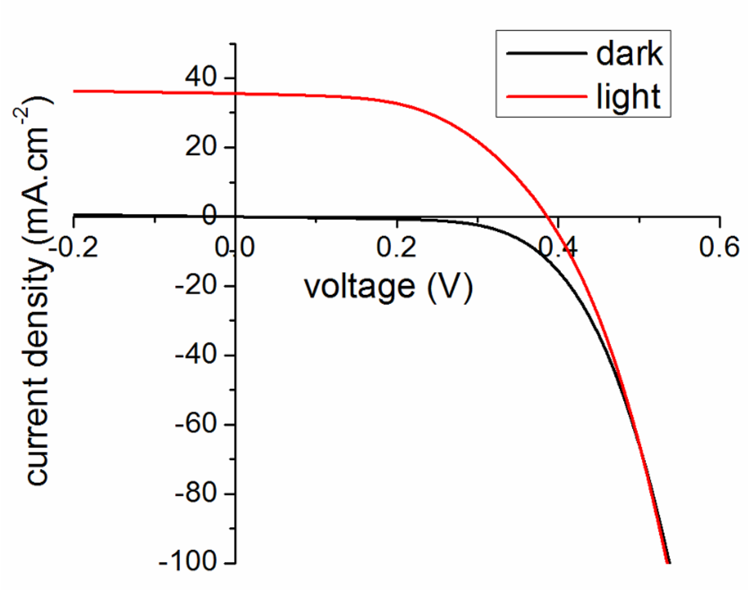

Figure 5.21: J-V characteristics of the best solar cell obtained (1 min prealloying). The power conversion efficiency is 7.2%, V_{oc}=386 mV, J_{sc}=35.5 mA/cm² and FF=53%.

5.5 Conclusion

This chapter shows that there is a strong linear relationship between the ratio of ZnSe and the short circuit current of the devices. The short circuit current of the solar cells increases with decreasing ZnSe ratio, up to a value of ZnSe/(CZTSe+ZnSe) of about 0.2, for which the J_{sc} values are typically around 35-40 mA/cm². This is due to a higher surface coverage by ZnSe, which can be detected by the optical absorption by this secondary phase, as evidenced in EQE spectra. Below a ZnSe ratio of 0.2, a strong drop of short circuit current is observed, thus 0.2 ZnSe is the optimal value for J_{sc}. Concerning other cells parameters, the V_{oc} and the fill factor are shown to strongly depend on the shunt resistance of the solar cells. Low shunt resistances seem to be the highest drawback for achieving high power conversion efficiencies.

It is shown that the probable origin of low R_{sh} is the formation of fragile blisters in the layers, which appear during the electrodeposition process (the phenomenon was described in chapter 3). These weak parts of the absorber easily result in pinholes, and can cause short shunting paths from the CdS layer directly to the Mo back contact. Furthermore, this hypothesis is strengthened by analyzing complete samples of 2x2 cm², analysed by making mini solar cells (0.1 cm²) on the total surface. This provides a mapping of cells characteristics over the area. The best efficiencies are achieved at the edges of the samples, due to different proportions of blisters in the center than in the edge of the samples. A correlation of proportion of blisters versus solar cells shunt resistance is established.

Additionally, the time of the alloying step between electrodeposition and selenization proposed by Ahmed [40] or Vauche [57] was investigated. Short prealloying times seem to be very beneficial for the open circuit of the devices, since high V_{oc} values of around 390 mV are obtained, with a solar cell of 7.2%. This value is close to the best reported efficiency for an electrodeposition-based process, which is 9.1% [41]. However, the effects of this process on FF and J_{sc} are still not understood.

Finally, the improvements of the power conversion efficiencies achieved during this thesis can be summarized as shown in figure 5.22. At the start of the project, the highest efficiency of the laboratory for a selenide Kesterite solar cell was about 1%. This efficiency was increased by changing the type of metallic precursor from Cu/Sn/Cu/Zn to Cu/Sn/Zn. Further improvement was obtained by increasing the short circuit current of the solar cells thanks to the optimization of the ZnSe ratio. Finally, the value of 7.2% was obtained by increasing the open circuit voltage of the solar cell via prealloying of the metallic precursors.

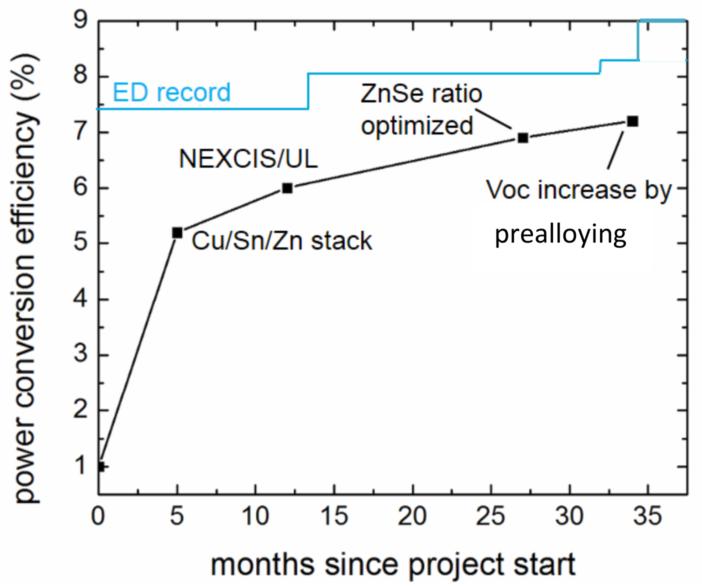

Figure 5.22: Best solar cells power conversion efficiencies achieved over the period of the project.

6 General conclusions and perspectives

6.1 Alloying and selenization of Cu/Sn/Zn stacks

This thesis brings mainly insight into the phenomenon of segregation of zinc selenide during the selenization of metallic layers of Cu-Sn-Zn. By employing a novel method of analysis at a specific position of a sample after different steps of the synthesis, a spatial correlation between the segregation of zinc selenide and the segregation of metals during alloying is established. By analyzing the thin films at scales larger than previously reported in the literature, it was shown that segregation of Cu-Zn and Cu-Sn at very large scales of 10-20 micrometers occur during the alloying. This segregation of metals then affects the selenization process: a preferential growth of ZnSe on areas which were rich of tin before the selenization is observed, attributed to the decrease of rate of formation of Kesterite on the tin-rich zones because of evaporation of tin selenide.

It was also shown that a mechanism of self-regulation of the tin content in the layers is established during the selenization. During the beginning of the selenization process, loss of tin is observed, and is due to the high vapor pressure of tin selenide at the temperature used for the conversion to selenide (550°C). The strong loss of tin at the beginning is probably due to the presence of large amounts of free tin segregated at large scales in the alloyed precursor. The large segregation of tin reduces the possibility of tin selenide to react with Cu-Se or ZnSe, thus a large quantity of SnSe evaporates during the first stages of the selenization process. At longer selenization times, a replenishment of tin in the layers is observed, due to the reaction of SnSe with Cu-Se and ZnSe, all needed Sn being provided via gas phase.

An investigation of the influence of precursors composition was done, in a domain with $Cu/Sn<2$ and $Zn/Sn>1$ (which is included in the Cu-poor $Cu/(Zn+Sn)<1$ and Zn-rich $Zn/Sn>1$ domain). The study shows that the process of tin evaporation and replenishment leads to a self-regulation of tin content to $Cu/Sn=2$. It can be explained by the fact that SnSe can only react with a copper-containing species, to form either Kesterite or Cu_2SnSe_3. Thus during the replenishment in the last part of the selenization process, only a stoichiometric amount of tin with respect to Cu_2 can be incorporated, which explains the value of $Cu/Sn=2$.

As a consequence, the thin films after selenization are mainly composed of Kesterite and ZnSe. ZnSe mainly segregates at the surface of the films, forming large scale aggregates of 10-20 micrometers diameter.

6.2 Solar cells parameters

The effect of the presence of ZnSe at the surface of the absorbers was investigated. ZnSe affects the short circuit current of the devices made with absorbers of different compositions, because of its resistivity. It acts as an insulator between the absorber and the CdS/ZnO layer. A linear relationship between the increase of ZnSe/(CZTSe+ZnSe) ratio and the decrease of J_{sc} is found for $ZnSe/(CZTSe+ZnSe)>0.2$. Below this ratio, a strong drop of short circuit current is observed, thus the optimal value is $ZnSe/(CZTSe+ZnSe)=0.2$.

The presence of blisters in the absorbers is detected. These blisters are protuberant parts of the layers, with a void underneath. They originate most probably from the electrodeposition process, during which each layer of metal is deposited to form the Cu/Sn/Zn stack. During this process, hydrogen can be formed by reduction of water, and bubbles of this gas can be trapped in the layers. Their growth creates compressive stress, which causes delamination of the layers between the copper and the molybdenum substrate. Further expansion of the hydrogen bubbles causes the formation of blisters, which then remain even after selenization. These blisters are fragile and easily create pinholes, leaving bare molybdenum apparent. This creates shortcuts in the devices, which decreases their shunt resistance, and decreases the V_{oc} and FF of the solar cells. A higher amount of blisters is generally found in the center of 2.1x2.1 cm^2 samples than in their edges, which results in higher efficiencies reached at the edges, where nearly no blisters are detected. The increased presence of blisters in the center of the samples can be due to the increasing relative speed from the center to the edge of the rotating electrode, which can more efficiently remove hydrogen bubbles forming on the surface.

Finally, further investigation of the effect of precursor microstructure was done by adding an intermediate step, in order to alloy the Cu/Sn/Zn stacks, prior to selenization. The time of alloying is investigated, and shows an increase of V_{oc} of more than 10% at 1 min prealloying. A best power conversion efficiency of 7.2% was obtained via this process, close to the 9.1% record value obtained with a similar process [41].

6.3 Recommendations for further studies

From the results of this work, several points can be considered to improve the process and its understanding.

6.3.1 Investigation of the effect of precursor microstructure on the selenization.

Two observations are considered for this paragraph: the results of section 4.4 (segregation of ZnSe) showing that the microstructure of a prealloyed sample has an effect on the mechanism of selenization and directly affects the microstructure of the selenized sample, and the observation of section 5.4 suggesting that the prealloying time has an effect on the V_{oc} of the solar cells. From these findings, it can be hypothesized that different alloying times result in different microstructures of alloyed films of Cu-Sn-Zn, which in turn change the properties of the solar cells.

To test this hypothesis, two investigations can be performed, on (i) the effect of prealloying time on microstructure, with optical microscope analysis and (ii) the selenization of different types of microstructures. Investigation (i) is relatively easy since it only requires to observe the microstructure after alloying, whereas (ii) would require to decorrelate alloying and selenization. For this, it would be ideal to perform a controlled prealloying in the selenization chamber, and directly start the selenization. This would avoid to have a first process of prealloying, and then perform the selenization in a second separate step, which is again including a prealloying during the heating ramp. To perform in one single process a controlled alloying (to obtain a controlled metallic alloy microstructure), a new oven design is required.

An ideal selenization furnace for this purpose would allow to decorrelate the heating ramp (when the sample is purely heated, without incorporation of selenium), from the selenization itself (when selenium reacts with the metals). A possible example of oven design is shown in figure 6.1. The oven proposed is composed of three zones, which allow controlling independently the temperature of the sample, of the Se powder and of the SnSe powder. Each powder is put in a quartz ampoule, which is connected to the graphite box where the reaction occurs via a quartz tube. Thus, the flow rate of selenium and tin selenide can be accurately controlled by the temperature of each of the zones. The quartz container in which the powders are is necessary to drive all the vapors of Se and SnSe generated directly inside the reaction chamber. Without these quartz elements, most of the vapors would condense on the cold parts of the oven, outside the heating zones.

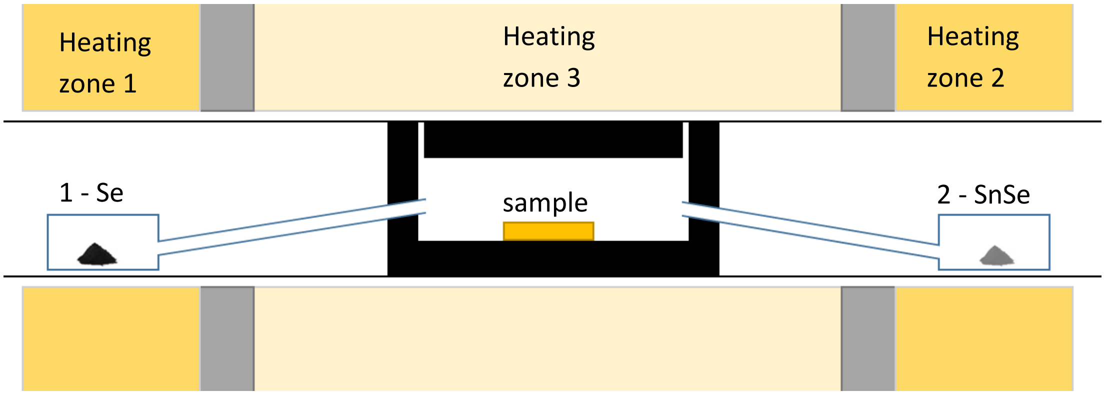

Figure 6.1: Three-zone oven with independent heating of sample, Se and SnSe.

In this way, a very large field of investigation would be opened, and probable improvement would occur. A very interesting experiment would be to investigate the effect of incorporating the chalcogen at different times of heating of the sample, to follow the work which was done by investigating different prealloying times and led to increased V_{oc} values. Probably different sizes of Cu-Zn and Cu-Sn can then be achieved, and different sizes of ZnSe aggregates will result.

6.3.2 Decrease of blistering effect

Another objective would be to try to decorrelate several parameters which decrease the efficiencies and make the analysis of the process difficult. The blistering effect would be the first problem to address, and could make the understanding of the synthesis much easier by getting rid of a source of non-reliability of the process, and by improving the homogeneity of the solar cells parameters over the samples surface. For this, changes in the electrodeposition process need to be investigated, in order to avoid formation of hydrogen between copper and Mo during copper deposition. Electrodeposition potentials have already been optimized during the thesis, thus other changes need to be done, such as changes of the chemistry of the electrolytes. Also alternative back contacts could be tested, on which hydrogen deposition overpotential could be increased, thus decreasing the problem of hydrogen formation. It has already been shown that it is possible to synthesize device-quality CZTSSe thin films on materials such as Au, W, or Pt

[97]. Even Mo substrates grown using different sputtering modes (RF and DC) are reported to have an influence on the growth of metallic thin films, as reported by Jubault [98], and could be tested.

Appendix A: XRD analyses of samples selenized at 400°C.

Detection of Cu_5Zn_8:

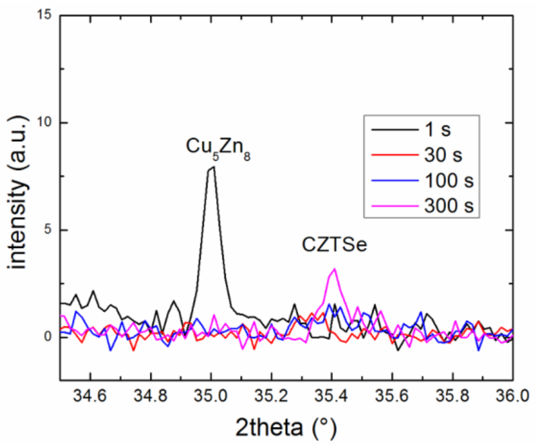

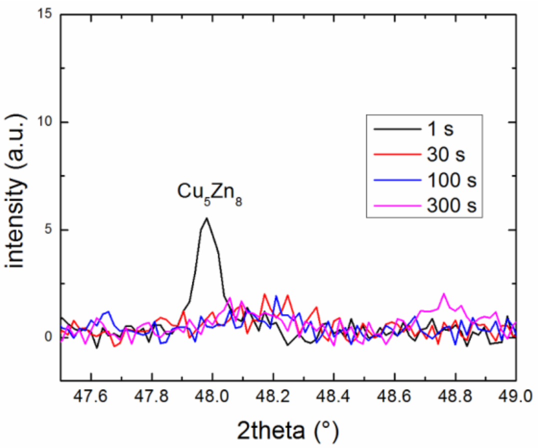

Detection of Kesterite:

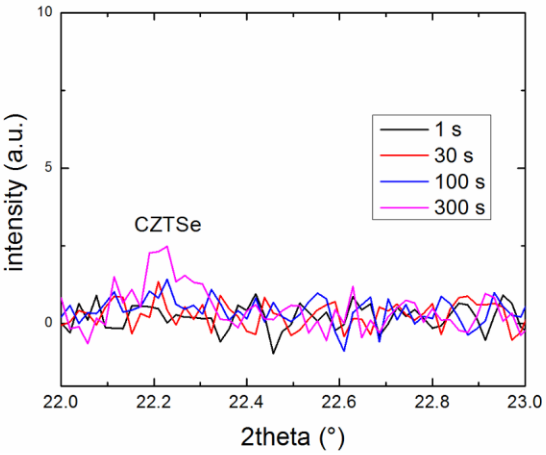

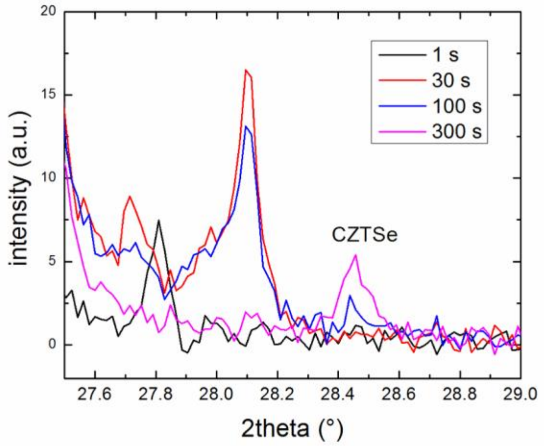

Detection of $ZnSe/Cu_2SnSe_3/Cu_2ZnSnSe_4$:

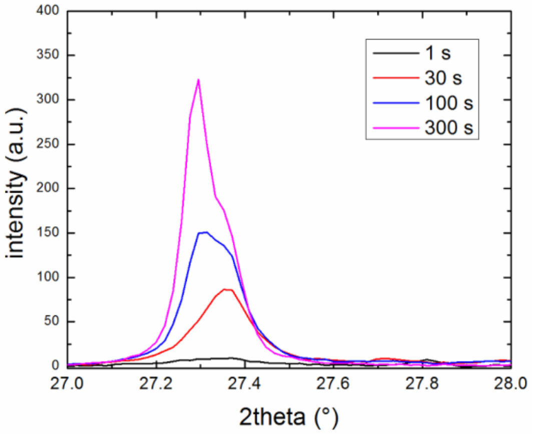

Detection of Cu_xSe:

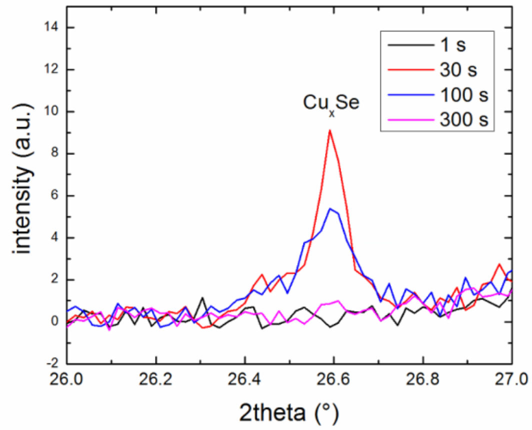

Appendix B: Images of surface of absorbers reaching highest efficiencies (over 5.5%). Each image corresponds to a different sample.

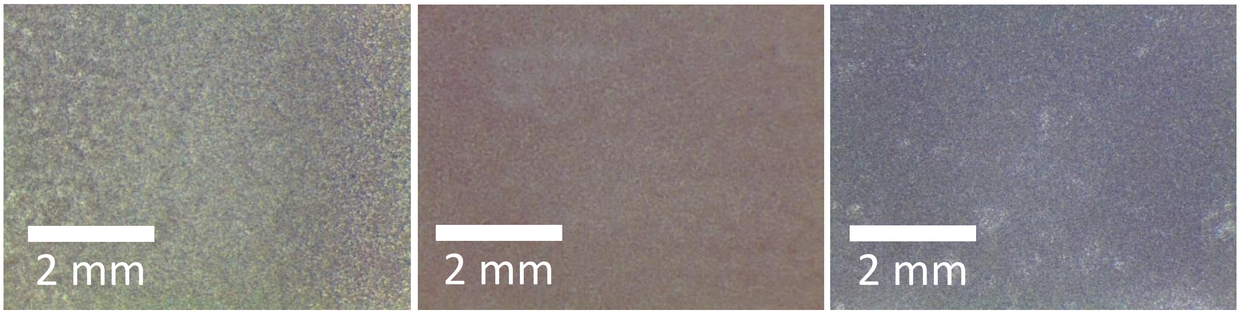

Figure: samples on which the best solar cell has an efficiency of (a) 7.2%, (b) 6.9%, (c) 6%.

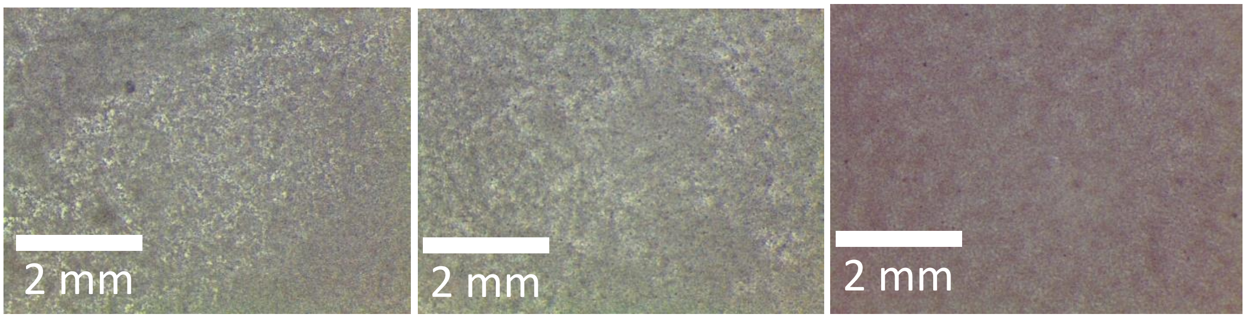

Figure: samples on which the best solar cell has an efficiency of (a) 6%, (b) 5.8%, (c) 5.7%.

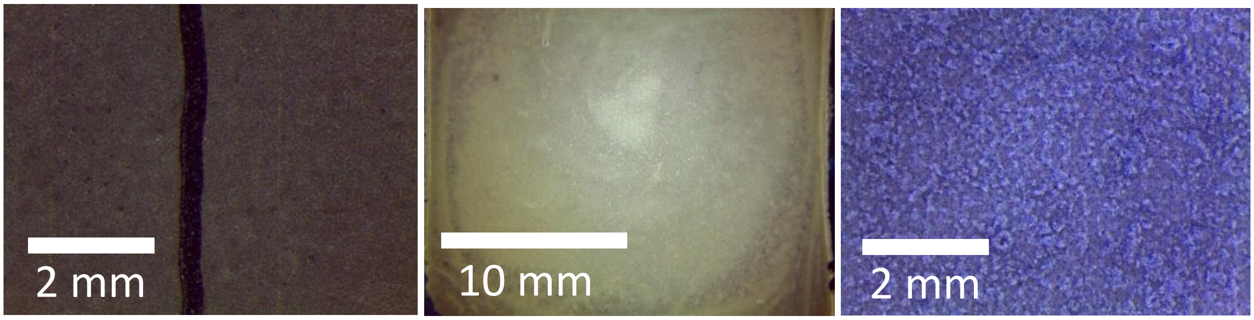

Figure: samples on which the best solar cell has an efficiency of (a) 5.7%, (b) 5.7%, (c) 5.6%.

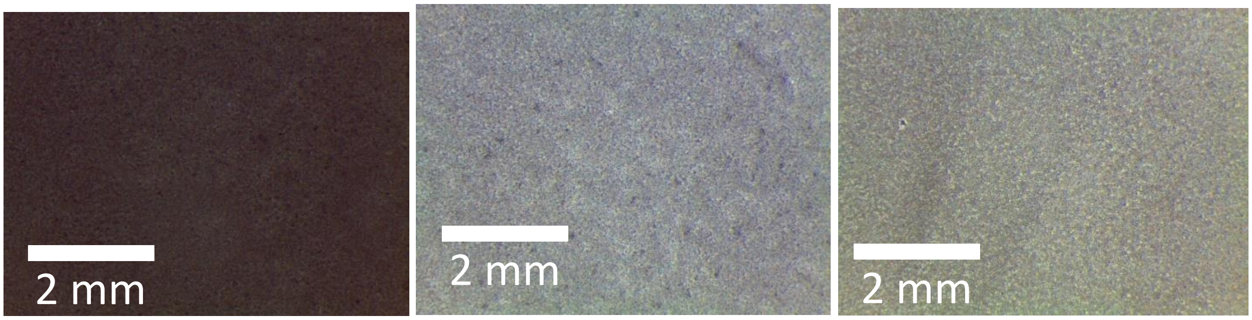

Figure: samples on which the best solar cell has an efficiency of (a) 5.6%, (b) 5.5%, (c) 5.5%.

Appendix C: Study of blistering effect within a sample

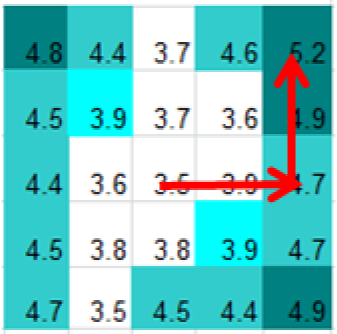

4.8	4.4	3.7	4.6	5.2
4.5	3.9	3.7	3.6	4.9
4.4	3.6	3.5	3.9	4.7
4.5	3.8	3.8	3.9	4.7
4.7	3.5	4.5	4.4	4.9

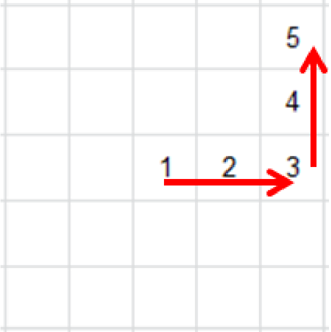

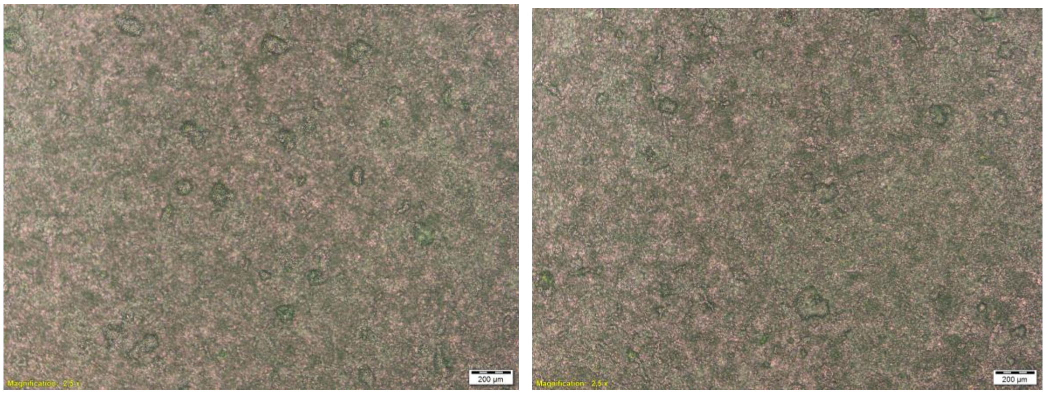

Figure: (a) and (b) optical microscope images of two positions randomly chosen on cell 1. Measurement of ratio of area covered with blisters gives 0.025 in figure (a) and 0.026 in figure (b).

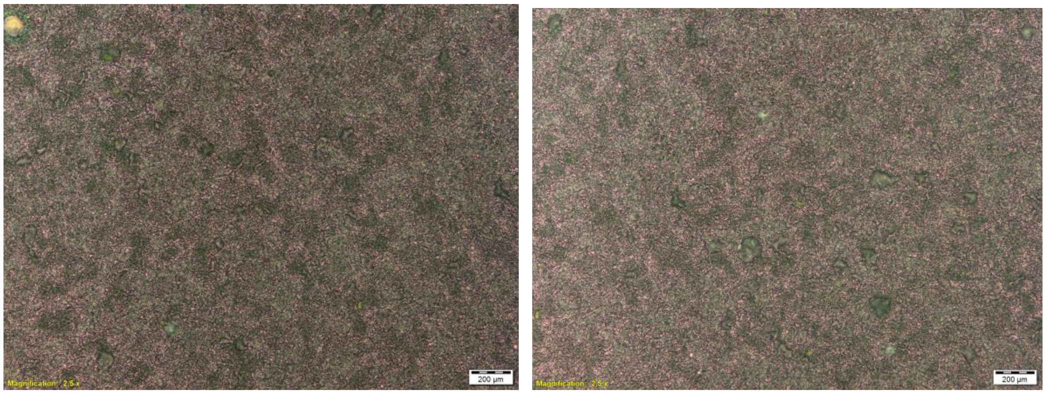

Figure: cell 2 – 0.018 and 0.015

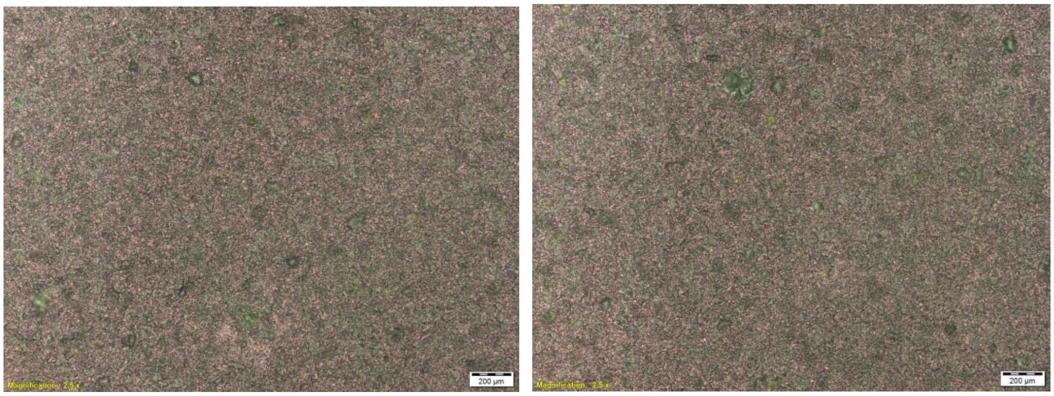

Figure: cell 3 – 0.0074 and 0.0082

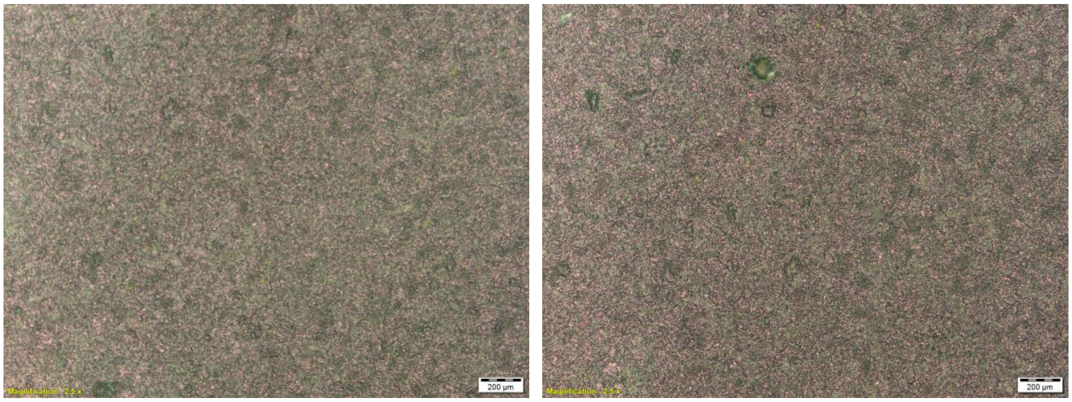

Figure: cell 4 – 0.0036 and 0.0052

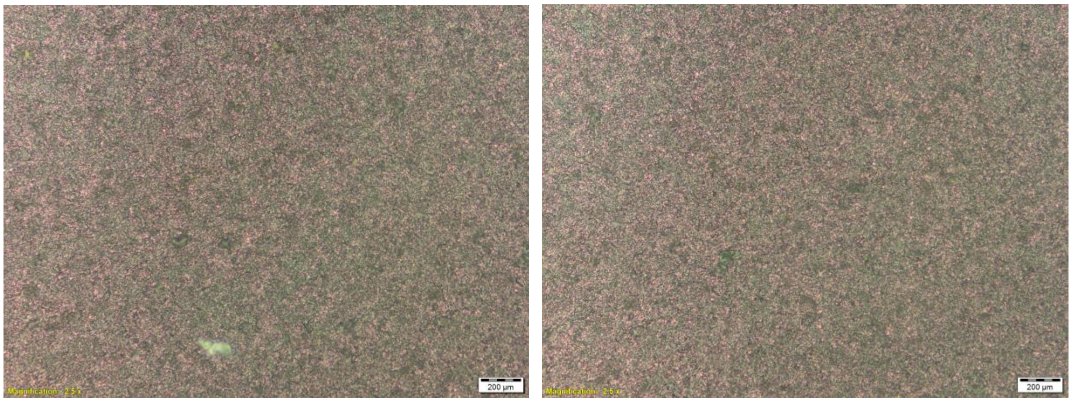

Figure: cell 5 – 0.00215 and 0.00157

Literature

[1] U. Nations, “World Population Prospects: The 2015 Revision,” 2015.

[2] British Petroleum, “BP Statistical Review of World Energy, June 2015,” *Nucl. Energy*, no. June, p. www.bp.com/statisticalreview, 2015.

[3] M. A. Green, K. Emery, Y. Hishikawa, W. Warta, and E. D. Dunlop, “Solar cell efficiency tables (version 46),” *Prog. Photovoltaics Res. Appl.*, vol. 23, no. 7, pp. 805–812, Jul. 2015.

[4] C. S. Tao, J. Jiang, and M. Tao, “Natural resource limitations to terawatt-scale solar cells,” *Sol. Energy Mater. Sol. Cells*, vol. 95, no. 12, pp. 3176–3180, 2011.

[5] A. J. Nozik, G. Conibeer, and M. C. Beard, *Advanced Concepts in Photovoltaics*. The Royal Society of Chemistry, 2014.

[6] “NREL efficiency chart.” [Online]. Available: http://www.nrel.gov/ncpv/images/efficiency_chart.jpg.

[7] P. Jackson, D. Hariskos, R. Wuerz, O. Kiowski, A. Bauer, T. M. Friedlmeier, and M. Powalla, “Properties of Cu(In,Ga)Se 2 solar cells with new record efficiencies up to 21.7%,” *Phys. status solidi - Rapid Res. Lett.*, vol. 9999, no. 9999, p. n/a–n/a, Dec. 2014.

[8] USGS, “Commodity statistics and information, USGS Minerals Information,” 2016. .

[9] K. I. and T. Nakazawa, “Electrical and Optical Properties of Stannite-Type Quaternary Semiconductor Thin Films,” *Jpn. J. Appl. Phys.*, vol. 27, no. 11R, p. 2094, 1988.

[10] S. Chen, X. G. Gong, A. Walsh, and S.-H. Wei, “Crystal and electronic band structure of Cu2ZnSnX4 (X=S and Se) photovoltaic absorbers: First-principles insights,” *Appl. Phys. Lett.*, vol. 94, no. 4, 2009.

[11] W. Shockley and H. J. Queisser, “Detailed Balance Limit of Efficiency of p-n Junction Solar Cells,” *J. Appl. Phys.*, vol. 32, no. 3, 1961.

[12] B. . Pamplin, “A systematic method of deriving new semiconducting compounds by structural analogy,” *J. Phys. Chem. Solids*, vol. 25, no. 7, pp. 675–684, Jul. 1964.

[13] R. Nitsche, D. F. Sargent, and P. Wild, “Crystal growth of quaternary 122464 chalcogenides by iodine vapor transport,” *J. Cryst. Growth*, vol. 1, no. 1, pp. 52–53, Jan.

1967.

[14] H. Katagiri, N. Sasaguchi, S. Hando, S. Hoshino, J. Ohashi, and T. Yokota, “Preparation and evaluation of Cu2ZnSnS4 thin films by sulfurization of E⍰B evaporated precursors,” *Sol. Energy Mater. Sol. Cells*, vol. 49, no. 1–4, pp. 407–414, Dec. 1997.

[15] W. Wang, M. T. Winkler, O. Gunawan, T. Gokmen, T. K. Todorov, Y. Zhu, and D. B. Mitzi, “Device Characteristics of CZTSSe Thin-Film Solar Cells with 12.6% Efficiency,” *Adv. Energy Mater.*, vol. 4, p. 1301465, 2013.

[16] S. Abermann, “Non-vacuum processed next generation thin film photovoltaics: Towards marketable efficiency and production of CZTS based solar cells,” *Sol. Energy*, vol. 94, no. 0, pp. 37–70, 2013.

[17] H. Azimi, Y. Hou, and C. J. Brabec, “Towards low-cost{,} environmentally friendly printed chalcopyrite and kesterite solar cells,” *Energy Environ. Sci.*, vol. 7, no. 6, pp. 1829–1849, 2014.

[18] D. Colombara, A. Crossay, L. Vauche, S. Jaime, M. Arasimowicz, P.-P. Grand, and P. J. Dale, “Electrodeposition of kesterite thin films for photovoltaic applications: Quo vadis?,” *Phys. status solidi*, vol. 212, no. 1, pp. 88–102, 2015.

[19] S. Delbos, “Kësterite thin films for photovoltaics : a review,” *EPJ Photovoltaics*, vol. 3, p. 35004, Aug. 2012.

[20] C. M. Fella, Y. E. Romanyuk, and A. N. Tiwari, “Technological status of Cu2ZnSn(S,Se)4 thin film solar cells,” *Sol. Energy Mater. Sol. Cells*, vol. 119, pp. 276–277, Dec. 2013.

[21] T. J. Huang, X. Yin, G. Qi, and H. Gong, “CZTS-based materials and interfaces and their effects on the performance of thin film solar cells,” *Phys. status solidi – Rapid Res. Lett.*, vol. 08, no. 09, pp. 735–762, 2014.

[22] H. Katagiri, K. Jimbo, W. S. Maw, K. Oishi, M. Yamazaki, H. Araki, and A. Takeuchi, “Development of CZTS-based thin film solar cells,” *Thin Solid Films*, vol. 517, no. 7, pp. 2455–2460, Feb. 2009.

[23] X. Liu, Y. Feng, H. Cui, F. Liu, X. Hao, G. Conibeer, D. B. Mitzi, and M. Green, “The current status and future prospects of kesterite solar cells: a brief review,” *Prog. Photovoltaics Res. Appl.*, p. n/a–n/a, Jan. 2016.

[24] D. B. Mitzi, O. Gunawan, T. K. Todorov, K. Wang, and S. Guha, “The path towards a high-

performance solution-processed kesterite solar cell," *Sol. Energy Mater. Sol. Cells*, vol. 95, no. 6, pp. 1421–1436, Jun. 2011.

[25] D. B. Mitzi, O. Gunawan, T. K. Todorov, and D. A. Barkhouse, "Prospects and performance limitations for Cu-Zn-Sn-S-Se photovoltaic technology," *Philos Trans A Math Phys Eng Sci*, vol. 371, no. 1996, p. 20110432, 2013.

[26] L. M. Peter, "Electrochemical routes to earth-abundant photovoltaics: A minireview," *Electrochem. commun.*, vol. 50, pp. 88–92, Jan. 2015.

[27] A. Polizzotti, I. L. Repins, R. Noufi, S. H. Wei, and D. B. Mitzi, "The state and future prospects of kesterite photovoltaics," *Energy Environ. Sci.*, vol. 6, no. 11, pp. 3171–3182, 2013.

[28] K. Ramasamy, M. A. Malik, and P. O'Brien, "Routes to copper zinc tin sulfide Cu2ZnSnS4 a potential material for solar cells," *Chem. Commun.*, vol. 48, no. 46, pp. 5703–5714, 2012.

[29] I. Repins, N. Vora, C. Beall, S.-H. Wei, Y. Yan, M. Romero, G. Teeter, H. Du, B. To, M. Young, and R. Noufi, "Kesterites and Chalcopyrites: A Comparison of Close Cousins," *MRS Proc.*, vol. 1324, pp. mrss11–1324–d17–01, Jun. 2011.

[30] I. L. Repins, M. J. Romero, J. V. Li, S.-H. Wei, D. Kuciauskas, C.-S. Jiang, C. Beall, C. DeHart, J. Mann, W.-C. Hsu, G. Teeter, A. Goodrich, and R. Noufi, "Kesterite Successes, Ongoing Work, and Challenges: A Perspective From Vacuum Deposition," *IEEE J. Photovoltaics*, vol. 3, no. 1, pp. 439–445, Jan. 2013.

[31] S. Siebentritt and S. Schorr, "Kesterites - a challenging material for solar cells," *Prog. Photovoltaics*, vol. 20, no. 5, pp. 512–519, 2012.

[32] S. A. Vanalakar, G. L. Agawane, S. W. Shin, M. P. Suryawanshi, K. V. Gurav, K. S. Jeon, P. S. Patil, C. W. Jeong, J. Y. Kim, and J. H. Kim, "A review on pulsed laser deposited CZTS thin films for solar cell applications," *J. Alloys Compd.*, vol. 619, pp. 109–121, Jan. 2015.

[33] Kentaro Ito, "Copper Zinc Tin Sulfide-Based Thin Film Solar Cells," 2015.

[34] S. Chen, A. Walsh, X. G. Gong, and S. H. Wei, "Classification of lattice defects in the kesterite Cu2ZnSnS 4 and Cu2ZnSnSe4 earth-abundant solar cell absorbers," *Adv. Mater.*, vol. 25, no. 11, pp. 1522–1539, 2013.

[35] G. Rey, A. Redinger, J. Sendler, T. P. Weiss, M. Thevenin, M. Guennou, B. El Adib, and S. Siebentritt, "The band gap of Cu2ZnSnSe4: Effect of order-disorder," *Appl. Phys. Lett.*,

vol. 105, no. 11, 2014.

[36] I. V Dudchak and L. V Piskach, “Phase equilibria in the Cu2SnSe3–SnSe2–ZnSe system,” *J. Alloys Compd.*, vol. 351, no. 1–2, pp. 145–150, 2003.

[37] S. Siebentritt, “Why are kesterite solar cells not 20% efficient?,” *Thin Solid Films*, vol. 535, no. 1, pp. 1–4, May 2013.

[38] A. Redinger, D. M. Berg, P. J. Dale, and S. Siebentritt, “The Consequences of Kesterite Equilibria for Efficient Solar Cells,” *J. Am. Chem. Soc.*, vol. 133, no. 10, pp. 3320–3323, 2011.

[39] J. J. Scragg, P. J. Dale, D. Colombara, and L. M. Peter, “Thermodynamic Aspects of the Synthesis of Thin-Film Materials for Solar Cells,” *ChemPhysChem*, vol. 13, no. 12, pp. 3035–3046, 2012.

[40] S. Ahmed, K. B. Reuter, O. Gunawan, L. Guo, L. T. Romankiw, and H. Deligianni, “A High Efficiency Electrodeposited Cu2ZnSnS4 Solar Cell,” *Adv. Energy Mater.*, vol. 2, no. 2, pp. 253–259, 2011.

[41] L. Vauche, “Process development and scale-up for low-cost high-efficiency kesterite thin film photovoltaics,” 2015.

[42] M. Arasimowicz, “PhD thesis,” 2015.

[43] M. C. Johnson, C. Wrasman, X. Zhang, M. Manno, C. Leighton, and E. S. Aydil, “Self-Regulation of Cu/Sn Ratio in the Synthesis of Cu2ZnSnS4 Films,” *Chem. Mater.*, vol. 27, no. 7, pp. 2507–2514, Apr. 2015.

[44] M. Arasimowicz, M. Thevenin, and P. J. Dale, “The Effect of Soft Pre-Annealing of Differently Stacked Cu-Sn-Zn Precursors on the Quality of Cu2ZnSnSe4 Absorbers,” in *Materials Research Society Spring Meeting*, 2013, vol. 1538, pp. 123–129.

[45] J. Timo Wätjen, J. Engman, M. Edoff, and C. Platzer-Björkman, “Direct evidence of current blocking by ZnSe in Cu2ZnSnSe4 solar cells,” *Appl. Phys. Lett.*, vol. 100, no. 17, p. 173510, 2012.

[46] D. M. Berg, “Kesterite equilibrium reaction and the discrimination of secondary phases from Cu2ZnSnS4,” 2012.

[47] J. J. Scragg, D. M. Berg, and P. J. Dale, “A 3.2% efficient Kesterite device from

electrodeposited stacked elemental layers," *J. Electroanal. Chem.*, vol. 646, no. 1–2, pp. 52–59, 2010.

[48] K. J. J. Mayrhofer, J. C. Meier, S. J. Ashton, G. K. H. Wiberg, F. Kraus, M. Hanzlik, and M. Arenz, "Fuel cell catalyst degradation on the nanoscale," *Electrochem. commun.*, vol. 10, no. 8, pp. 1144–1147, Aug. 2008.

[49] U. R. D. A.-R. T. Kirchartz, *Advanced characterization techniques for thin film solar cells*. 2011.

[50] S. S. Hegedus and W. N. Shafarman, "Thin-Film Solar Cells: Device Measurements and Analysis," *Prog. Photovoltaics Res. Appl.*, vol. 12, no. 2–3, pp. 155–176, 2004.

[51] a. R. Burgers, J. a. Eikelboom, a. Schonecker, and W. C. Sinke, "Improved treatment of the strongly varying slope in fitting solar\ncell I-V curves," *Conf. Rec. Twenty Fifth IEEE Photovolt. Spec. Conf. - 1996*, pp. 4–7, 1996.

[52] H. Lechtman, "Pre-Columbian surface metallurgy," *Sci. Am.*, vol. 250, no. 6, pp. 56–63154, 1984.

[53] J. J. Scragg, P. J. Dale, L. M. Peter, G. Zoppi, and I. Forbes, "New routes to sustainable photovoltaics: evaluation of Cu2ZnSnS4 as an alternative absorber material," *Phys. Status Solidi*, vol. 245, no. 9, pp. 1772–1778, 2008.

[54] H. Araki, Y. Kubo, A. Mikaduki, K. Jimbo, W. S. Maw, H. Katagiri, M. Yamazaki, K. Oishi, and A. Takeuchi, "Preparation of Cu2ZnSnS4 thin films by sulfurizing electroplated precursors," *Sol. Energy Mater. Sol. Cells*, vol. 93, no. 6–7, pp. 996–999, 2009.

[55] H. Araki, Y. Kubo, K. Jimbo, W. S. Maw, H. Katagiri, M. Yamazaki, K. Oishi, and A. Takeuchi, "Preparation of Cu2ZnSnS4 thin films by sulfurization of co-electroplated Cu-Zn-Sn precursors," *Phys. status solidi*, vol. 6, no. 5, pp. 1266–1268, 2009.

[56] L. Guo, Y. Zhu, O. Gunawan, T. Gokmen, V. R. Deline, S. Ahmed, L. T. Romankiw, and H. Deligianni, "Electrodeposited Cu2ZnSnSe4 Thin Film Solar Cell with 7% Power Conversion Efficiency," *Prog. Photovoltaics Res. Appl.*, vol. 22, no. 1, pp. 58–68, 2014.

[57] L. Vauche, L. Risch, Y. Sánchez, M. Dimitrievska, M. Pasquinelli, T. Goislard de Monsabert, P.-P. Grand, S. Jaime-Ferrer, and E. Saucedo, "8.2% pure selenide kesterite thin-film solar cells from large-area electrodeposited precursors," *Prog. Photovoltaics Res. Appl.*, vol. 24, no. 1, pp. 38–51, Jul. 2015.

[58] D. A. Skoog, D. M. West, F. J. Holler, and S. R. Crouch, *Fundamentals of Analytical Chemistry*, Eighth. Thomson Brooks/Cole, 2004.

[59] J.-O. Jeon, K. D. Lee, L. Seul Oh, S.-W. Seo, D.-K. Lee, H. Kim, J. Jeong, M. J. Ko, B. Kim, H. J. Son, J. Y. Kim, L. Seul Oh, S.-W. Seo, D.-K. Lee, H. Kim, J. Jeong, M. J. Ko, B. Kim, H. J. Son, and J. Y. Kim, "Highly efficient copper-zinc-tin-selenide (CZTSe) solar cells by electrodeposition.," *ChemSusChem*, vol. 7, no. 4, pp. 1073–7, Apr. 2014.

[60] J.-O. Jeon, K. D. Lee, L. Seul Oh, S.-W. Seo, D.-K. Lee, H. Kim, J. Jeong, M. J. Ko, B. Kim, H. J. Son, and J. Y. Kim, "Highly Efficient Copper–Zinc–Tin–Selenide (CZTSe) Solar Cells by Electrodeposition," *ChemSusChem*, vol. 7, no. 4, pp. 1073–1077, 2014.

[61] Y. Lin, S. Ikeda, W. Septina, Y. Kawasaki, T. Harada, and M. Matsumura, "Mechanistic aspects of preheating effects of electrodeposited metallic precursors on structural and photovoltaic properties of Cu2ZnSnS4 thin films," *Sol. Energy Mater. Sol. Cells*, vol. 120, Part , no. 0, pp. 218–225, 2014.

[62] C. Chou and S. Chen, "Phase equilibria of the Sn-Zn-Cu ternary system," *Acta Mater.*, vol. 54, no. 9, pp. 2393–2400, May 2006.

[63] Y. Huang, S. Chen, C. Chou, and W. Gierlotka, "Liquidus projection and thermodynamic modeling of Sn–Zn–Cu ternary system," *J. Alloys Compd.*, vol. 477, no. 1–2, pp. 283–290, May 2009.

[64] P. Aloke, *Thermodynamics, Diffusion and the Kirkendall Effect in Solids*. 2014.

[65] J. J. Scragg, P. J. Dale, and L. M. Peter, "Synthesis and characterization of Cu2ZnSnS4 absorber layers by an electrodeposition-annealing route," *Thin Solid Films*, vol. 517, no. 7, pp. 2481–2484, 2009.

[66] R. Djemour, M. Mousel, A. Redinger, L. Gütay, A. Crossay, D. Colombara, P. Dale, and S. Siebentritt, "Detecting ZnSe secondary phase in Cu2ZnSnSe4 by room temperature photoluminescence," *Appl. Phys. Lett.*, vol. 102, p. 222108, 2013.

[67] D. D. S. J. W. Dini, "Electrodeposition of Copper," in *Modern Electroplating*, Fifth Edit., M. S. and M. Paunovic, Ed. John Wiley & Sons, 2010, p. 33.

[68] T. B. Massalski, *Binary Alloy Phase Diagrams*, 2nd ed. Ohio: ASM International, 1990.

[69] W. Pfeiler, Ed., *Alloy Physics: A Comprehensive Reference*. Wiley-VCH.

[70] F. W. Ostwald, *Lehrbuch der Allgemeinen Chemie*, vol. 2. Leipzig: Engelmann, 1896.

[71] L. Choubrac, A. Lafond, M. Paris, C. Guillot-Deudon, and S. Jobic, “The stability domain of the selenide kesterite photovoltaic materials and NMR investigation of the Cu/Zn disorder in Cu2ZnSnSe4 (CZTSe).,” *Phys. Chem. Chem. Phys.*, vol. 17, no. 23, pp. 15088–92, Jun. 2015.

[72] W.-C. Hsu, B. Bob, W. Yang, C.-H. Chung, and Y. Yang, “Reaction pathways for the formation of Cu2ZnSn(Se{,}S)4 absorber materials from liquid-phase hydrazine-based precursor inks,” *Energy Environ. Sci.*, vol. 5, no. 9, pp. 8564–8571, 2012.

[73] F. Hergert and R. Hock, “Predicted formation reactions for the solid-state syntheses of the semiconductor materials Cu2SnX3 and Cu2ZnSnX4 (X = S, Se) starting from binary chalcogenides,” *Thin Solid Films*, vol. 515, no. 15, pp. 5953–5956, May 2007.

[74] C. M. Fella, A. R. Uhl, C. Hammond, I. Hermans, Y. E. Romanyuk, and A. N. Tiwari, “Formation mechanism of Cu2ZnSnSe4 absorber layers during selenization of solution deposited metal precursors,” *J. Alloys Compd.*, vol. 567, pp. 102–106, Aug. 2013.

[75] R. Adhi Wibowo, W. Hwa Jung, and K. H. Kim, “Synthesis of Cu2ZnSnSe4 compound powders by solid state reaction using elemental powders,” *J. Phys. Chem. Solids*, vol. 71, no. 12, pp. 1702–1706, Dec. 2010.

[76] J. Li, T. Ma, M. Wei, W. Liu, G. Jiang, and C. Zhu, “The Cu2ZnSnSe4 thin films solar cells synthesized by electrodeposition route,” *Appl. Surf. Sci.*, vol. 258, no. 17, pp. 6261–6265, 2012.

[77] O. Volobujeva, J. Raudoja, E. Mellikov, M. Grossberg, S. Bereznev, and R. Traksmaa, “Cu2ZnSnSe4 films by selenization of Sn-Zn-Cu sequential films,” *J. Phys. Chem. Solids*, vol. 70, no. 3–4, pp. 567–570, 2009.

[78] P. M. P. Salomé, P. A. Fernandes, and A. F. da Cunha, “Morphological and structural characterization of Cu2ZnSnSe4 thin films grown by selenization of elemental precursor layers,” *Thin Solid Films*, vol. 517, no. 7, pp. 2531–2534, Feb. 2009.

[79] A. Olin, B. Nolang, E. G. Osadchii, L.-O. Ohman, and E. Rosen, “Chemical Thermodynamics of Selenium,” *October*, p. 894, 2005.

[80] M. Altosaar, J. Raudoja, K. Timmo, M. Danilson, M. Grossberg, J. Krustok, and E. Mellikov, “Cu2Zn1–xCdx Sn(Se1–ySy)4 solid solutions as absorber materials for solar cells,” *Phys. status solidi*, vol. 205, no. 1, pp. 167–170, 2008.

[81] M. Grossberg, J. Krustok, K. Timmo, and M. Altosaar, “Radiative recombination in Cu2ZnSnSe4 monograins studied by photoluminescence spectroscopy,” *Thin Solid Films*, vol. 517, no. 7, pp. 2489–2492, 2009.

[82] A. Fairbrother, X. Fontané, V. Izquierdo-Roca, M. Espíndola-Rodríguez, S. López-Marino, M. Placidi, L. Calvo-Barrio, A. Pérez-Rodríguez, and E. Saucedo, “On the formation mechanisms of Zn-rich Cu2ZnSnS4 films prepared by sulfurization of metallic stacks,” *Sol. Energy Mater. Sol. Cells*, vol. 112, pp. 97–105, May 2013.

[83] P. J. Dale, M. Arasimowicz, D. Colombara, A. Crossay, E. Robert, and A. A. Taylor, “Is it Possible to Grow Thin Films of Phase Pure Kesterite Semiconductor? A ZnSe case study,” *2013 MRS Spring Meeting - Symposium C – Compound Semiconductors: Thin-Film Photovoltaics*, vol. 1538. Materials Research Society, San Francisco, 2013.

[84] W. C. Chou, C. M. Lin, R. S. Ro, C. S. Ho, D. Y. Hong, C. S. Yang, D. S. Chuu, T. J. Yang, J. Xu, and E. Huang, “A Raman study of ZnSe at high pressure,” *Chinese J. Phys.*, vol. 35, no. 3, pp. 266–273, 1997.

[85] M. Ishii, K. Shibata, and H. Nozaki, “Anion Distributions and Phase Transitions in CuS1-xSex(x = 0-1) Studied by Raman Spectroscopy,” *Journal of Solid State Chemistry*, vol. 105, no. 2. pp. 504–511, 1993.

[86] D. M. Berg, A. Crossay, J. Guillot, V. Izquierdo-Roca, A. P??rez-Rodriguez, S. Ahmed, H. Deligianni, S. Siebentritt, and P. J. Dale, “Simplified formation process for Cu2ZnSnS4-based solar cells,” *Thin Solid Films*, vol. 573, pp. 148–158, 2014.

[87] A. Crossay, D. Colombara, M. Melchiorre, M. Guennou, B. Mendis, and P. J. Dale, “Understanding quaternary compound Cu2ZnSnSe4 synthesis by microscopic scale analyses at an identical location,” *J. Mater. Chem. C*, no. 4, pp. 4626–4629, 2016.

[88] R. Djemour, M. Mousel, A. Redinger, L. Gütay, A. Crossay, D. Colombara, P. J. Dale, and S. Siebentritt, “Detecting ZnSe secondary phase in Cu2ZnSnSe4 by room temperature photoluminescence,” *Appl. Phys. Lett.*, vol. 102, no. 22, 2013.

[89] Y. S. Lee, T. Gershon, O. Gunawan, T. K. Todorov, T. Gokmen, Y. Virgus, and S. Guha, “Cu 2 ZnSnSe 4 Thin-Film Solar Cells by Thermal Co-evaporation with 11.6% Efficiency and Improved Minority Carrier Diffusion Length,” *Adv. Energy Mater.*, vol. 5, no. 7, p. n/a–n/a, Apr. 2015.

[90] G. Brammertz, M. Buffière, S. Oueslati, H. ElAnzeery, K. Ben Messaoud, S. Sahayaraj, C. Köble, M. Meuris, and J. Poortmans, “Characterization of defects in 9.7% efficient Cu2ZnSnSe4-CdS-ZnO solar cells,” *Appl. Phys. Lett.*, vol. 103, no. 16, p. 163904, 2013.

[91] B. Shin, Y. Zhu, N. A. Bojarczuk, S. Jay Chey, and S. Guha, “Control of an interfacial MoSe2 layer in Cu2ZnSnSe4 thin film solar cells: 8.9% power conversion efficiency with a TiN diffusion barrier,” *Appl. Phys. Lett.*, vol. 101, no. 5, pp. 53903–53904, 2012.

[92] A. Fairbrother, M. Dimitrievska, Y. Sánchez, V. Izquierdo-Roca, A. Pérez-Rodríguez, and E. Saucedo, “Compositional paradigms in multinary compound systems for photovoltaic applications: a case study of kesterites,” *J. Mater. Chem. A*, vol. 3, no. 18, pp. 9451–9455, Apr. 2015.

[93] J. Kim, H. Hiroi, T. K. Todorov, O. Gunawan, M. Kuwahara, T. Gokmen, D. Nair, M. Hopstaken, B. Shin, Y. S. Lee, W. Wang, H. Sugimoto, and D. B. Mitzi, “High efficiency Cu2ZnSn(S,Se)4 solar cells by applying a double In2S3/CdS emitter.,” *Adv. Mater.*, vol. 26, no. 44, pp. 7427–31, Nov. 2014.

[94] A. Redinger, M. Mousel, M. H. Wolter, N. Valle, and S. Siebentritt, “Influence of S/Se ratio on series resistance and on dominant recombination pathway in Cu2ZnSn(SSe)4 thin film solar cells,” *Thin Solid Films*, vol. 535, no. 1, pp. 291–295, May 2013.

[95] D. Colombara, E. V. C. Robert, A. Crossay, A. Taylor, M. Guennou, M. Arasimowicz, J. C. B. Malaquias, R. Djemour, and P. J. Dale, “Quantification of surface ZnSe in Cu2ZnSnSe4-based solar cells by analysis of the spectral response,” *Sol. Energy Mater. Sol. Cells*, vol. 123, pp. 220–227, 2014.

[96] F. Jiang, S. Ikeda, T. Harada, and M. Matsumura, “Pure Sulfide Cu 2 ZnSnS 4 Thin Film Solar Cells Fabricated by Preheating an Electrodeposited Metallic Stack,” *Adv. Energy Mater.*, vol. 4, no. 7, p. n/a–n/a, May 2014.

[97] G. Altamura, L. Grenet, C. Roger, F. Roux, V. Reita, R. Fillon, H. Fournier, S. Perraud, and H. Mariette, “Alternative back contacts in kesterite Cu2ZnSn(S1-xSex)4 thin film solar cells,” *J. Renew. Sustain. Energy*, vol. 6, no. 1, p. 011401, 2014.

[98] M. Jubault, L. Ribeaucourt, E. Chassaing, G. Renou, D. Lincot, and F. Donsanti, “Optimization of molybdenum thin films for electrodeposited CIGS solar cells,” *Sol. Energy Mater. Sol. Cells*, vol. 95, no. SUPPL. 1, pp. S26–S31, May 2011.

List of publications

Publications in peer-reviewed journals:

A. Crossay, D. Colombara, M. Melchiorre, M. Guennou, B.G. Mendis, and P. J. Dale, "Understanding quaternary compound $Cu_2ZnSnSe_4$ synthesis by microscopic scale analyses at an identical location", J. Mater. Chem. C, no. 4, pp. 4626–4629, 2016.

D. Colombara, **A. Crossay**, L. Vauche, S. Jaime, M. Arasimowicz, P.-P. Grand, and P. J. Dale, "Electrodeposition of kesterite thin films for photovoltaic applications: Quo vadis?," Phys. status solidi, vol. 212, no. 1, pp. 88–102, 2015.

D. M. Berg, **A. Crossay**, J. Guillot, V. Izquierdo-Roca, A. Pérez-Rodriguez, S. Ahmed, H. Deligianni, S. Siebentritt, and P. J. Dale, "Simplified formation process for Cu2ZnSnS4-based solar cells," Thin Solid Films, vol. 573, pp. 148–158, 2014.

D. Colombara, E. V. C. Robert, **A. Crossay**, A. Taylor, M. Guennou, M. Arasimowicz, J. C. B. Malaquias, R. Djemour, and P. J. Dale, "Quantification of surface ZnSe in Cu2ZnSnSe4-based solar cells by analysis of the spectral response," Sol. Energy Mater. Sol. Cells, vol. 123, no. 0, pp. 220–227, 2014.

D. Colombara, **A. Crossay**, D. Regesch, C. Broussillou, T. G. De Monsabert, P. P. Grand, and P. J. Dale, "Prediction of photovoltaic p-n device short circuit current by photoelectrochemical analysis of p-type CIGSe films," Electrochem. commun., vol. 48, pp. 99–102, 2014.

A. Bhatia, H. Meadows, **A. Crossay**, P. J. Dale, and M. A. Scarpulla, "Continuous wave solid phase laser annealing of single-pot electrodeposited CuInSe2 thin films: Effects of Cu/In stoichiometry," J. Appl. Phys., vol. 114, no. 4, 2013.

P. J. Dale, M. Arasimowicz, D. Colombara, **A. Crossay**, E. Robert, and A. A. Taylor, "Is it Possible to Grow Thin Films of Phase Pure Kesterite Semiconductor? A ZnSe case study," 2013 MRS Spring Meeting - Symposium C – Compound Semiconductors: Thin-Film Photovoltaics, vol. 1538. Materials Research Society, San Francisco, 2013.

R. Djemour, M. Mousel, A. Redinger, L. Gütay, **A. Crossay**, D. Colombara, P. Dale, and S. Siebentritt, "Detecting ZnSe secondary phase in Cu2ZnSnSe4 by room temperature photoluminescence," Appl. Phys. Lett., vol. 102, p. 222108, 2013.